DESIGN AND ANALYSIS OF PLANAR INVERTED-F ANTENNA (PIFA) FOR 5G APPLICATIONS

A Thesis Submitted to

Delhi Technological University

for the Award of Degree of

Doctor of Philosophy

In

Electronics and Communication Engineering

By

AKHILESH VERMA

(Enrollment No.: 2K16/Ph.D/EC/17)

Under the Supervision of

Dr. N. S. RAGHAVA

Professor

Department of Electronics and Communication Engineering

Delhi Technological University (Formerly DCE)

Bawana Road, Delhi-110042, India.

October , 2021

DECLARATION

I declare that the research work reported in this thesis entitled "**Design and Analysis of Planar Inverted-F Antenna (PIFA) for 5G Applications**" for the award of the degree of *Doctor of Philosophy in Electronics and Communication Engineering* has been carried out by me under the supervision of Prof. N.S. Raghava, Department of Electronics and Communication Engineering, Delhi Technological University, Delhi, India.

The research work embodied in this thesis, except where otherwise indicated, is my original research. This thesis has not been submitted by me earlier in part or full to any other University or Institute for the award of any degree or diploma. This thesis does not contain other person's data, graphs or other information, unless specifically acknowledged.

Date:

(Akhilesh Verma)

Enrollment no.: 2K16/Ph.D/EC/17

Department of ECE

Delhi Technological University,

Delhi-110042, India

DELHI TECHNOLOGICAL UNIVERSITY

(Formerly Delhi College of Engineering)

Shahbad Daulatpur, Bawana Road, Delhi-110042, India

CERTIFICATE

This is to certify that the research work embodied in the thesis entitled **"Design and Analysis of Planar Inverted-F Antenna (PIFA) for 5G Applications"** submitted by **Mr. Akhilesh Verma** with enrollment number **(2K16/Ph.D/EC/17)** is the result of his original research carried out in the Department of Electronics and Communication Engineering, Delhi Technological University, Delhi, for the award of **Doctor of Philosophy** under the supervision of **Prof. N.S. Raghava.**

It is further certified that this work is original and has not been submitted in part or fully to any other University or Institute for the award of any degree or diploma.

This is to certify that the above statement made by the candidate is correct to the best of our knowledge.

(Prof. N.S. Raghava)

Supervisor

Head, Department of ECE

Delhi Technological University,

Delhi-110042

ACKNOWLEDGEMENT

I would also like to thank Dr. Thennarasan Sabapathy, Associate Professor, UNIMAP, Malaysia for his valuable guidance in my research work.

I gratefully acknowledge all my colleagues of the research laboratory. I would also like to appreciate the company of research scholars of other departments from whom I got help and shared joy. I shared a great time with Rehan, Dr. Rahul Bansal, Dr. Tej Singh, Dr. Ashish Kumar, Amit, Amarendra, Rahul, Peeyush, Abhishek, Bani, Jyoti.

I would like to take the opportunity to thanks especially my best friend Abhilash, to pay gratitude for his immense help and emotional support during my Ph.D journey.

Above all, I would like to express my heartiest thanks to all my family members whose blessings and affection have been remained constant source of inspiration. I have no words to express my gratitude to my Brothers, Sister-in–law and sister.

Words cannot express my deep sense of gratitude to my life partner "Dr. Anamika" for her encouragement, motivation, understanding, cooperation and positive support during every stage of this work. I might not be able to reach at this stage without her. She is always there cheering me up and stood by me through the good and bad times equally. Last, but not least, I would like to dedicate my thesis to my beloved wife and loving parents for their endless love, patience and understanding.

Date :   **(Akhilesh Verma)**
Place : Delhi, India.

DEDICATED TO MY BELOVED PARENTS

Ved Prakash Verma

&

Satyawati Verma

CONTENTS

Abstract

This thesis investigates the PIFA antenna along with some other antennas and the role of periodic structures over the antennas to fulfil the fifth-generation (5G) requirements. The 5G wireless technology is the next step towards the evolution of cellular communication systems. There are three broad categories of 5G bands – the low (600-850 MHz), the mid (3.4-3.6 GHz), and the high (millimeter wave) and all of them have their own pros and cons.

The previous wireless technology used the antennas not having high gain, wide bandwidth, and beam steering capability for directional transmission and reception of the signal. However, 5G technology requires antennas with high-speed data rate, high gain for a wide coverage of the network with beam steering capacity (efficient coverage), and should also occupy less area (compactness). To get the high gain required for 5G communications in millimeter frequencies, beam forming technology plays a major role. There are different types of large networks used for beamforming, such as Butler matrix, Rotman lens, phased array antenna because beam steering requires it. However, these methods increase the complexity, weight, and cost of the design. In order to overcome these issues, disruptive beamforming can be used. Disruptive beamforming does not require phase shifters, power dividers to steer the beams. Disruptive beamforming uses some structures like an artificial magnetic conductor (AMC), metasurfaces, superstrate, and RF absorbers through which high gain, wide bandwidth, beam steering can be achieved. Different types of antennas can be used for the purpose of beamforming/beam steering such as monopole antenna, PIFA antenna, microstrip patch antenna, etc.

In the second chapter, compact planar inverted-F antenna (PIFA) is designed. It is found that the gain and bandwidth of the antenna are low while the SAR value is high which may not be useful for 5G and other applications. To counter low gain, the gain enhancement of the PIFA antenna is explored by applying AMC and this also helps to reduce SAR.

In the third chapter, a coplanar waveguide fed monopole antenna is designed where three superstrate structures have been explored for gain enhancement. The low gain problem is investigated in a systematic manner. Hence, to achieve high gain, AMC is used with superstrate for enhancing the forward radiation from the antenna. Finally, low dielectric superstrate is fabricated with the combination of monopole and AMC.

In the fourth chapter, beam steering capability is developed in monopole antenna with the help of non-uniform metasurface superstrate and AMC as beam steering with low scan loss is going to be a necessity for 5G communications.

In the fifth chapter, Eccosorb MCS absorber is used which is used to transform the radiation pattern of a slotted PIFA and producing a radiation beam in the desired direction while also increasing the antenna's gain.

Extending the work in the fifth chapter, we designed a planar inverted-F multi-beam antenna using RF absorbers in the sixth chapter. The proposed antenna provides multiple beams from a single antenna with wide angular coverage. The designed antenna achieves a multi-beam behaviour by six slabs of absorbers placed periodically between the PIFA patch and substrate.

In the seventh chapter, circular polarized MIMO antenna for the 5G band is designed. The MIMO antenna incorporates SIW structure which is used to perform beamforming.

The eighth chapter conclude the work and future scope of the thesis.

In this way, this thesis will discuss gain enhancement, beam splitting, and beamforming techniques using AMC, superstrate, RF absorbers, and metasurface superstrate with different antennas.

List of Figures

List of Tables

All examiner observation incorporated (page 8, 17, 25, 38, 61, 62, 94)

CHAPTER 1

Introduction

The fifth-generation (5G) wireless technology is the next step towards the evolution of cellular communication systems. There are three broad categories of 5G bands – the low (600-850 MHz), the mid (3.4-3.6 GHz), and the high (millimeter wave) and all of them have their own pros and cons. Nowadays, mid-band and sub-6 GHz bands for 5G communications are getting attention. Mid-band offers a far wider coverage area than high-band millimeter wave spectrum and, unlike millimeter wave, can penetrate walls, in addition to faster speeds and more capacity than low-band. In the millimeter range, different frequency bands are available at 24 GHz, 28 GHz, 38 GHz, and 60 GHz for 5G communication. However, electromagnetic waves face a high loss in the millimeter range during propagation. Due to all these limitations, the many initial services of 5G, 3.3-3.8 GHz, and sub-6 GHz is the expected range.

The previous wireless technology used the antennas not having high gain, wide bandwidth, and beam steering capability for directional transmission and reception of the signal. However, 5G technology requires antennas with high speed for transmitting signals (high-speed data rate), high gain for a wide coverage of the network with beam steering capacity (efficient coverage), and should also occupy less area (compactness).

To get the high gain required for 5G communications in millimeter frequencies, beamforming technology plays a major role. There are different types of large networks used for beamforming, such as Butler matrix, Rotman lens, phased array antenna because beam steering requires it. These methods increase the complexity, weight, and cost of the design. In order to overcome these issues, disruptive beamforming can be used. Disruptive beamforming does not require phase shifters, power dividers to steer the beams. Disruptive beamforming uses some structures like an artificial magnetic conductor (AMC), metasurfaces, superstrate, and RF absorbers through which high gain, wide bandwidth, beam steering can be achieved. Different types of antennas can be used for the purpose of beamforming/beam steering such as monopole antenna, PIFA antenna, microstrip patch antenna, etc.

In this chapter, a brief introduction of 5G technology and the expected spectrums are described. Next, the requirements of the antennas in future wireless technology are also described. In the end, for beam steering and gain enhancement, different types of periodic structures are also explored. This introduction lays the foundation that is needed to appreciate the work performed in this thesis.

1.1 Review of Evolution of Wireless Technology

With the fast improvement of wireless communication, remote correspondence has improved over the years due to the implementation of advanced heterogeneous systems [1]. After 4G communication, the next generation of wireless communication has drawn attention called the fifth generation i.e., 5G has drawn attention. The next generation of wireless technology will be advanced as compared to previous generations that are first introduced commercially in 2009. As compared to 4G whose speed is up to 100 Mbps, 5G speeds could reach 10 gigabits per second. With this high-speed network, high-definition (HD) movies of more than 1 GB can be downloaded easily. The transmission speed as well as the bandwidth of the 5G network increases which will be needed to accommodate added demands from the "internet of things" [2 - 3]. 5G will provide a direct link between many devices and services like user experience continuity and mission-critical services [4]. The multiband smart antenna is the basic condition for 5G applications. It is categorized by an adaptive array that changes the pattern of the beam according to the user and interference movements. For the direction of arrival (DOA), estimation null enforcement, digital beamforming is used [5 - 7]. Advanced generation systems are introduced to overcome the limitations of previous generations such as high speed, bandwidth, capacity, quality digital video conferencing, online gaming, and availability of the network all the time at any place [8]. The evolution of cellular technology over the previous versions is shown in Figure 1. The first-generation communication was introduced in 1980 and is popularly known as AMPS (Advanced mobile phone system). It utilized a frequency re-use concept supporting 5 to 10 times more users than that of IMTS (Improved mobile telephone system). But 1st generation systems were prone to hindrances like insecurity and full-duplex analog mode of communication. Some of the limitations of 1st generation were overcome by the 2nd generation communication systems which were launched in 1990 utilizing GSM (Global system for mobile communication) standard (See Figure 1.1). The 2G systems were digitally encrypted and more efficient on the spectrum.

They have paved the way to text messaging services. It was introduced in 1995 which was an amalgamation of packet switch networks and GSM possessed data rates up to 160 kbps. This technology is usually referred to as 2.5G. The Evolution (EDGE), uses 8 PSK modulation which indeed provides fast internet services as the e-services were becoming more prevalent during this phase [9]-[10]. In the case of 3G, the base stations upgradation cost was very high and the base stations were needed to keep closer to each other which increases the cost further. The long term evolution technology was added to 4G which provides ultra-high-speed broadband wireless network [11].
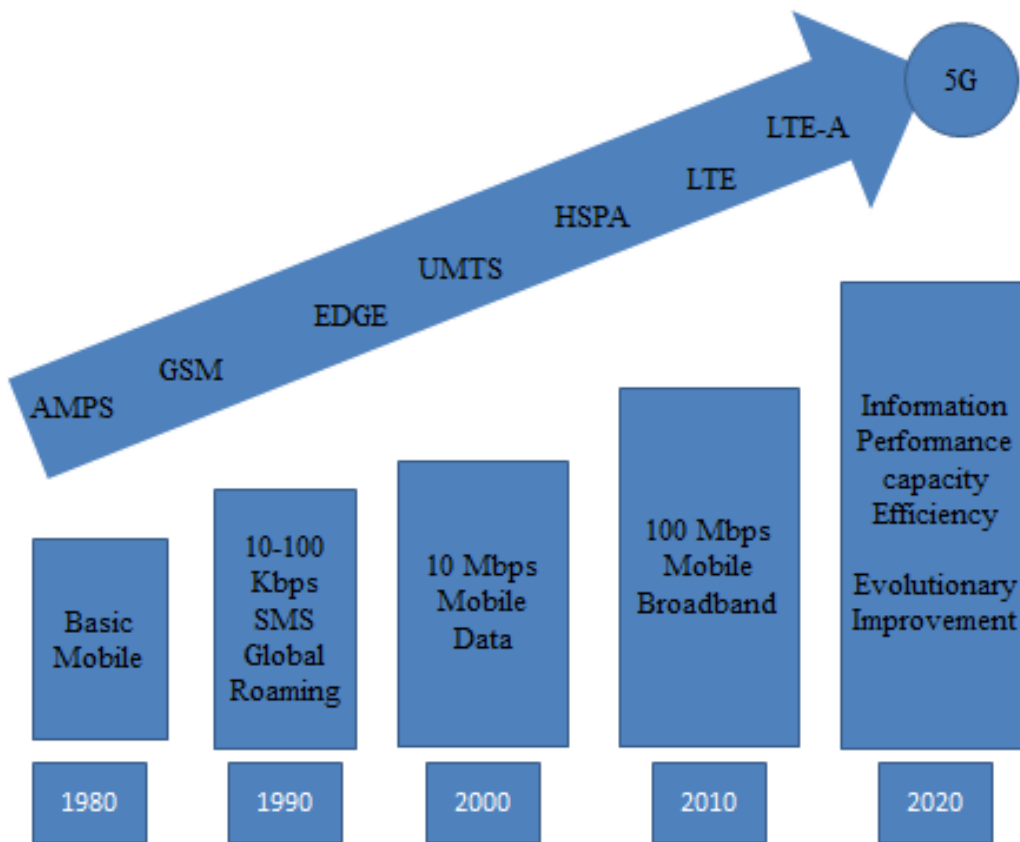
Figure 1.1: Evolution of wireless technology.

1.2   5G Technology

After 1G, 2G, 3G, and 4G, the impending 5G is the fifth-generation wireless technology, which is a new global wireless standard. In comparison to earlier technology, 5G is supposed to deliver more connectivity. 5G claims to simply improve cellular capabilities by improving

3

mobile capacity and data rates while also giving more broadband power. In fact, 5G cellular networks are 10 to 50 times faster than prior generations [12]-[13]. The new applications like Internet of Things (IoT), Device to Device (D2D), Machine to Machine (M2M) communications, Internet of Vehicles (IoV) can be implemented by 5G technology [14]-[15].

2.2   5G Expected Spectrum

To meet the future expectations of advanced new coming wireless technology i.e., 5G, more spectrums need to explore for 5G services. To meet market demand, 5G would require a considerable amount of new harmonised spectrum, thus clearing prime bands should be prioritised. The 5G spectrum is divided into three parts:

i)   Lower Band

ii)   Mid-band

iii)   Higher Band

i)   Lower Band: This is a sub-1 GHz band that allows for widespread coverage in urban, suburban, and rural regions, including indoors. Increased low-band capacity is essential to close the digital divide by creating greater equity between urban and rural broadband connectivity.

ii)   Mid-band: It provides a good combination of coverage and capacity advantages. The majority of commercial 5G networks use spectrum in the 3.3-3.8 GHz region.

In the long run, more spectrum will be required to sustain 5G service quality and fulfill expanding demand (e.g., 3.3-4.2 GHz, 4.8 GHz and 6 GHz).

iii)   Higher Band: For mobile, the GSMA recommends supporting the 26 GHz, 28 GHz, 40 GHz, and 66-71 GHz bands.

There are new challenges to meet link quality requirements at mm-waves frequencies:

➢   Impairments are not an issue at sub-6 GHz but become more problematic at mm-wave frequencies.

➢   With wider channel bandwidths expected at mm-wave frequencies, common signal

impairments impact baseband and RF designs.

➢ 5G radio systems use multi-antenna spatial diversity and beam steering techniques on both base stations and mobile devices to overcome these challenges [16].

1.4 Requirements of the Antennas for Future Wireless Technology

In wireless communication technology demand of efficient transmission and reception of the signal is rapidly increasing in laptops, smartphones, and satellite communication. Therefore, the antenna plays a key role in any wireless communication systems for the transmission and reception of signals. The role of an antenna is to convert electronic signals into electromagnetic signals or vice-versa. The IEEE definition of the antenna is "an antenna is a transitional structure between free space and a guiding device that allows radio waves to be transmitted or received [17]. The antenna has following features like high gain, wide bandwidth, low ohmic losses, and high radiation efficiency which is highly preferable for future wireless technology [18].

5G technology requires the type of antennas having highspeed transmission, high gain for a wide coverage of the network, compact size. For 5G new radio (NR), network capacity beamforming antennas are a very important part for mobile operators.

Beamforming technologies are one key solution for generating high-gain antennas. It is the ability to constructively generate highly directive (high-gain) antenna patterns, especially electronically-steerable patterns. Traditional antennas could only transmit and receive on defined radiation patterns in previous wireless technology. Beamforming antennas, on the other hand, shape their main and null beam directions dynamically based on the location of connected users. The ability of a beamforming antenna to reduce interference, enhance the signal to interference and noise ratio (SINR), and give better-directed signals has been demonstrated [19]-[20].

1.5 Different Types of Antennas

This thesis describes different types of antennas that can be used for the purpose of beamforming/beam steering such as monopole antenna, PIFA antenna, microstrip patch antenna, etc. This section mainly concentrates on antennas and different periodic structures used for beam steering and gain enhancement.

1.5.1   Monopole Antenna

Because of its simple shape, low cost, and omnidirectional radiation pattern, the monopole antenna is widely utilized in wireless communication systems. Monopole antenna is constructed from a straight conductive rod which is perpendicular to a metal ground plane as shown in Figure 1.2. A metal ground plane is used, with respect to which excitation is applied [21].

Conductive rod — Length $= \lambda/4$

Conductive ground plane

Coaxial pin
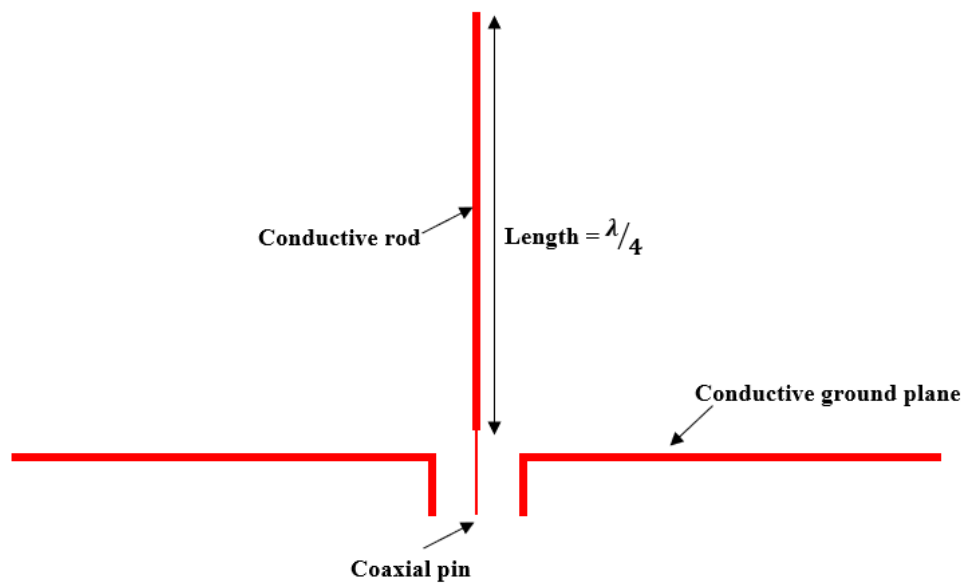
Figure 1.2: Monopole antenna with conductive road and ground plane.

In [22], Chen *et al*. proposed a CPW fed triband planar monopole antenna where multiband operation is achieved by two inverted-L slots. However, the triband operation is obtained but gain of the antenna in three bands is not sufficient for future wireless communication technology. In [23], Boutayeb *et al*. proposed a technique to enhance the gain of the antenna. The mushroom-like cylindrical EBG substrate is used to increase the antenna gain. However, the structure of EBG is made up of metallic rings and vias radially disposed which makes its structure complex.

1.5.2.   Planar Inverted-F Antenna (PIFA)

PIFA antenna was introduced in 1958 by Ronold W. P. King which is the form of bent wire as shown in Figure 1.3. PIFA antenna is a variant of monopole antenna in which the top of the wire is folded down parallel to the ground which also increases the radiation resistance. [24]. The length of the antenna is $\lambda/4$ which makes it low profile and compact. The PIFA antenna is widely used in wireless devices such as mobile phones, tablets, laptops, satellite applications, and missiles [25]. It is comprised of one shorting pin and fed by a probe which is some distance away from the shorting pin. The impedance bandwidth is controlled by varying the air gap between the top and ground of the PIFA antenna, whereas, the impedance matching can be controlled by the distance between feed and shorting. The impedance decreases as the feed gets closer to the shorting pin; conversely, the impedance increases as the feed gets further away from the short edge. This parameter can be used to adjust the impedance of the PIFA. The PIFA's resonant frequency is determined by W.

If this is the case, the shorting pin will run the length of the patch. The PIFA is resonant in this case

If $W = W_p \Rightarrow L_p = \lambda / 4$

Suppose that W=0, so that the short is just a pin (or assume $W \ll L_p$.Then the PIFA is resonant at:

If $W = 0$ then $L_p + W_p = \lambda/4$ [26].
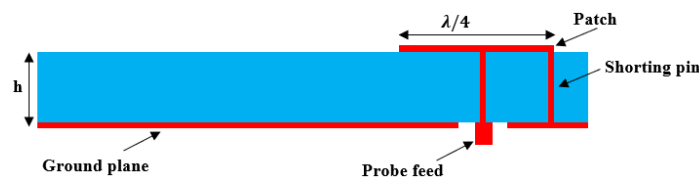
Figure 1.3: Planar Inverted-F Antenna.

1.5.3.   Microstrip Patch Antenna

The concept of a microstrip patch antenna was proposed by Deschamps in 1953. Microstrip

patch antenna is widely used as an internal antenna because of the following reasons:

i.   Light weight

ii.   Manufacturing is inexpensive

iii.   Ability to create high gain arrays

iv.   Polarization diversity

The design of the antenna is such that the metal is printed partially on the upper part and the lower part of the substrate is completely covered by metal. The shape of the patch can be square, rectangle, circle, triangle, elliptical, etc. The rectangular shape microstrip patch antenna is shown in Figure. 1.4 [27].
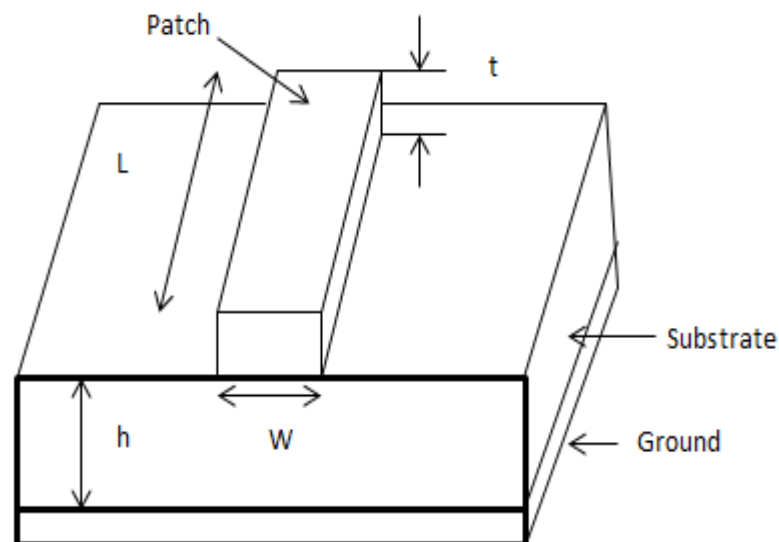
Figure 1.4: Microstrip patch antenna.

1.5.4.   Substrate Integrated Waveguide (SIW)

The substrate integrated waveguide (SIW) is the technology where the substrate is sandwich between two metallic layers and the metallic posts or vias are inserted which connect the lower metallic layer and upper metallic layer of the substrate. It is generally used at millimeter wave because the microstrip line has high radiation losses at high frequency.
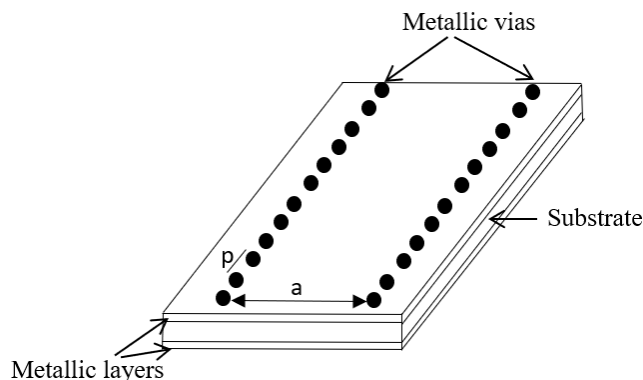
Figure 1.5: Substrate integrated waveguide.

The SIW design equation is given as [108]

$$\varepsilon_{eff} = a - 1.08\frac{d^2}{p} + 0.1\frac{d^2}{a}$$

where 'w_{eff}' is the effective width, 'd' is the diameter of the vias and 'p' is the separation between the vias.

1.6.   Different Types of Periodic Structures

These periodic structures can be in the form of AMC, uniform or non-uniform superstrate, or the periodic absorber blocks that change the behavior of antennas to provide desired radiation characteristics.

1.6.1.   Artificial Magnetic Conductor (AMC)

When placed on a grounded dielectric substrate, planar periodic metallic arrays operate as artificial magnetic conductor (AMC) surfaces and introduce a zero degree reflection phase shift to incident waves, as shown in Figure 1.5. AMCs' reflection phase crosses zero at only one frequency in practice (for one resonant mode). Because these phase values would not produce destructive interference between direct and reflected waves, the useable bandwidth of an AMC is generally specified as on either side of the central frequency.
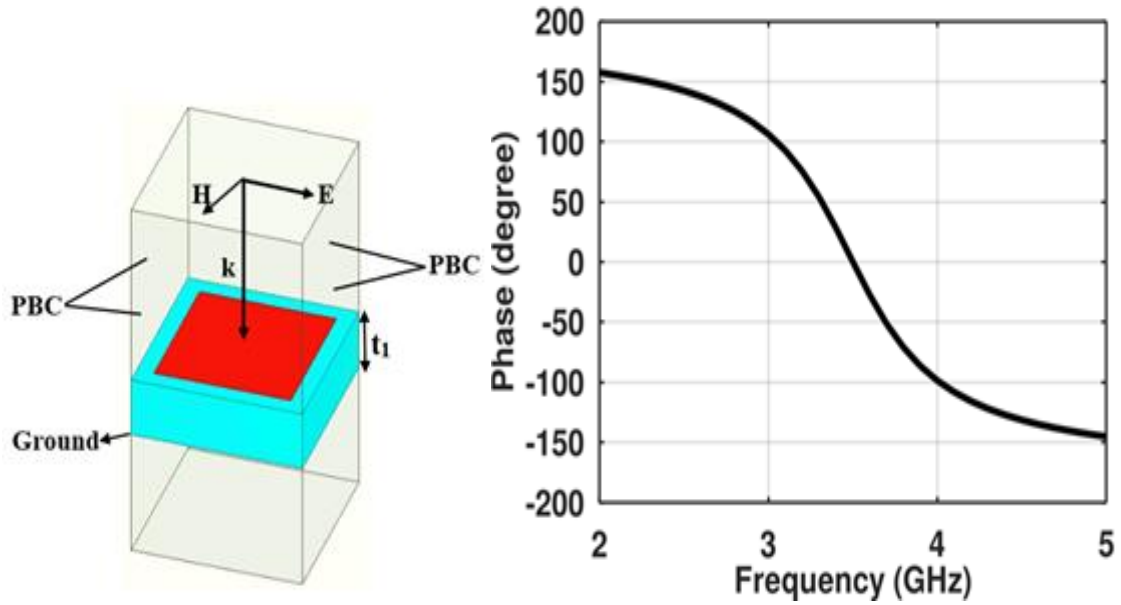
Figure 1.6: AMC unit cell: (a) isometric view; (b) reflection phase.

1.6.2.   Uniform Superstrate

The superstrate over an antenna helps to create a cavity effect in line with the Fabry-Perot effect (See Figure 1.6) and the transmission and reflection behavior of the substrate decides the overall gain of the antenna-superstrate combination. Proper selection of AMC and superstrate can provide high gain to the antenna. Mostly, a uniform superstrate is used for this type of function. Figure 1.6 shows the uniform metasurface superstrate.

(a)   (b)
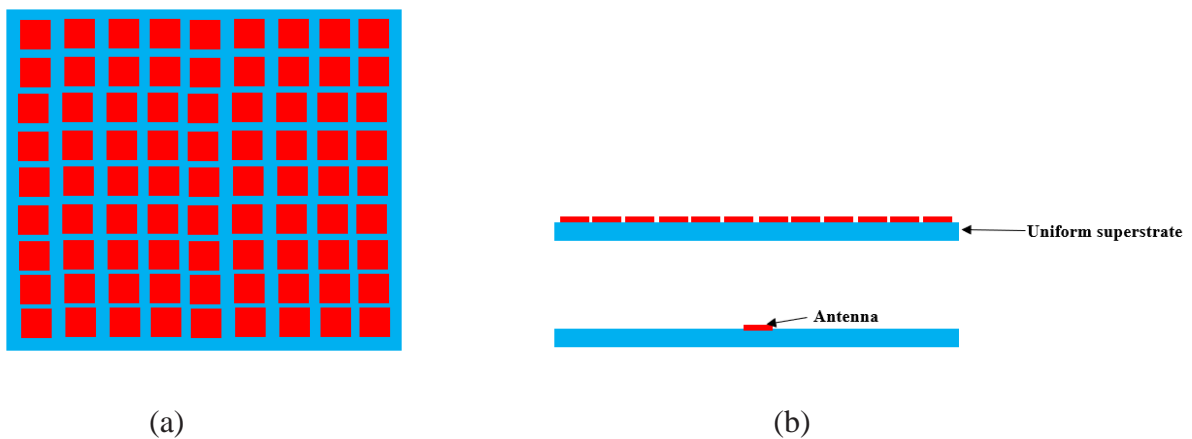
Figure 1.7.: Uniform superstrate: (a) top view; (b) side view.

1.6.3. Non-uniform Superstrate

Non-uniform superstate instead a of uniform superstate not only provides gain but can also steer the beam in the desired direction. This section explores non-uniform superstrate and its design for high gain antennas. Figure 1.7 shows the geometry of the proposed superstrate which comprises of metallic patches of different sizes. In order to steer the beam ina direction away from the broadside, there should be phase variation for waves emanating from different locations of the superstrate. This phase-varying behavior is provided by a nonuniform metasurface printed on the dielectric substrate acting as a superstrate.

(a)   (b)
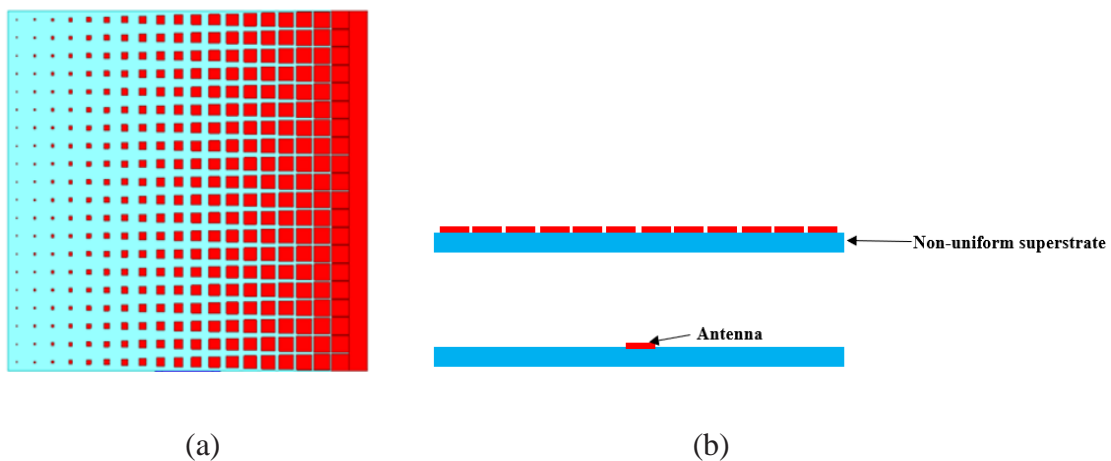
Figure 1.8: Non-uniform superstrate: (a) top view; (b) side view.

1.7.   Literature Survey

1.7.1.   High Gain Antenna

We discussed the use of various periodic structures is utilized for the gain enhancement, beamforming, and beam splitting in the conventional antennas in previous sections. This section concentrates on the different methods to obtained high gain and beamforming for 5G applications.

Planar inverted-F antenna (PIFA) is suitable for low-profile, compact wireless devices. Another benefit of the PIFA antenna is the integration with other electronic components. Different low- profile, and flexible textile PIFA for Wireless Local Area Network (WLAN)

applications are reported in [28–31]. With the advantage of low profile, wide bandwidth, PIFA has some limitations of low gain, backward radiations, high specific absorption rate (SAR), and complicated fabrication [32].

In [33], Chen *et al*. proposed two PIFA arrays in which one PIFA has shorting pins at outer edges and another PIFA has shorting pins at the inner edge which broaden the bandwidth as well as increase the gain of the antenna. Whereas, Sievenpiper *et al*. show that the performance of the antenna in terms of bandwidth, gain, and efficiency can be improved without compromising the size of the antenna with the help of an artificial magnetic conductor (AMC) [34]. The function of AMC is to reflect the wave at 0° phase and add in phase with an antenna which creates constructive interference, improving the bandwidth and gain respectively [35]-[36]. In [37], Gao *et al*. achieved miniaturization and high gain by using high permittivity metasurface (MS) placed over the antenna.

Whereas in [38], Yang *et al.* has proposed a thick cavity used as an antenna magnetic ground plane which achieved 1.73 dB peak gain enhancement. Furthermore, the performance of the antenna is enhanced by a 2×2 antenna array.

The SAR reduction is one of the challenges for any antenna, which increases when a mobile phone is close to the human body. Therefore, there is a need for the antenna to work close to the human body without affecting SAR. The magneto dielectric nanocomposite substrate is used to reduce the SAR value and enhance the performance of the antenna [39]. Lai *et al*. proposed additional pair of parasitic shorted patches to suppress the backward radiations which help to obtain 12.23% impedance bandwidth and gain of 6.5 dB gain [40]. The metasurface units consist of non-uniform metallic patches which are fed through two microstrip coupled slots. A good filtering performance is achieved by shorting via the separation of two slots [41]. In [42], Joubert *et al*. proposed a cavity-backed printed slotted antenna fed by CPW in which the unidirectional radiation pattern is obtained by an AMC reflector. Furthermore, the antenna performance is enhanced using a newly devised EBG structure. However, Ta *et al*. proposed a T-shape slit-based AMC unit cell is used as a reflector of the antenna which achieved broadband characteristics [43]. Whereas, miniaturization and wideband are achieved using AMC as reported in [44]. Hossain *et al*. proposed a PIFA antenna which achieved 2.08 and 2.29 W/kg 1g SAR in the human head at 900 and 1800 MHz

bands respectively [45]. The different SAR values have been evaluated at different distances from the head as reported in [46]. In [47], Choi *et al.* proposed two 28 GHz beam steering antenna sub arrays for fully metal-covered 5G cellular handsets with reduced SAR values. Moreover, the effects of the hand on PIFA antenna have been reported in [48]. For different planar and bending scenarios, the SAR reduction has been achieved using AMC and is investigated in [49]. In [50], a miniaturized slotted Jerusalem Cross (JC) AMC ground plane is integrated on an M-shaped monopole antenna which achieved a gain of 4.8 dB and SAR value of 0.683 W/kg. In [51], wide operational bandwidth is achieved by a new type of PIFA antenna which provides quasi-omnidirectional type radiations. However, Ali *et al.* proposed an ultrawide band microstrip patch antenna where suppression of cross-polarization is achieved by defective ground plane [52]. Can *et al.* present a design which reduces the specific absorption rate (SAR) using AMC [53]-[54].

Monopole antennas are used in wireless communication because of their simple design, quarter wavelength length, low cost, and omnidirectional radiation pattern. Over a considerable portion of its frequency spectrum, a monopole antenna has a high response impedance. The omnidirectional radiation property of the monopole antenna makes it suitable for 5G technology [55]-[60].

Tan *et al.* presented a dual-band with dual sleeve monopole antenna was proposed in [61], which operates in 900 MHz and 1800 MHz frequency bands. Tan et al. proposed monopole antenna with crinkle fractal structure for multiband applications was presented in [62].

Deng *et al.* proposed a monopole antenna in which a sleeve was introduced to increase the gain to 3.9 dBi [63]. Moreover, Jiang *et al.* proposed a compact flexible anisotropic metamaterial coating is presented in [64], which shows bandwidth enhancement (2.15-4.6 GHz) and increased gain up to 5.46 dBi.

Panahi *et al.* presented a polarization reconfigurable monopole antenna in [65], which achieved LHCP/RHCP using two PIN diodes and obtained a maximum gain of 1.2 dBi. Furthermore, Koohestani *et al.* presented that the gain and performance of the antenna can be enhanced by using an artificial magnetic conductor (AMC) [66]. Abbasi *et al.* proposed a novel vertically polarized, omnidirectional low-profile antenna was proposed in [67] and it shows a 5.5% of bandwidth and 3.7 dB gain.

Yuan *et al*. presented a low-profile vertical monopole element with a standard metallic reflector plane [68]. Lin *et al*. report a pair of double-printed crossed dipoles employing vacant quarter-rings in [69], but with strong back radiation which is removed by using square AMC. In [70], Wu *et al*. a horizontally polarised circular loop antenna and a vertically polarised low-profile monopole antenna make up the proposed antenna. However, Cao *et al*. obtained a conical pattern and gain of 6 dBi through square-shaped AMC [71]. Jackson *et al*. proposed gain enhancement methods for printed circuit antennas in [72]. Jackson *et al*. presented the importance of leaky waves in the fundamental physics of directional beaming at microwave and optical frequencies [73]. In [74], Kim *et al*. enhanced the gain of the antenna dielectric superstrate. Whereas, Mittra *et al*. presented using three different superstrates to conduct a comparative investigation of directivity enhancement of microstrip patch antennas in [75]. Li *et al*. proposed a Fabry Perot antenna where directivity is enhanced by a stepped dielectric slab superstrate [76]. Zhang *et al*. proposed microwave flat gradient index (GRIN) lenses where ultrawideband and high gain is achieved by partially infilled dielectrics with a varied periodicity and artificially engineered dielectrics (AED) [77]. Arya et al. presented meta-atoms and artificially engineered materials for antenna Applications [78]. Zhang *et al*. proposed a planar graded-index (GRIN) lens in which gain enhancement is achieved by GRIN lens which transforms spherical wavefronts into planar wavefronts [79].

It can be said from the above mentioned literature review that the artificial magnetic conductor (AMC) and superstrate are attractive for achieving high gain, low SAR, and wide bandwidth in conventional antennas. But it does not fulfill the requirements of modern wireless communication systems because it is very difficult to achieve beamforming, beam scanning, and beam splitting. So, researchers are finding some other techniques to remove these drawbacks.

1.7.2. Beamforming and Beam Splitting Antenna

In 5G, the beam steering capability of the antenna plays the main role for efficient coverage to all users [80]-[82]. Beam steering is the solution to today's network problems such as call drops, multipath fading in crowded areas [83], [84].

Arai *et al*. proposed a leaky wave optical beam scanning antenna which achieved 10° beam scanning with the help of waffle and waffle iron waveguides [85]. McManamon *et al*.

presented many beam steering methods reported in [86], which shows one of the methods of beam steering, Birefringent Prisms. However, this method is limited as it requires prism thickness of more than 8 cm which may create the problem of beam walk off [87], [88] when the beam needs to be steered by 20°. The precise beam steering is obtained using a 1D optical phased array on silicon-on-insulator which achieves 2.3° at a wavelength of 1550 nm and 14.1° steering. The design is, however, limited due to its high cost and complication in designing with low beam scanning presented by Van Acoleyen *et al*. [89].

Ji *et al*. proposed a reconfigurable partial reflecting surface (PRS) structure which was deployed to achieve beam steering from -15° to 15° as reported in [90]. Tanoli *et al*. proposed a microstrip leaky wave antenna which achieved total beam scanning of 78° [91]. Whereas, Symeonidou *et al*. achieved 0° to 40° beam scanning with the help of an electronically controlled microstrip antenna and changing the capacitance value [92].

Dias *et al*. obtained tilted beam at ±15° by combining parasitic elements with inserted capacitances [93]. Luther *et al*. proposed a parasitic phased array antenna with varactors and tuning capacitance which provides continuous scanning of ±15° [94]. However, Khairnar *et al*. proposed a reconfigurable microstrip Yagi antenna which achieved beam scanning from -40° to +40° in H-plane with the help of two hexagonal slotted tunable parasitic elements with the gain of 3.36 dBi [95]. Li *et al*. presented a beam steering antenna based on a parasitic layer which achieved beam steering of -30°, 0°, +30° and used a grid of 5× 5 electrically-small rectangular-shaped metallic pixels on the upper layer of the parasitic layer which are connected by switches [96]. Besides, 360° beam steering is presented in [97] by combining electronically steerable parasitic array radiator (ESPAR) antenna and the water antenna, but it makes the design complex and cannot be easily designed. Ourir *et al*. proposed a phase varying metamaterial for steerable directive antennas where $\pm20^o$ steer beam is obtained [98].

The above work is addressed in chapter 4.

The majority of antennas are measured in wavelengths, and the short wavelengths of mm-waves allow for small antennas with high directivity [99]. In [100], the authors use three identical sub-arrays of patch antennas that are fed by switching to certain sub arrays to achieve beam steering capability in the theta plane ranging from -90° to $+90^o$. In [101], Hong et al. proposed stacking of six pieces of the substrate, placed in a radome which improved the

radiation pattern distorted at mm-waves. In [102], Hashem *et al.* proposed a six-element MIMO PIFA antenna, whereas, Morshed *et al.* proposed a PIFA antenna with slots to increase the gain and bandwidth [103]. In [104], Wang *et al.* presented an array of 4×4 patch antenna which improves the gain of the antenna with a soft surface structure which suppressed the surface wave.

An antenna covering the frequency range of 53 GHz to 71 GHz is proposed, with a bandwidth of 29 % and a gain of 17.5 dBi. Park *et al.* [105] combined two radiating elements to obtained high gain and tilted beam into two directions. In [106], Aliakbari *et al.* show that the adjustment of the slots results in increased impedance matching and axial ratio. Kornprobst et al. developed an mm-wave patch antenna with a wide beamwidth of 100° to 125° achieved by parasitic patches with multiple resonances and a 13 % bandwidth that covered the frequency range of 34.1 to 38.9 GHz [107]. Agrawal *et al.* proposed a SIW leaky-wave horn antenna which achieved radiation pattern improvement by varying the number of slots [108]. However, Faezi *et al.* discussed radiation pattern improvement carried out by conducting post around the slots which suppress the surface wave and remove the ripples from E-plane [109]. Whereas, Panda *et al.* proposed tuning fork-shaped monopole antenna where surface waves suppressed by HIS which increase the gain as well as obtained wide bandwidth [110]. In [111], Feng et al. demonstrated that a layer of three substrates may reach 19.4 % bandwidth (4.69-5.7 GHz) and 7.32 dBi gain, with the top superstrate consisting of 77 square patch cells metasurface. In a multilayer substrate for wideband operation, seamless integration of other devices is problematic, which is achieved in [112] by using a MIMO dual-band mm-wave monopole antenna.

In Katare *et al.* proposed a split beam antenna where a split beam is achieved using digital metasurface along with a lens in which radiation in boresight direction is improved through the lens, and beam splitting is achieved through digital metasurfaces [113]. However, [114] proposed an ultra-thin polarization beam splitter using the property of the transmissive phase gradient metasurface (TPGM). Jiang et al. suggested a symmetrical dual-beam bowtie antenna for 5G MIMO applications in [115], which utilised three pairs of metamaterials (MTM) arrays. A wide beam was achieved using the first pair of MTM arrays with a high refractive index, while the second pair of MTM arrays were configured so that the single wide beam splits into dual beams at 30°. Khidre et al. presented a wideband dual-beam U-slot microstrip

antenna where dual radiation beams with wide bandwidth directed at $\pm35^o$ and -33° is reported in [116].

In [117], Park *et al.* proposed a four-element planar folded slot phased array antenna which achieved beam scanning of $\pm50^o$. However, Guan *et al.* improved beam scanning rate by slow-wave substrate integrated waveguide structure [118]. Whereas de Paula *et al.* presented an air-filled substrate integrated waveguide 1×4 antenna array which shows $\pm50^o$ beam scanning [119]. Ansari et al. presented a complex structure called the Butler matrix 46, which was combined with a six-element linear antenna array to achieve 45° beam scanning in [120].

From the above-mentioned literature review it is evident that the artificial magnetic conductor (AMC) along with non-uniform metasurface superstrate, RF absorber, and SIW are attractive for achieving beamforming, beam scanning, and beam splitting which is the requirements of upcoming 5G wireless technology.

1.8. Motivation and Objective of the Thesis

In the upcoming wireless communication technology i.e., 5G, there is an extensive requirement of the high gain, beamforming, beam scanning, and beam splitting antenna. Moreover, antenna designers are also more focused on mid-band, sub-6 GHz, and millimeter-wave bands along with highly directional, high radiation efficiency, and compact antennas. To get the high gain required for 5G communications in millimeter frequencies, beamforming technology plays a major role. There are different types of large networks used for beamforming, such as Butler matrix, Rotman lens, phased array antenna because beam steering requires it. However, these methods increase the complexity, weight, and cost of the design. In order to overcome these issues, disruptive beamforming can be used.

The literature survey reveals that many research groups are working in the field of 5G antenna design and also, they got success to some extent. Due to the above requirements, our research work is mostly concentrated on enhancement of features such as gain, beamforming, and beam splitting, beam steering and beam reconfiguration etc., with different periodic structures which are studied in details.

Some of the following challenges are motivating factors to conduct research work in the field of 5G antennas:

➢ Combining different periodic structures to enhance the gain of the antenna.
➢ Specific absorption rate (SAR) reduction using artificial magnetic conductor (AMC).
➢ Come up with different techniques to achieve beam scanning, beamforming.
➢ Isolation and coupling reduction

On the basis of the above factors, the main objective of this thesis is to design and

analyze of planar inverted-F antenna, monopole, and microstrip patch antenna along with different periodic structures.

The main objectives of this thesis are listed below:

➢ Achieving high gain, wide bandwidth, and SAR reduction in PIFA antenna using AMC.
➢ Gain enhancement of monopole antenna using AMC and superstrate.
➢ By utilising a non-uniform superstrate, develop beam steering ability in monopole antenna.
➢ Obtain wideband and high gain and pattern reconfigurable using Eccosorb MCS absorber.
➢ Split beam into two directions using Eccosorb MCS absorber.
➢ Achieve beamforming using SIW, metasurface, and EBG structure in two-port MIMO antenna.
➢ By using simulation tools such as Ansys HFSS for optimizations of the antenna parameters.
➢ Fabricate prototypes antennas to validate the simulation results such as input impedance bandwidth, gain, radiation patterns, and so on.

1.9. Design Guidelines of the Antenna

Figure 1.8: shows the function of the work plan in flow chart format and divides the whole work into majorly seven sub-sections which are given below:

➢ Choose the Frequency of operation of the antenna and select the material and its dielectric constant.

➢ Use the design equations for finding the resonant frequency.

➢ Use appropriate techniques to achieve high gain, beamforming, and split beams

➢ Designed the proposed antenna structure by using Ansys HFSS and apply proper boundary conditions.

➢ Conduct parametric analyses to know the effect of different parameters on the Antenna performance.

➢ Once the antenna design is finalized start the fabrication process for the prototype antenna.

➢ Measured the fabricated prototypes for validation of the results.
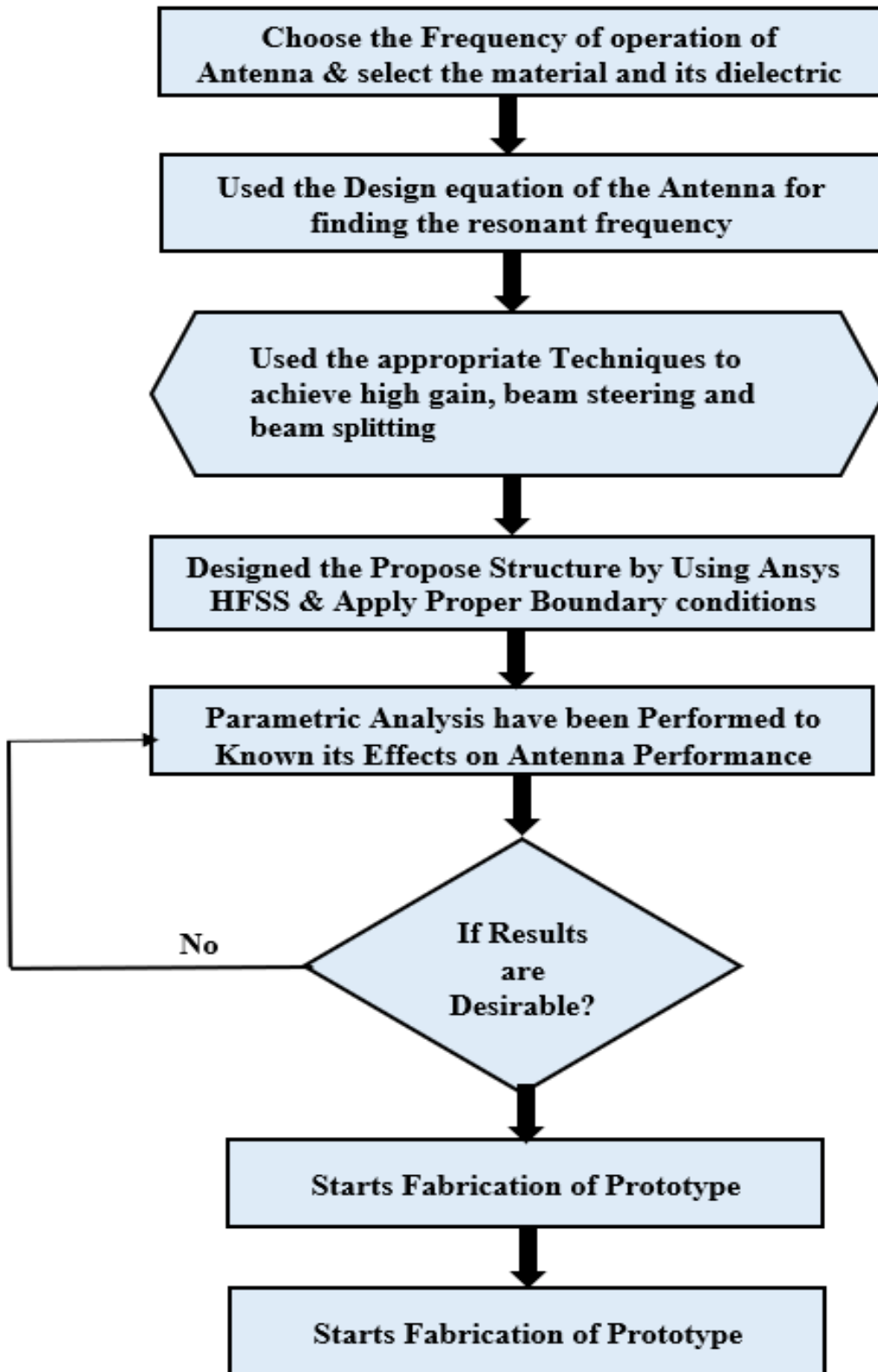
Figure 1.9: Design methodology of the proposed antennas.

1.9.1.   Organization of the Thesis

The thesis has been divided into eight chapters which are given as:

Chapter-1: In the first chapter, a brief introduction of 5G technology and the expected spectrums are described. Next, the requirements of the antennas in future wireless technology are also described. In the end, for beam steering and gain enhancement, different types of periodic structures are also explored. This introduction lays the foundation that is needed to appreciate the work performed in this thesis.

Chapter-2: In the second chapter, we start with the design of a compact planar inverted-F antenna (PIFA). It is found that the gain and bandwidth of the antenna are low while the SAR value is high which may not be useful for 5G and other applications. To counter low gain, the gain enhancement of the PIFA antenna is explored by applying AMC. On the other hand, the SAR contribution leading to the undesired electromagnetic radiation towards the human body is analyzed using three- and four-layer of the human tissue models. Once the reason for high SAR is known, the SAR reduction technique with AMC is used, reducing SAR to a low value. The value of SAR of the proposed antenna is found to be lower than the IEEE standards which shows the effectiveness of the AMCs. When measured, the proposed antenna has an impedance bandwidth of 4.8–6.7 GHz (33 % with center frequency at 5.75 GHz) and a maximum gain of 7.6 dBi, making it appropriate for WLAN, satellite uplink C-band, and sub-6 5G applications.

Chapter-3: In the third chapter, we designed a coplanar waveguide-fed monopole antenna. Traditional planar monopole antennas have low gain and might not be usable for many applications due to it. While the use of AMC and superstrate is used for gain enhancements, it has never been employed for planar monopole antennas in a single design. So, we approached this low gain problem in a systematic manner. Hence, to achieve high gain, we use AMC as well as superstrate for enhancing the forward radiation from the antenna. However, superstrates demand for materials with high dielectric constants but these materials are either not available commercially off-the-shelf or are very expensive compared to traditional dielectrics. This motivated us to study three different superstrates and discuss how they can be used in place of each other without sacrificing antenna performance. Finally, one of these three superstrates is fabricated with the monopole and AMC combination. The

fabricated coplanar waveguide fed monopole antenna with AMC and superstrate shows the measured impedance bandwidth of 15.7% (3.2-3.75 GHz) and has the maximum gain of 7 dBi which is well suited for 5G and WiMAX applications.

Chapter-4: In the fourth chapter, we explored a beam-steering antenna based on a non-uniform metasurface superstrate and AMC as beam steering with low scan loss is going to be a necessity for 5G communications. The proposed antenna in this work can steer the beam along $\theta = -18°$ and $18°$ with the superstrate and along $\theta = 0°$ in the absence of the superstrate with almost zero scan loss. The antenna, working at 3.5 GHz, due to these qualities, is an ideal candidate for 5G, WiMAX, and WLAN applications.

Chapter-5: In the fifth chapter, we look at how an Eccosorb MCS absorber can be used to transform the radiation pattern of a slotted planar inverted-F antenna (PIFA). The structure of the PIFA antenna with and without absorber was analysed to see whether the antenna performance might be improved. We show that by using an absorber, the radiation pattern may be transformed, producing a radiation beam in the desired direction while also increasing the antenna's gain at the same time.

Chapter-6: Extending the work performed in the fifth chapter, we designed a planar inverted-F multi-beam antenna using RF absorbers in the sixth chapter. The multi-beam antennas mostly require a complex system of multiple antennas such as a phased array or MIMO antennas and make the system bulky as well as power-hungry. The proposed antenna circumvents these limitations and provides multiple beams from a single antenna with wide angular coverage. The designed antenna achieves a multi-beam behaviour by six slabs of absorbers placed periodically between the PIFA patch and substrate to split the beams into two directions at $\pm26°$. This design fulfills the multibeam requirements not just for 5G but for other latest communication systems too.

Chapter-7: In the seventh chapter, we design a circularly polarized MIMO antenna for the 5G band at millimeter wave frequencies (23.5-25.5 GHz). As microstrip or CPW type of transmission lines incur a high loss at millimeter frequencies, the antennas call for SIW-based designs for low loss. Therefore, a novel SIW structure is employed to achieve beamforming in this chapter. This work comprises different types of vias and slots that achieve multibeam in the 1st and 2nd quadrant with 120° angular coverage. The introduction of slots also improves

the axial ratio and antenna gain. The proposed antenna also benefits by using EBG and metasurfaces to produce right-handed circular polarized radiations within the desired band of 23.5-25.5 GHz with good return loss. Finally, the MIMO's diversity properties have been investigated. In all aspects, the suggested antenna performs well for 5G applications.

Chapter-8: In the end, the eighth chapter consists of the overall conclusion and future scope of the thesis. In this thesis, we designed various antennas like PIFA, monopole, SIW, and microstrip patch antennas to achieve high gain and beam splitting, beamforming for 5G applications. These antennas will be helpful for 5G applications working in frequency bands of mid-band (3.4-3.6 GHz), sub-6 GHz, 19.7 to 30.32 GHz, 24.2-25.7 GHz, and 23.5-25.5 GHz.

In this way, this thesis will discuss gain enhancement, beam splitting, and beamforming techniques using AMC, superstrate, RF absorbers, and metasurface superstrate.

1.10   List of Publications

1. **Verma, A**. and Srinivasa, R.N., 2021. Wideband Slotted Planar Inverted-F Antenna using Eccosorb MCS Absorber for Millimeter-Wave Applications. *Indian Journal of Pure & Applied Physics (IJPAP)*, 59(6), pp.421-428.

2. **Verma, A**. and Raghava, S.N., 2021. Circularly polarized hybrid mode substrate integrated waveguide antenna for two quadrant scanning beamforming applications for 5G. *International Journal of RF and Microwave Computer-Aided Engineering*, 31(10), p.e22798.

3. **Verma, A**., Arya, R.K., Bhattacharya, R. and Raghava, S.N., 2021. Compact PIFA Antenna with High Gain and Low SAR Using AMC for WLAN/C-band/5G Applications. *IETE Journal of Research*, pp.1-11.

4. Verma, A. and Raghava, N.S., 2021. Beam Splitting Planar Inverted-F Antenna for 5G Communication. *Defence Science Journal*, 71(6), pp.791-797.

5. **Verma, A,** N. S. Raghava, Raghava, S.N., 2021. An era of new future wireless 5G technology and its aspects: A review. International Journal of Systems, Control and Communications.

6. **Verma, A**. and Raghava, N.S., 2017. Compact slotted meandered PIFA antenna for wireless applications. *Jour of Adv Research in Dynamical & Control Systems*, 9(11).

7. **Verma, A**. and Raghava, S.N., 2019, December. Circularly Polarized Slots in T-Shape based Substrate Integrated Waveguide PIFA Antenna for 5G Applications. *In 2019 IEEE Indian Conference on Antennas and Propogation (InCAP)* (pp. 1-5). IEEE.

8. **Verma, A**. and Raghava, N.S., 2018, October. Millimeter Wave Reconfigurable Vivaldi Antenna using Power Divider for 5G Applications. *In 2018 2nd IEEE International Conference on Power Electronics, Intelligent Control and Energy Systems (ICPEICES)* (pp. 1126-1131). IEEE.

9. **Verma, A**. and Raghava, N.S., 2017, Febuary. Compact Slotted Meandered PIFA Antenna for Wireless Application," *Proceedings of IIRAJ International Conference (ICCI-SEM-2K17)*, GIFT, Bhubaneswar, India.

Papers communicated to international journals are

1. **Akhilesh Verma,** Ravi Kumar Arya, N. S. Raghava, Monopole Cavity Resonator Antenna using Artificial Magnetic Conductor and Superstrate.

2. **Akhilesh Verma,** Ravi Kumar Arya, N. S. Raghava, Metasurface Superstrate Beam Steering Antenna with AMC.

Patent published:

1. Multi & Wide Band Millimeter Wave PIFA Antenna Using Multiple Slot For 5G Applications published in 2018.

CHAPTER 2

Compact PIFA Antenna with High Gain using Artificial Magnetic Conductor

2.1 Introduction

With the rapid demands for high data, connectivity, low data traffic has drawn attention towards new wireless technology *i.e.* fifth generation (5G). The demand for low profile and compact wireless devices for advanced wireless service like 5G is high. Nonplanar antennas such as monopole antennas are low profile in nature but they have limitations such as uncontrolled radiation, narrow bandwidth, and low gain. Planar inverted-F antenna (PIFA) is suitable for low profile, compact wireless devices. Another benefit of the PIFA antenna is the integration with other electronic components because of its low-profile nature.

Hence, PIFA antenna is the most prominent solution for the next generation wireless technology.

In literature, the periodic structures i.e., artificial magnetic conductor (AMC) have been used for improving the performance of the antenna [42]. Therefore, several works have been reported on AMC technique to improve the antenna bandwidth, gain, efficiency and to reduce the SAR [43]-[44]. In this work, to enhance the bandwidth and gain of the PIFA antenna, square unit cell AMC is designed as shown in Figure 2.1 (a). The proposed square AMC unit cell is based on Rogers RT/Duroid 5880 of thickness 1.6 mm and permittivity value of 2.2. The top surface of the substrate is covered by metallic square patches and the bottom surface is completely covered with metal. The side length of the square patch is denoted by a $(= a_x = a_y)$ whereas the periodicity of the unit cells is denoted by p ($= p_x = p_y$).

The square patch is centered in the unit cell leaving an equal gap around it. The dimensions of the optimized AMC unit cell are taken as $a = 9.88$ mm with $p = 10$ mm. This size of the AMC gives the zero-reflection phase at 5.6 GHz.
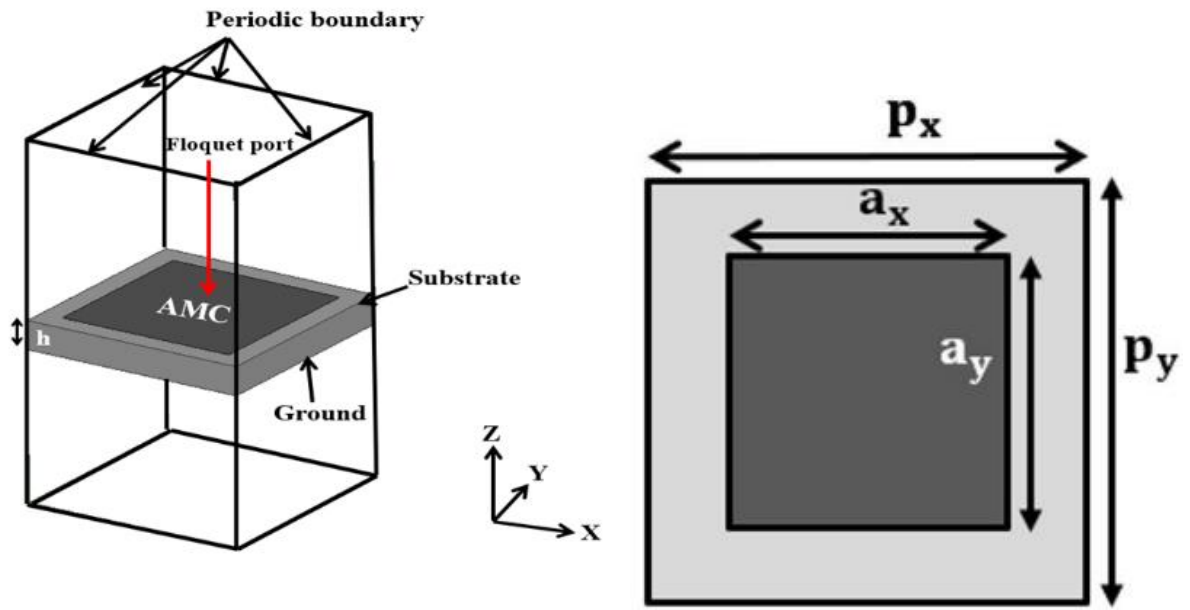
Figure 2.1: AMC unit cells.
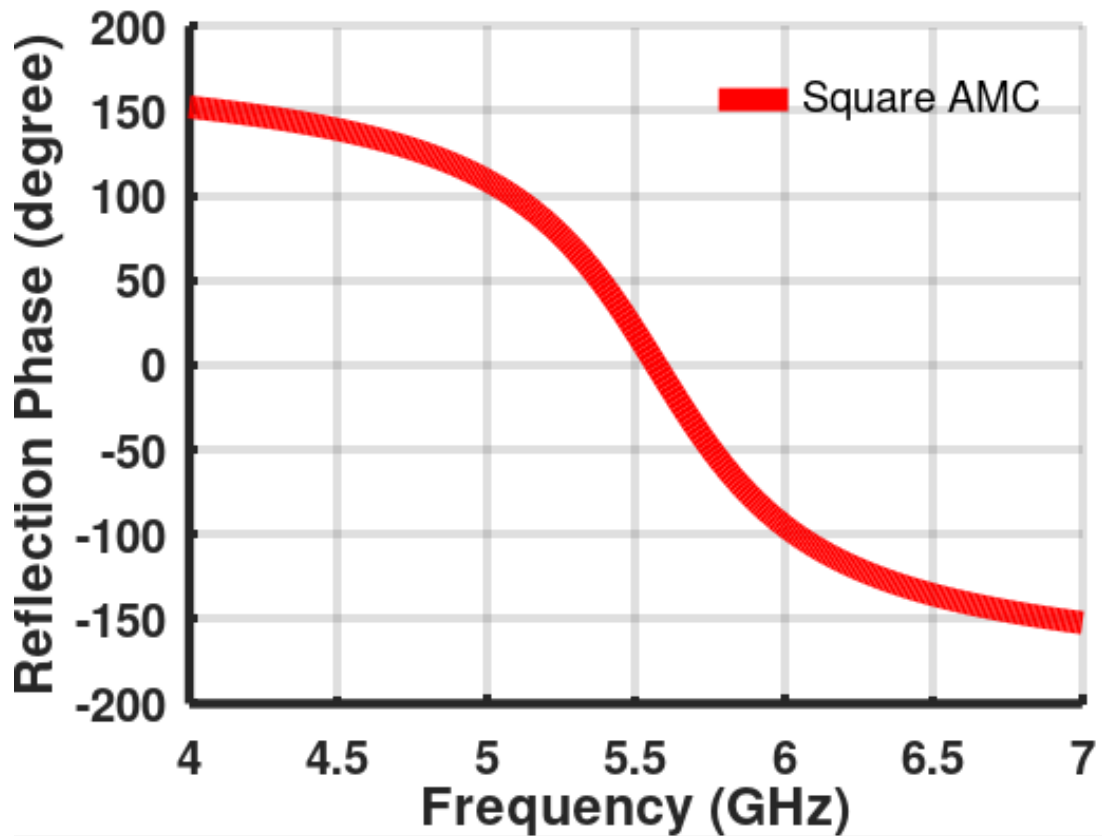
Figure 2.2: The reflection phase characteristics of the AMC unit cells.

2.2   Design Procedure and Parametric Studies of PIFA Antenna

This section contains the antenna design procedure and parametric studies (effect of air gap between patch and ground, length of the antenna, and position between feed and shorting).

2.2.1 PIFA Antenna Design

The geometry of the proposed composite antenna is shown in Figure 2.3. The PIFA antenna with its ground is printed on top of the substrate while the bottom of the substrate touches the AMC structure. The 3D layered structure of the proposed composite antenna is shown in Figure 2.3.
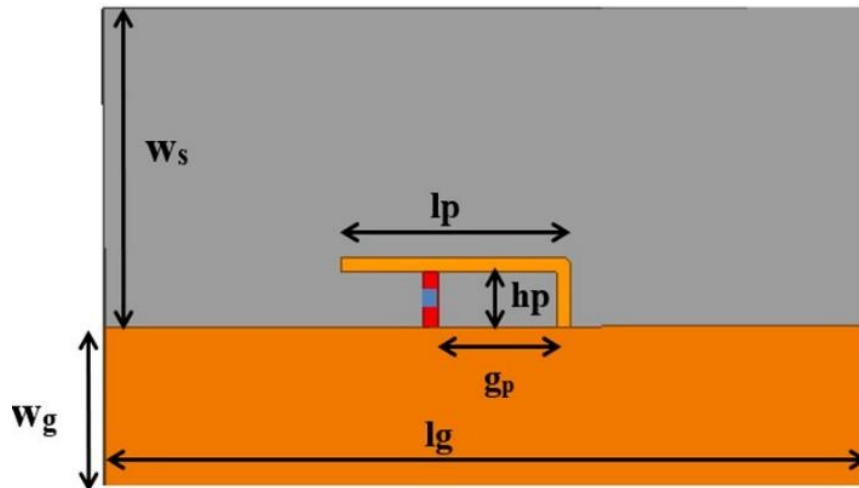
(a)
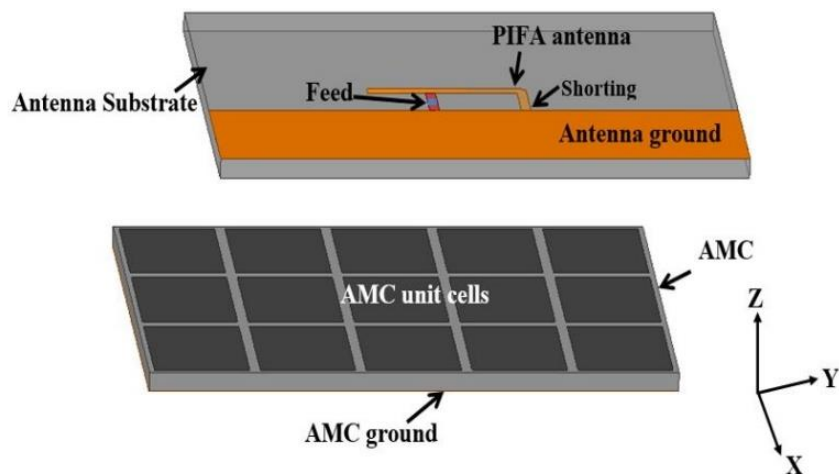
(b)
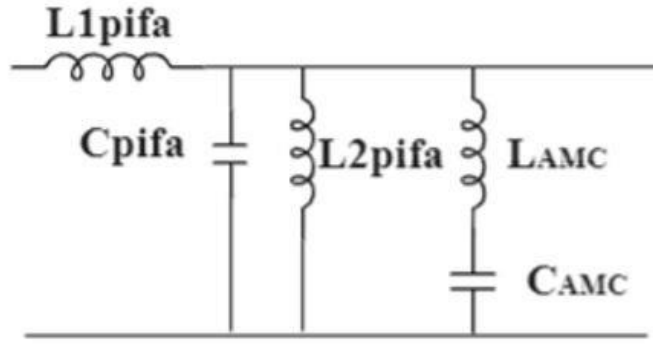
(c)

Figure 2.3: Proposed antenna structure; (a) detailed dimensions of the antenna; (b) 3D layered structure of the antenna; (c) equivalent circuit model of the proposed antenna.

For the top PIFA antenna, the distance between the feed and shorting end is denoted by 'g_p' while the air gap between the PIFA and ground is denoted by 'h_p'.

The design equation of PIFA [31] is given as:

$$f_r = \frac{c}{4(L_p + W_p + h)\sqrt{\varepsilon_r}}$$

Where f_r is the resonant frequency, L_p is the length of the patch, W_p is the width of the patch and h is the air gap. If the width of the shorting pin is less than the width of the patch then $L_p + W_p = \lambda/4$. The equivalent circuit model of the proposed PIFA antenna with AMC is shown in Figure 2.3 (c). The $L1pifa$ and $L2pifa$ denote the inductors and $Cpifa$ is the capacitance of the PIFA antenna, whereas the LAMC and CAMC are the inductance and capacitance created in an AMC respectively.

Figure 2.4 shows the photographs of the fabricated proposed antenna. The photographs also show the connection employed to feed the antenna. The center conductor of the coaxial cable is connected to PIFA and the outer conductor is connected to the ground of the antenna.
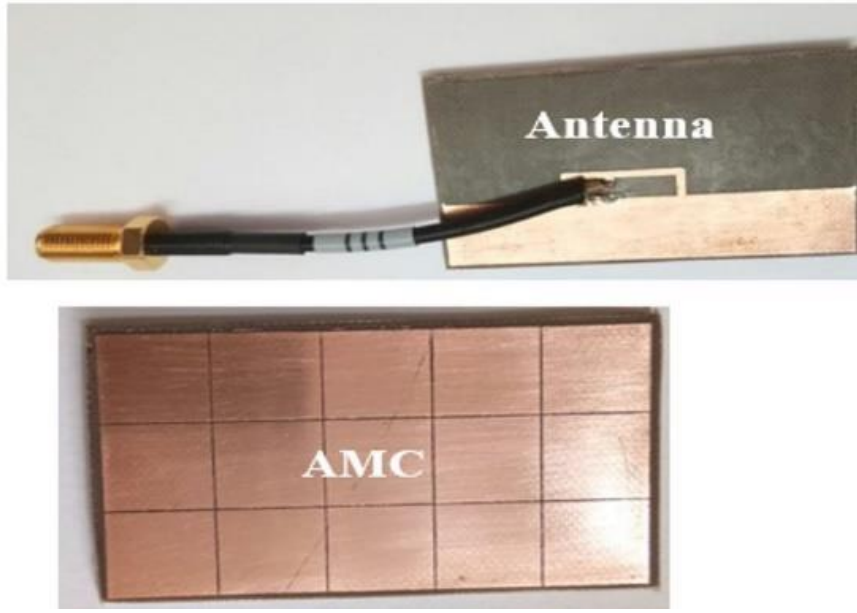
Figure 2.4: Photographs of the proposed antenna.

The optimized parameters of the proposed antenna are found to be: $w_s = 20\,\text{mm}$, $w_g = 10\,\text{mm}$, $l_p = 14.55\,\text{mm}$, $h_p = 3.43\,\text{mm}$, $h = 1.6\,\text{mm}$, $g_p = 7.74\,\text{mm}$, $l_g = 50\,\text{mm}$.

2.2.2 Parametric Analysis

The dimensions of the proposed antenna are achieved by optimization of different dimensions like h_p, l_p, g_p on the overall performance of the proposed antenna.

2.2.2.1   Effects of air gap between patch and ground h_p

To find the optimal air gap between the patch and ground, the position of h_p is very essential for obtaining the required results. To find the optimized value, h_p is varied from 2.43 mm to 4.43 mm with a step size of 1 mm. It is observed from Figure 2.5 (a) that S-parameters are dependent upon h_p. It can be seen that when h_p increases, the bandwidth of the proposed antenna also increases. Finally, we choose the optimized value of h_p as 3.43 mm which provides the increased bandwidth of $4.9-6.5\,\text{GHz}$ with $|S_{11}| \leq 10\,\text{dB}$ for the design.
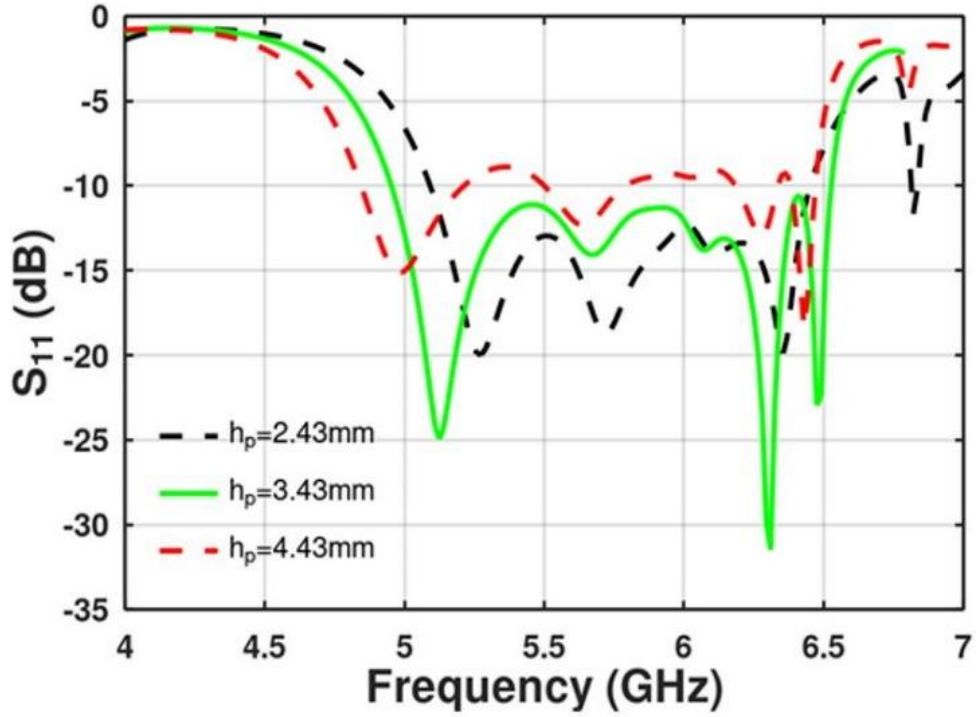
(a)

2.2.2.2   Effects of PIFA length l_p

Next, parametric analysis is performed on the length of the PIFA which is denoted by l_p. The effects of l_p on return loss and frequency band of the proposed antenna are shown in Figure 2.5 (b). The value of l_p is increased from $13.5\,\text{mm}$ to $15.5\,\text{mm}$ and the optimized value of l_p is found to be $14.55\,\text{mm}$ which gives the desired bandwidth.
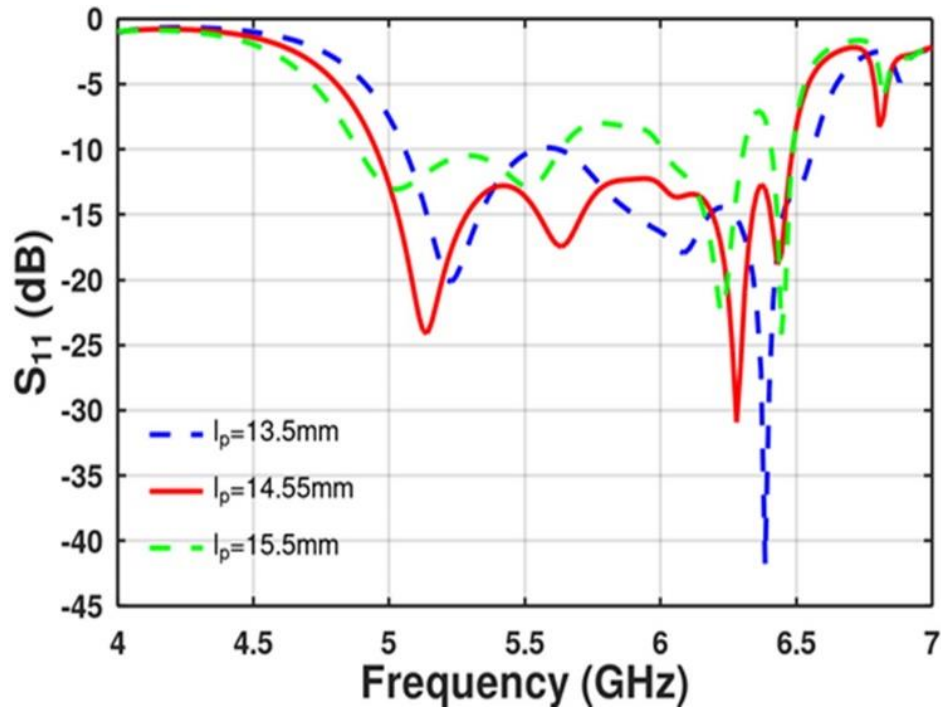
(b)

2.2.2.3 Effects of Feed Location from Shorting End

The location of feed from the shorting end should be carefully selected. This location should be selected in such a way that the feed sees $50\,\Omega$ impedance from the antenna. The distance

'g_p' between feed and shorting pin controls the characteristic impedance and bandwidth of the antenna. From Figure 2.5 (c), we can see that if the location of the feed is moved (change in g_p shows the movement of feed location) from the optimized location, the S-parameters degrade and also affect the impedance bandwidth. The figure shows the effect when 'g_p' is varied from $6.74\,\text{mm}$ to $8.74\,\text{mm}$ with a step size of $1\,\text{mm}$. We find that $g_p = 7.74\,\text{mm}$ is the optimized distance from the shorting end to feed the antenna that helps to achieve the desired frequency band.
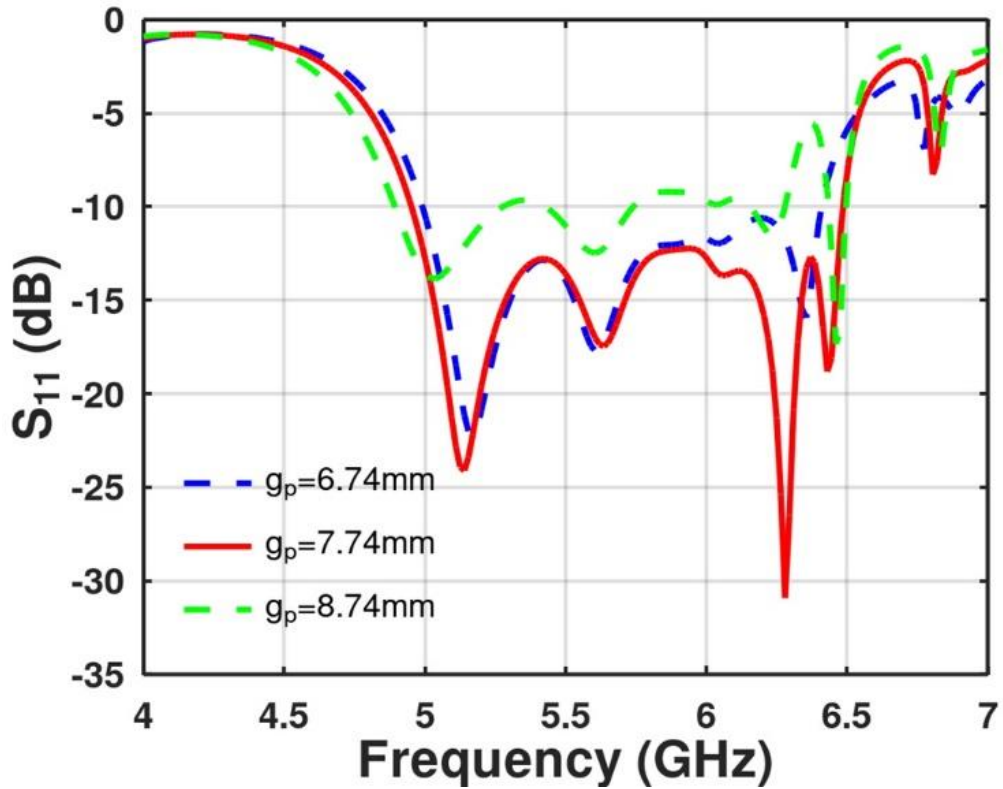
(c)

Figure 2.5: Simulated S-parameters of the proposed antenna as a function of (a) h_p, (b) l_p ,and (c) g_p.

2.3   Simulated and Measured Results

The prototype of the proposed antenna is fabricated and tested for the validation of antenna design. Figure 2.6 shows the S-parameters of the proposed antenna. The figure shows that there is a good agreement between measured and simulated results. The S-parameters of the PIFA antenna without AMC have lower bandwidth as compared to the antenna with AMC signifying that the introduction of the AMC has increased the bandwidth of the antenna. The measured impedance bandwidth is $4.8 - 6.7$ GHz i.e., 33% for $|S_{11}| \leq 10$ dB. It is important to note here that the introduction of the AMC brings in extra resonances which ultimately gives a better impedance match at different frequencies. These extra resonance modes show up as multiple dips in the desired frequency band.
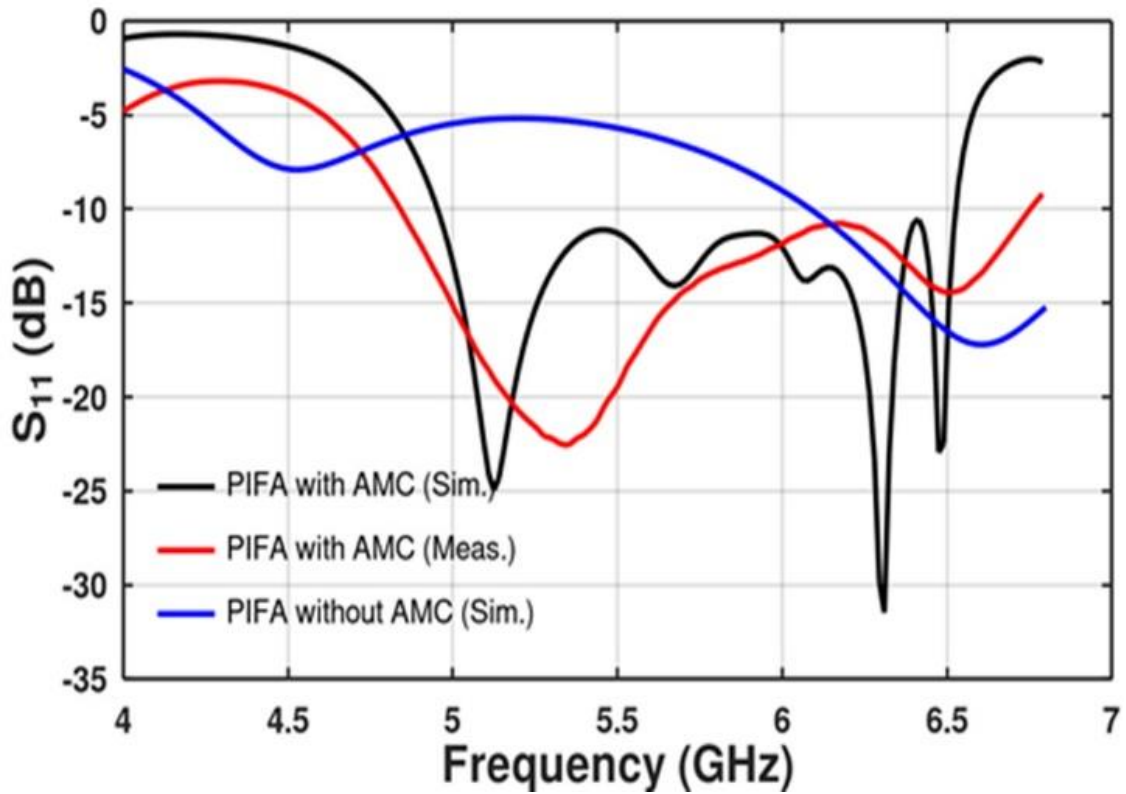
Figure 2. 6: Simulated and measured S-parameters of the proposed antenna.

AMC reflects the radiations of the radiating antenna in such a way so that the reflected field adds constructively with direct radiations of the antenna to provide unidirectional radiations. It is also important to note that the AMC has limited bandwidth (*i.e.,* frequency range from 5 GHz to 6.5 GHz of the reflected phase). Due to this limited bandwidth, AMC will not be able to reflect the beam away from it in the same phase as frequency changes. Moreover, the radiation pattern also does not remain unidirectional and becomes frequency-dependent. It also leads to lower gain for the frequencies that are away from the central frequency of AMC operational bandwidth. We find that the radiation pattern broadens and reduces the overall gain at 5 or 6 GHz as compared to 5.5 GHz as AMC gives better in-phase reflections at 5.5 GHz.

The simulated and measured radiation patterns of the proposed AMC-based PIFA antenna at 5, 5.5, and 6 GHz for different phi cuts are shown in Figure 2.7.
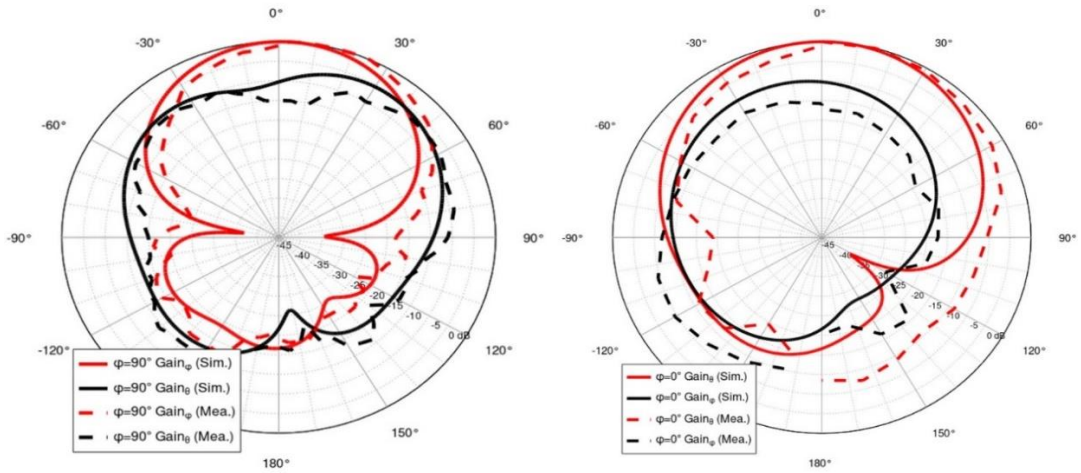
(a)
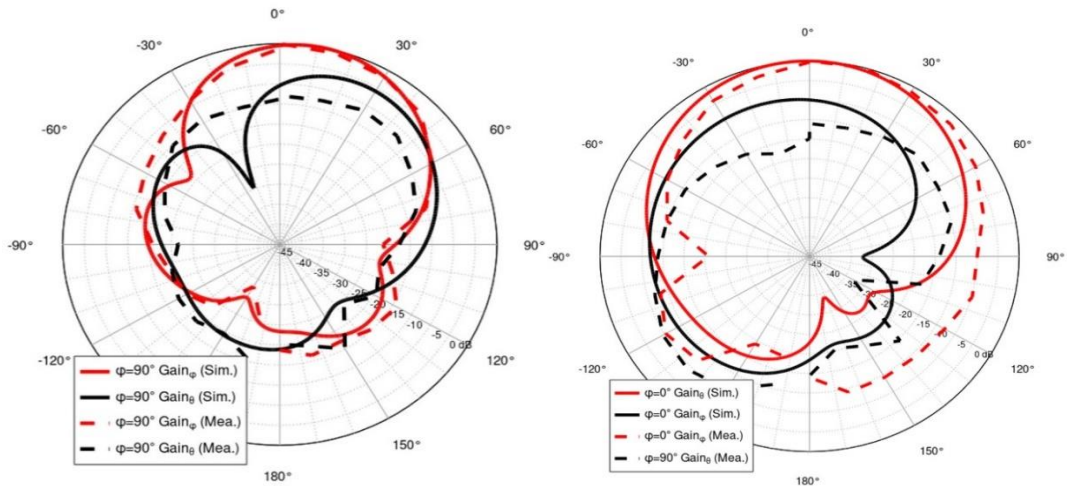
(b)
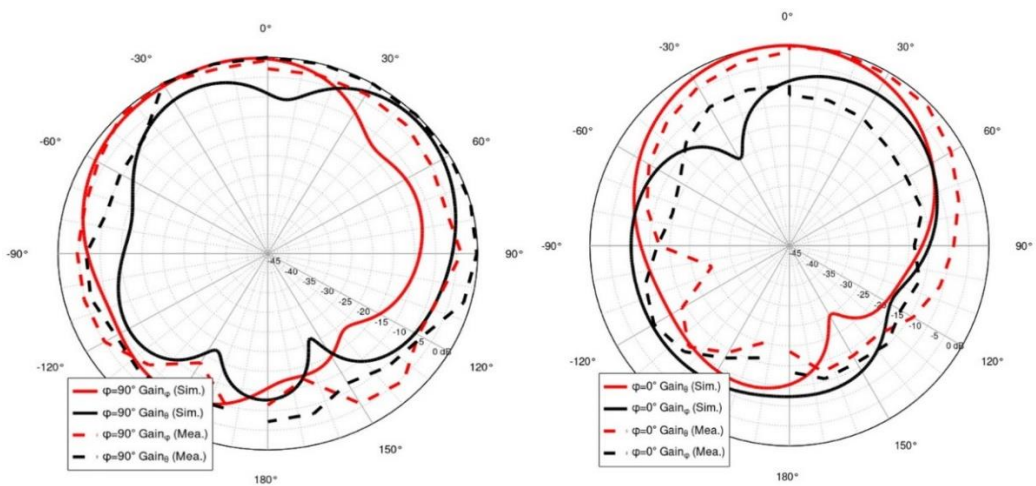
(c)

Figure 2.7: Simulated and measured radiation patterns (for $\varphi = 0^o$, $\varphi = 90^o$ cuts) of the proposed antenna at: (a) 5 GHz; (b) 5.5 GHz; (c) 6 GHz.

The simulated and measured results are in good agreement. The co-polarization gain is shown by red colour while the cross-polarization gain is shown by a black color lines. We note that the cross-polarization levels are high and are not desirable as it is the indication that the part of the power is getting wasted in unwanted polarization *i.e.,* cross-polarization. It is important to note here that the beam is getting tilted (*i.e.,* maximum gain is not along $\theta = 0^o$) because the material under the antenna is not uniform. On one side, there is ground and on the other side, there is no ground. This type of non-uniformity creates the tilt in the beam.

In order to reduce the cross-polarization level, without changing the radiation antenna structure, [52] can be helpful for the readers where rectangular metasurface superstate is employed to reduce cross-polarization. Another novel and innovative way of reducing cross-polarization is by enhancing the AMC design and this technique is shown in Figure 2.8.
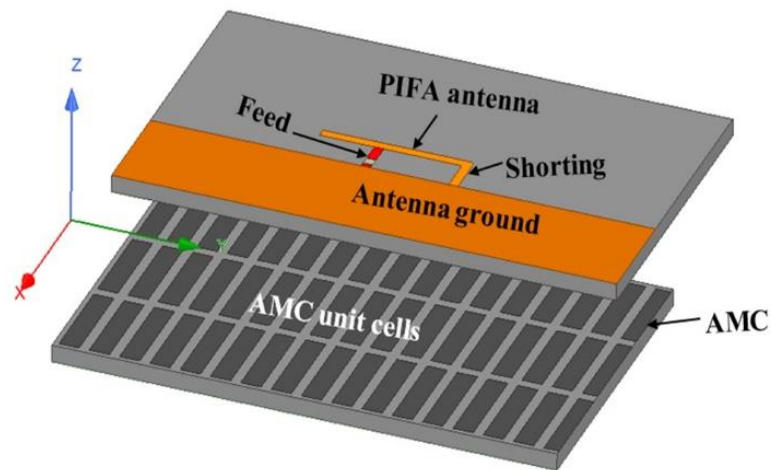
Figure 2.8: PIFA with rectangular AMC.

The improved AMC design with low cross-polarization is shown in Figure 2.8. The new AMC design composes rectangular unit cells instead of square unit cells. By this modification, AMC has a nonuniform effect on orthogonally polarizations and hence reflects orthogonal polarized fields whose characteristics are not the same. In this way, co- and cross-polarized radiations from the proposed antenna can be independently controlled by optimizing the AMC unit cell dimensions.

The optimized dimensions for rectangular AMC unit cells with low cross-polarization are found to be $p_x = 3 \, \text{mm}$, $a_x = 9.88 \, \text{mm}$, and $a_y = 2$.

Figure 2.9 shows the simulated radiation patterns of the PIFA antenna with rectangular AMC unit cells. Continuous lines show co-polarized field values while dashed lines show cross-polarized components. From radiation patterns, it can noted that the cross-polarization for PIFA antenna with rectangular AMC is far lower than the square AMC. This non-intrusive method of reducing cross-polarization is independent of the radiating element and can be applied to other different types of antennas. In this way, cross-polarization of the planar PIFA antenna can be reduced by using rectangular unit cells instead of square ones.

(a) (b)

(c)
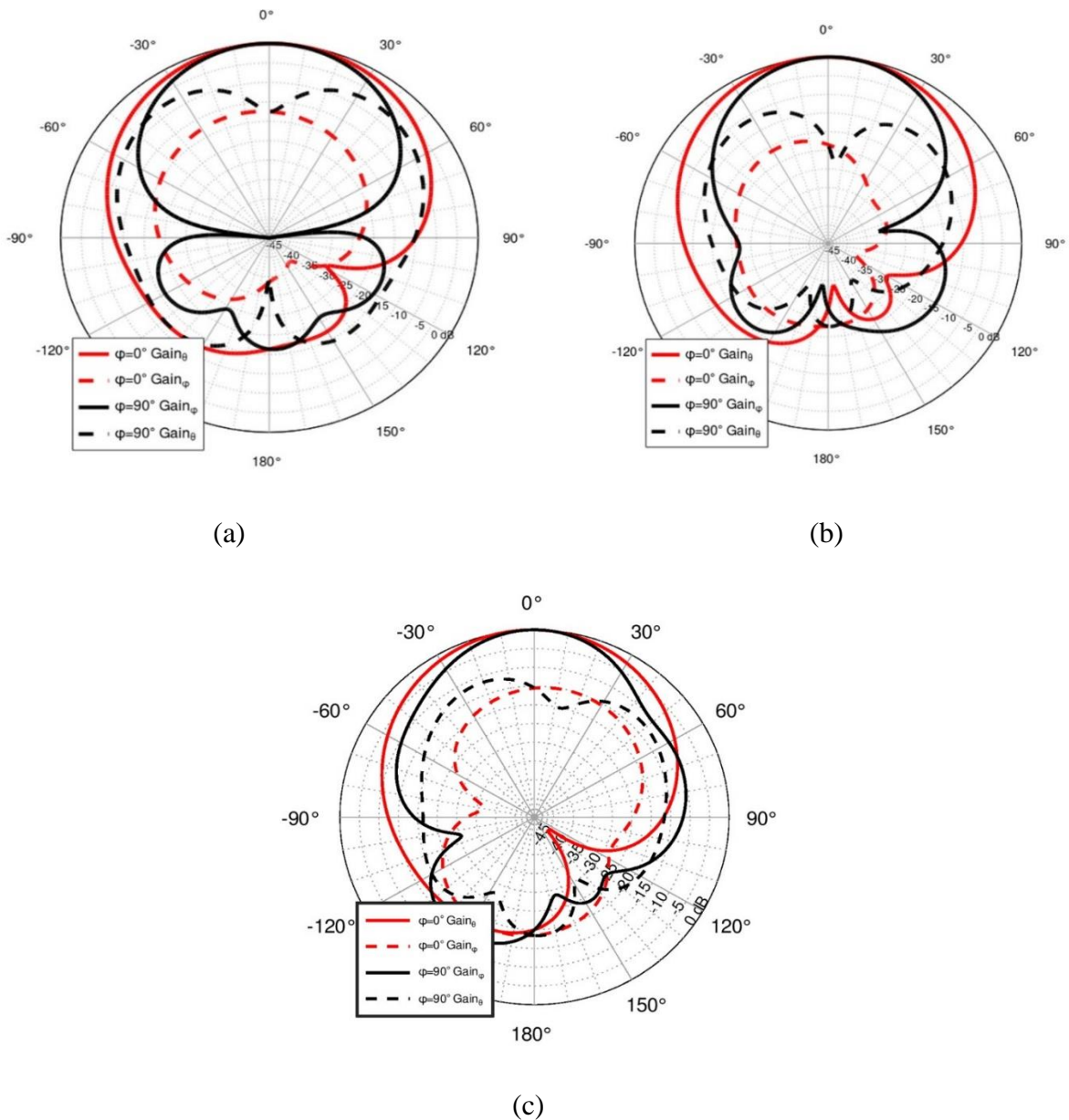
Figure 2.9: Radiation patterns of the PIFA antenna with rectangular AMC at: (a) 5 GHz; (b) 5.5 GHz; (c) 6 GHz.

36

The gain of the proposed PIFA antenna with and without AMC is shown in Figure 2.10. The maximum simulated gain of the proposed PIFA antenna with AMC is 8.3 dBi while the maximum measured gain is 7.6 dBi as shown in Figure 2.10. However, the gain of the PIFA antenna without AMC is quite low. It does show that the introduction of AMC has increased the gain of the PIFA antenna. This gain is measured in the direction perpendicular to the surface of the antenna (i.e., at $\theta = 0^o, \varphi = 0^o$ according to Figure 2.4). There is a good agreement between the simulated and measured value of the gain.
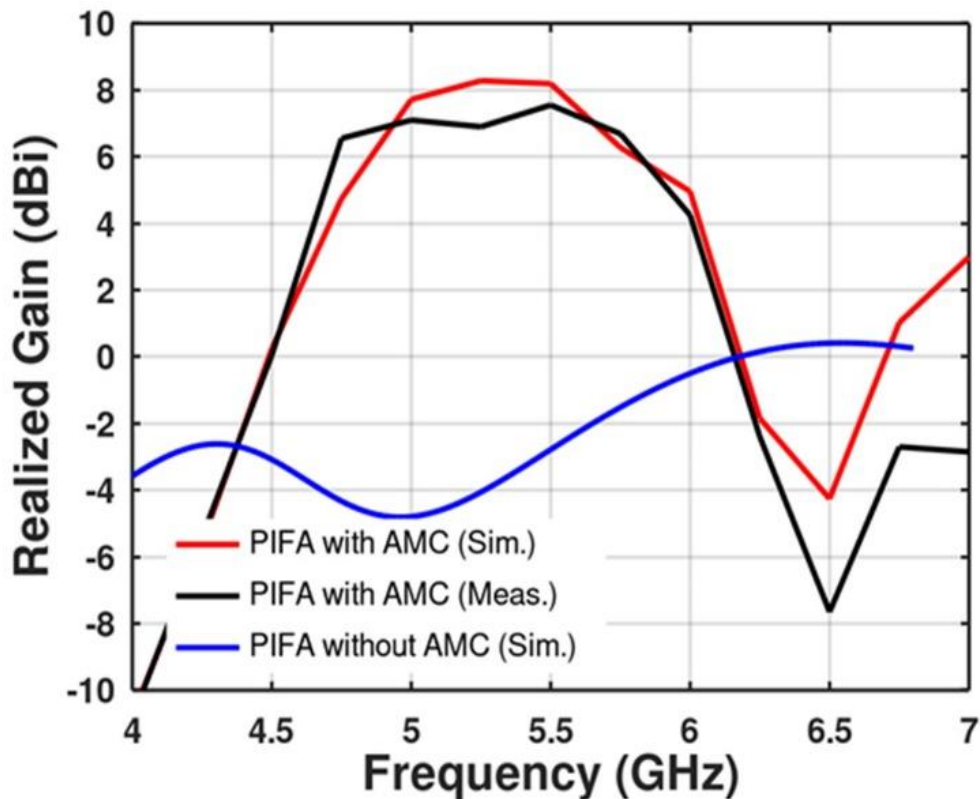
Figure 2.10: Simulated and measured realized gain of the proposed antenna.

The analysis of SAR for any antenna used in wireless applications is very important. SAR is used to measure the impact of electromagnetic waves on the human body in terms of power absorption by human body tissues. In this work, frequency-dependent three-layer and four-layer phantom models are designed for SAR analysis as shown in Figure 2.11. The three-layer phantom model consists of dry skin, fat, and muscles while the four-layer phantom model consists of skin, fat, muscles, and bones. The value of conductivity, permittivity, loss tangent for skin, fat, muscles, and bones have been calculated at three frequencies *i.e.,* at 5, 5.5, and 6 GHz and are given in Table 2.1 [54].

37
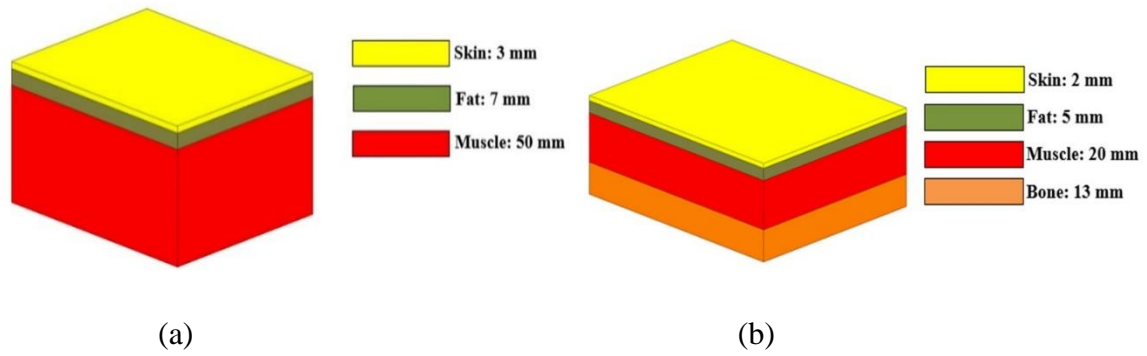
Figure 2.11: Human tissue models with layer thicknesses; (a) three-layer model; (b) four-layer model

TABLE 2.1: Dielectric properties of the tissues for different frequencies [54].

Tissue (layers)	σ	ε_r	δ
5 GHz			
Skin	3.06	35.78	0.3
Fat	0.24	5.03	0.17
Muscle	4.04	49.54	0.29
Bone	0.96	10.04	0.34
5.5 GHz			
Skin	3.46	35.36	0.32
Fat	0.27	4.98	0.18
Muscle	4.61	48.88	0.31
Bone	1.08	9.81	0.36
6 GHz			
Skin	3.89	34.95	0.33
Fat	0.30	4.94	0.18
Muscle	5.20	48.21	0.32
Bone	1.20	9.59	0.37

The SAR values have been carried out at 5, 5.5, and 6 GHz over 1 g average according to IEEE standards as shown in Tables 2.2 and 2.3.

TABLE 2.2: SAR level of the proposed antenna at 5, 5.5, and 6 GHz (100 mW).

SAR (W/Kg)	5 GHz	5.5 GHz	6 GHz
Three-layer model	0.4	0.22	0.54
Four-layer model	0.51	0.2	0.4

TABLE 2.3: SAR level of the proposed antenna at 5, 5.5, and 6 GHz (290 mW).

SAR (W/Kg)	5 GHz	5.5 GHz	6 GHz
Three-layer model	1.35	0.62	1.59
Four-layer model	1.5	0.6	1.2

The distance of the human model from the antenna is kept at 5 mm. The maximum limit of SAR has been evaluated by different power levels. Tables 2.2 and 2.3 show the value of average SAR over 1 g average for three-layer and four-layer human models at 100 and 290 mW power respectively. The maximum SAR value at three frequencies for 100 mW power level is 0.51, 0.21, and 0.54 W/kg respectively. In comparison, the maximum SAR value at three frequencies for 290 mW power level is 1.35, 0.62 and 1.59 W/Kg respectively. It is observed from these tables that the SAR values at 5, 5.5, and 6 GHz are lower than the standard maximum value of 1.6 W/Kg with input power up to 290 mW. Figure 2.12 shows the simulated SAR distribution of the proposed antenna. The Figure 2.12 shows the SAR distribution on different locations of the antenna when it is placed on three- and four-layer models. The plots show that the maximum value of SAR (0.22 W/kg) occurs at the rightmost top corner of the antenna while it is lower at other locations of the antenna.

The SAR can be reduced by obstructing the propagation of radiations from the antenna towards the human body. In this way, if the interaction between antenna radiations and the human body can be lowered, the SAR value will get reduced. One of the simplest methods to obstruct radiation from the antenna to the body is to placing the PEC sheet as the

obstruction. However, placing the PEC sheet has the disadvantage as to form the constructive radiation after reflection from the PEC, the distance of PEC sheet and the radiating antenna should be $\lambda_0 / 2$. For most applications, keeping PEC sheet $\lambda_0 / 2$ away might not be possible due to antenna size constraints. Another way is the introduction of AMC. The benefit of the AMC is the unique property that it can be brought closer to the antenna while it provides a similar reflection as the PEC sheet. AMC obstructs the radiation going towards the body and hence the SAR value reduces [53].
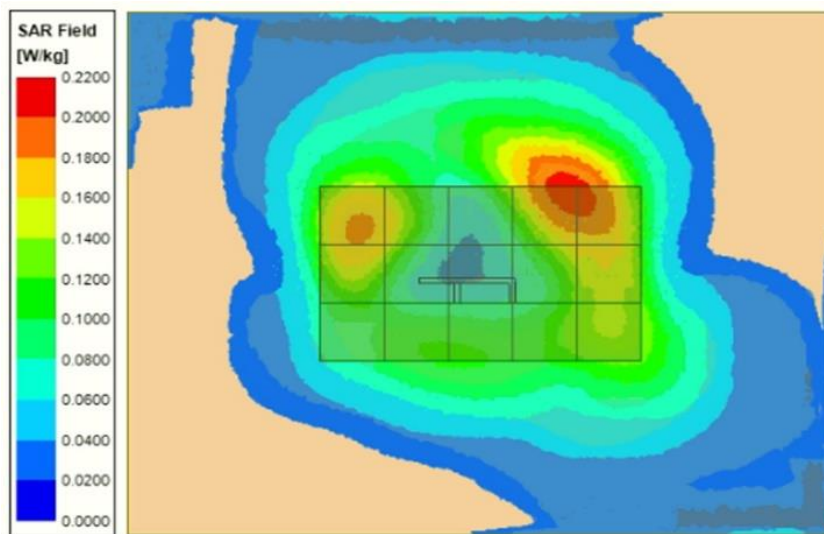
(a)
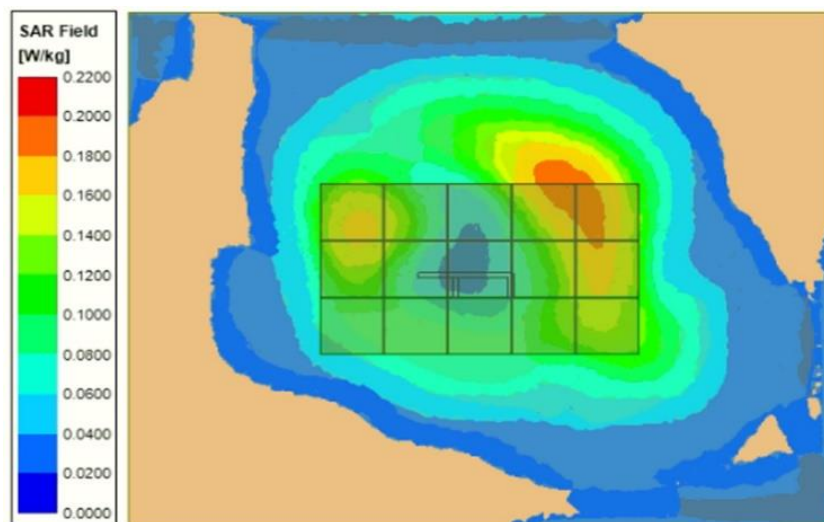
(b)

Figure 2.12: Simulated average SAR values; (a) three-layer model; (b) four-layer model at 5.5 GHz at the distance of 5 mm for 100 mW power.

Figure 2.13 shows the measured and simulated radiation efficiency of the proposed antenna. The plot shows that the antenna achieves a measured radiation efficiency of more than 85% for $5-6\,\mathrm{GHz}$ but 37% at $6.5\,\mathrm{GHz}$ signifying that it is working as a better radiator at lower frequencies than the higher ones. AMC structures are frequency-dependent structures so moving away from the central frequency will distort the desired behaviour of the AMC. In our case, the gain reduces at frequencies away from the central frequency (i.e., $5.6\,\mathrm{GHz}$) of AMC operation. The reduced gain at a higher frequency decreases the measured radiation efficiency. Another reason for decreased efficiency might be the lossy substrate material having a loss tangent higher than provided in the datasheet.
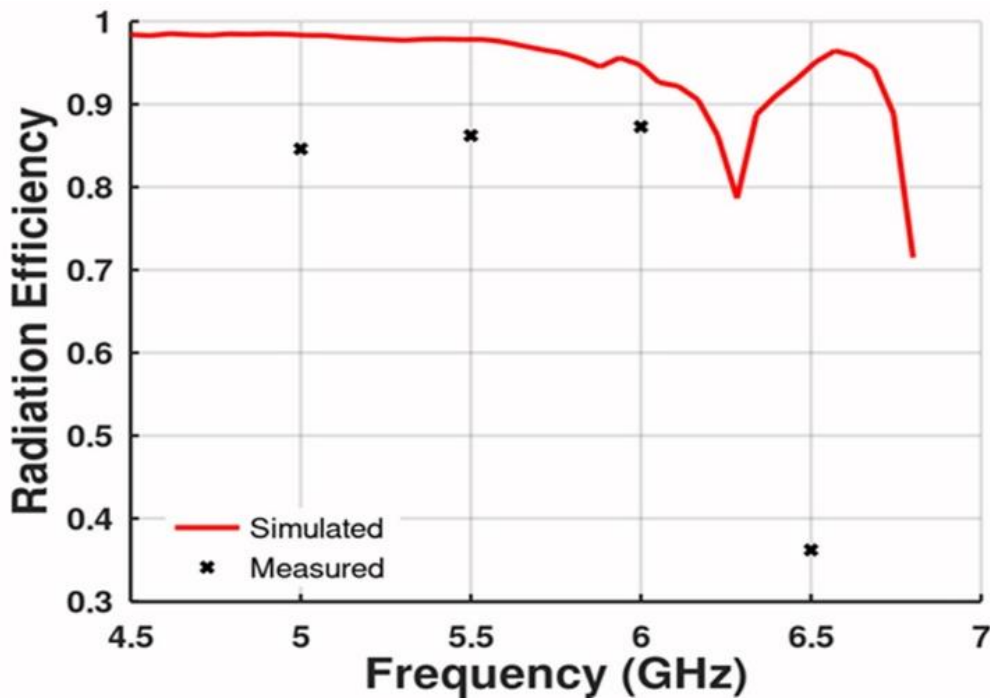
Figure 2.13: Radiation efficiency of the proposed antenna.

2.4 Observations and Comparisons of Proposed Antenna with Existing Designs

The antenna performance of the proposed designed antenna has been discussed in this section. Table 2.4 gives the comparison between related reference antennas published in the literature [28-32, 37-39, 43-46, and 48-51] and presented antenna results.

From the table, it can be seen that the proposed antenna is not only compact, wideband with low SAR but also gives the highest gain for a single antenna element among other existing designs in the literature.

Table 2.4 Comparison of the proposed antenna with other reported work based on AMCs.

Ref No.	Antenna	Dimension (λ_o)	Frequency Band (GHz unless specified)	Gain (dBi)	1-g Averaged SAR (W/Kg)
28	PIFA	0.5✕0.11✕0.096	2.4-2.49 4.19-6.1	2.5 3.2	-
29	PIFA	.096✕0.204✕0.012	1.8 2.4	-	1.8GHz, hand=3.73 2.4GHz, hand=55.3
30	PIFA	0.84✕ 0.66 ✕ .036	5.15–5.825	5.9	0.9307
31	PIFA	1.12✕1.12✕0.09	4.83-6.25	6	0.22
32	PIFA	1.06✕0.048✕0.044	470–771 MHz	3.5	-
37	PIFA with metasurface	0.77✕0.51✕0.07	4.96-5.90	6.7	0.3699 @ 5.5 GHz
39	PIFA With MDNC substrate	0.18✕0.37✕0.0094	911-981 MHz	-0.3	0.72
43	Dipole with AMC	0.576✕0.576✕0.088	4.90-5.5	6.2	-
44	Patch with AMC	1.74✕1.74✕0.126	2.37-2.59 4.28-5.62	6 4	-
45	PIFA	0.3✕0.12✕0.004	850-952.4 MHz 1750-1880 MHz	2.32 3.88	2.08 @ 900 MHz 2.29 @ 1800MHz
46	PIFA	0.32✕0.17✕0.004	900 MHz 1800 MHz	-	2

48	PIFA	0.12×0.06×0.0009	0.9	1.6	0.247
			1.8	3.95	0.899
49	AMC Textile antenna	1.70×1.13×0.06	4.30-5.90	6.12	0.37
50	Monopole with AMC	1.70×1.13×0.06	2.45	3.7	0.683
51	PIFA	-	4.6-7.55	1.3	-
This work	**PIFA with AMC**	**0.91×0.55×0.05**	**4.8-6.7**	**7.6**	**0.22 (three-layer)** **0.2 (four-layer)** **@ 5.5 GHz**

2.5   Conclusion

In this chapter, a compact PIFA antenna with high gain and low SAR has been designed and analyzed based on the AMC technique. The antenna performance enhancement in respect of gain, SAR, and bandwidth by using AMC is performed for planar PIFA antenna. By applying the AMC, the proposed antenna occupies a small area and provides wide bandwidth and high gain. The proposed antenna has an impedance bandwidth of 4.8–6.7 GHz (33% with center frequency at 5.75 GHz) with a maximum gain of 7.6 dBi. Furthermore, the undesired electromagnetic radiation towards the human body is analyzed by SAR using three-and four-layer of the human tissue model. The value of SAR of the proposed antenna is found to be lower than the IEEE standards which shows that the AMC is reducing the SAR values. The SAR values for the proposed antenna with three-layer and four-layer models are 0.22 and 0.2 W/kg in 1 g of tissue for 100 mW power, respectively. With such desired radiation properties, it is concluded that the proposed antenna is suitable for WLAN, C-band and especially for sub-6 5G applications if the proposed antenna is combined with similar antennas to form a MIMO configuration.

CHAPTER 3

Monopole Cavity Resonator Antenna using Artificial Magnetic Conductor and Superstrate

3.1   Introduction

In the last chapter, the concept of artificial magnetic conductor (AMC) on PIFA antenna was discussed for obtaining the high gain, wide bandwidth and low SAR. In the same chapter, the idea of the AMC along with different superstrates which can be used in place of each other without sacrificing antenna performance is also discussed for achieving high gain; therefore, it provides the flexibility to designers to achieved high gain.

Conventional planar monopole antennas have low gain and might not be usable for many applications due to it. While the use of AMC and superstrate is used for gain enhancements, it has never been employed for planar monopole antennas in a single design. So, this low gain problem was approached in a systematic manner. Hence, to achieve high gain, AMC as well as superstrate for enhancing the forward radiation from the antenna is used to remove all these shortcomings [75].

Literature survey reveals, based on the monopole antenna gain enhancement technique, there are several research attempts to enhance the gain in monopole antenna [71-79].
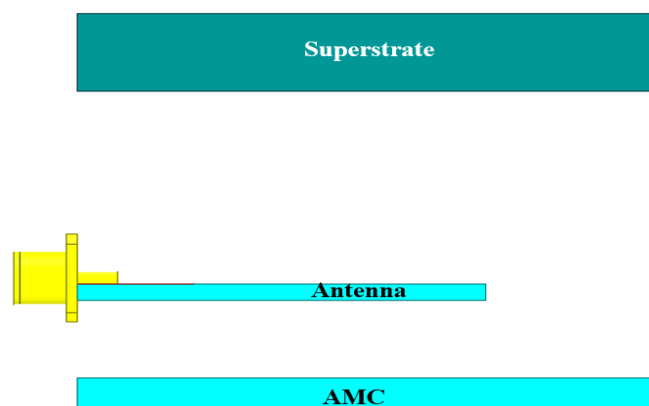
Figure 3.1: Typical antenna with AMC and superstrate.

A typical antenna with AMC and superstrate (see Figure 3.1) consists of AMC on one side of the antenna and superstrate on the other side of the antenna. In this way, radiations from the antenna are reflected from AMC and then are reradiated through superstrate by the Fabry-Perot effect [75], [76]. The combined effect of AMC and superstrate creates an antenna with a high gain if the design components are optimally designed.
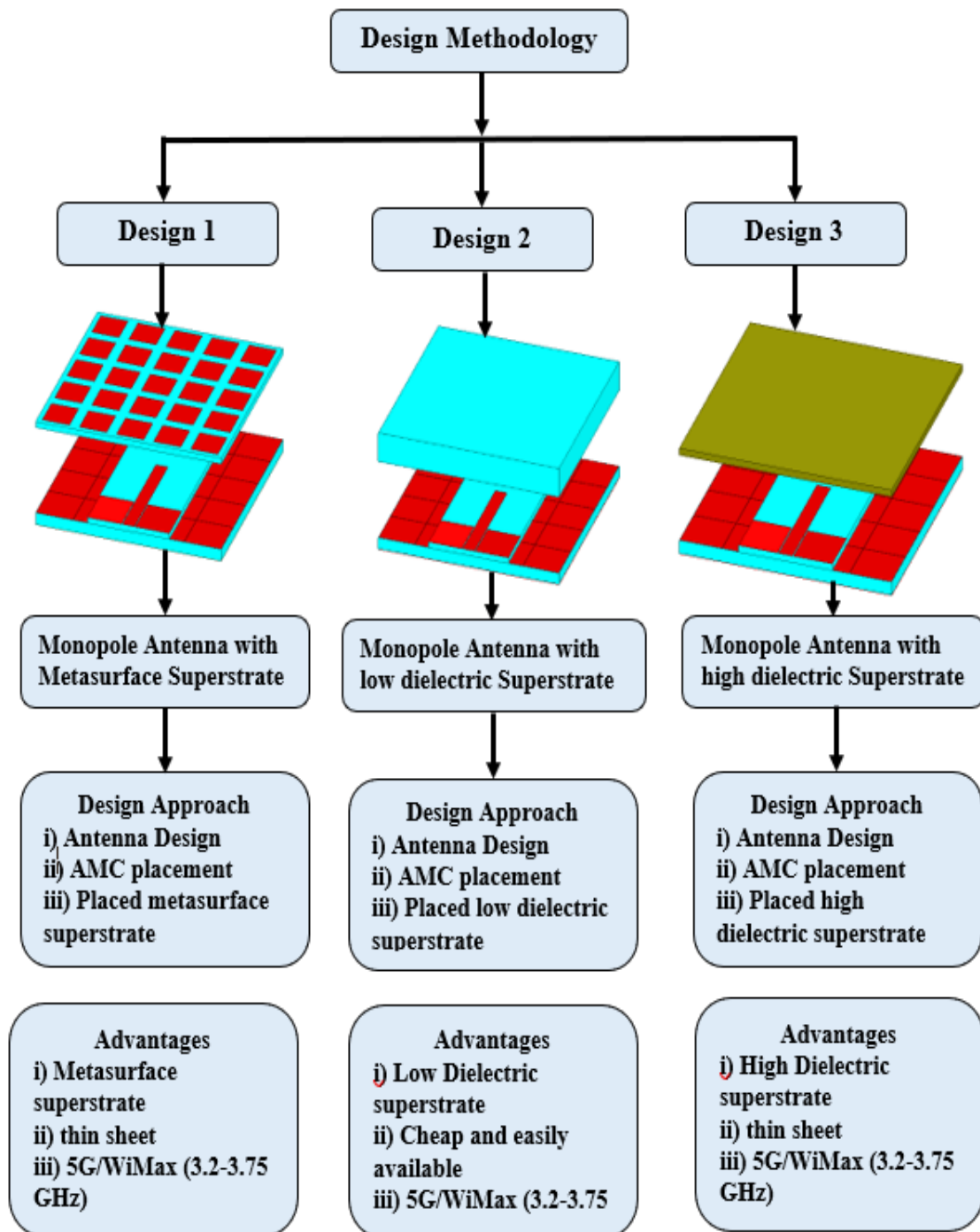
Figure 3.2: Design methodology of chapter-3 antenna.

This chapter us arranged into three sections: (i) designed and analysis of metasurface superstrate monopole antenna (Design-1), and (ii) low dielectric superstrate monopole antenna (Design-2), (iii) high permittivity dielectric superstrate monopole antenna (Design-3). Figure. 3.2 depicts the designed methodology of both the presented antennas in this chapter.

3.2   Design and Analysis of AMC based Monopole Antenna

As a radiating element, a CPW-fed monopole antenna is used as shown in Figure 3.3. The length of the monopole antenna is approximately $\lambda_g/4$ at a frequency of 3.5 GHz. The dimensions of the antenna are as: $h_m = 17$ mm, $w = 3.2$ mm, $c = 9.1$ mm, $n = 0.3$ mm, $l_3 = 10$ mm. For substrate, FR4 with a thickness of $t_2 = 1.6$ mm with permittivity of 4.4 and loss tangent of 0.02 is used.
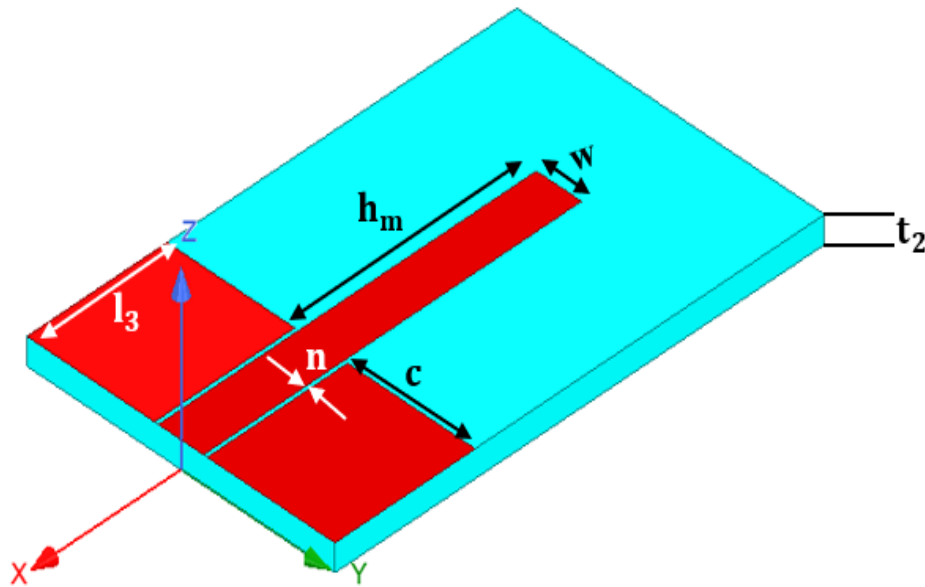
Figure 3.3. CPW-fed monopole antenna.

To start the AMC design, first, the AMC central frequency is decided. For the design, the AMC central frequency is 3.5 GHz. For AMC, a unit cell of 10 mm $\times$ 10 mm is used. Next, electrically-small square shaped pixel of side 'a' is printed at the center of the unit cell on the grounded FR4 substrate with a thickness of $t_1 = 3.2$ mm with permittivity of 4.4 and loss tangent of 0.02 as shown in Figure 3.4. The unit cell with periodic boundary condition (PBC)

is also shown. For simulation purposes, the Floquet port is applied for the calculation of the reflection phase and magnitude.

Next, the side of the square pixel $'a'$ is optimized so that periodic unit cell simulation gives a reflection phase of 0° at desired 3.5 GHz. In Figure 3.4 (c), we can see that when the side of the pixel, $a = 9.58$ mm, the reflection phase is 0°.
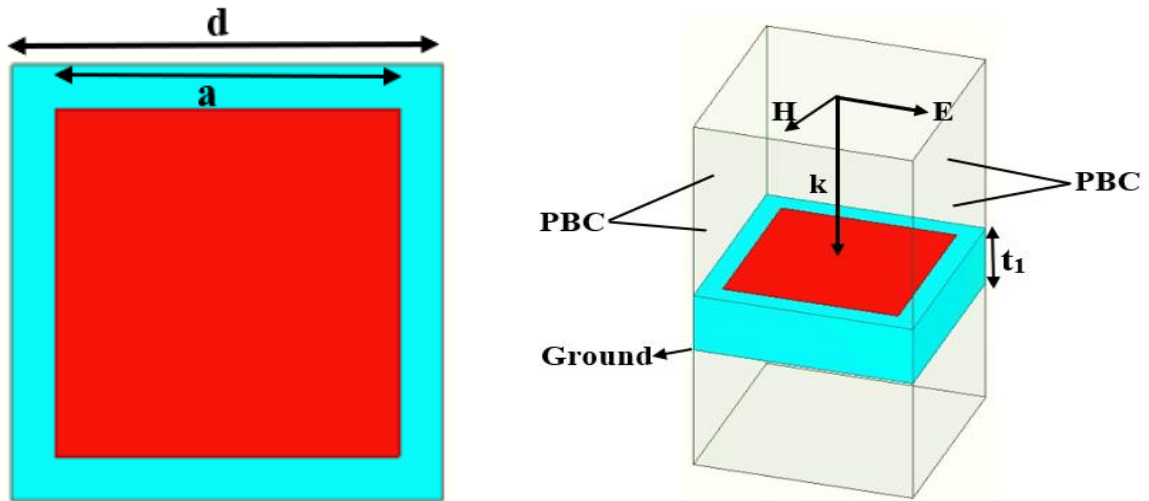
(a)   (b)
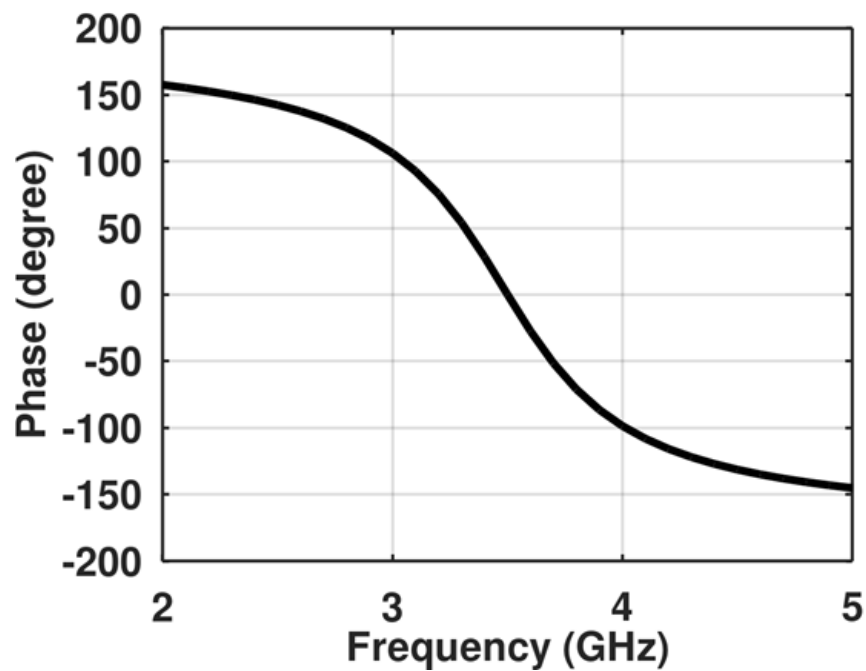
(c)

Figure 3.4: AMC unit cell: (a) top view; (b) isometric view; (c) reflection phase.

The geometry of the proposed low permittivity dielectric superstrate antenna is illustrated in Figure 3.5. In this structure, the monopole antenna is printed on FR4 substrate of dimensions l_2 (30 mm) $\times$ w_2 (22 mm) $\times$ t_2 (1.6 mm) with $\varepsilon_r = 4.4$ and loss tangent $= 0.02$. The antenna comprises the rectangular shape of dimension $h_m \times w$ fed by CPW whose dimension is given as c (9.1 mm) $\times$ l_3 (10 mm).

AMC as compared to PEC for reflection has the benefit that it can be placed near to a radiating antenna to enhance forward radiation. For our design, we place AMC touching the dielectric of the CPW-fed monopole antenna as shown in Figure 3.5. In the design, we use a grid of 5×5 AMC cells, designed earlier, to keep the overall antenna size small.

It is important to note here that mostly AMC is placed a little away from the radiating element for a better impedance match. But, putting AMC away from the antenna poses the threat of breakage of the whole antenna system if it is not handled well. Mostly foam is used to maintain the separation between AMC and radiating element and this separation distance has to be maintained well. In our design, we circumvent this problem by bringing AMC close so that there is no separation between AMC and radiating antenna, and in this way our design is more rigid and robust.

(a)

<div align="center">(b)</div> <div align="center">(c)</div>
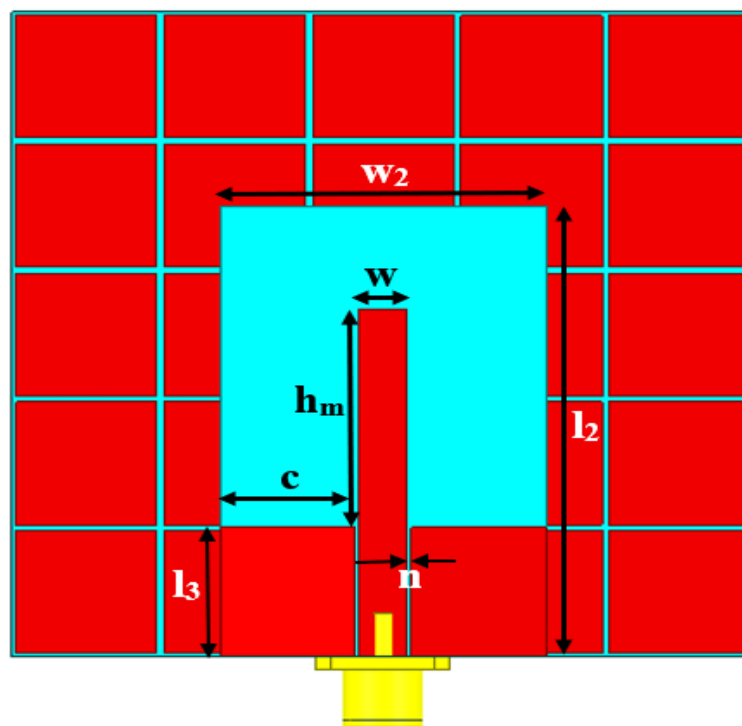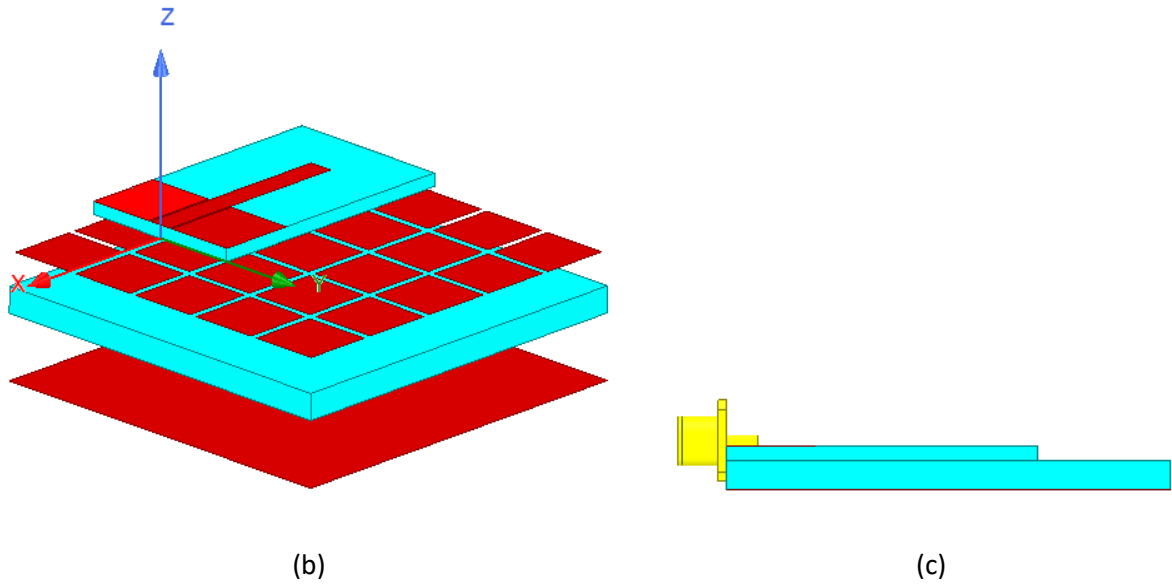
<div align="center">Figure 3.5: AMC with CPW-fed monopole antenna; (a) Dimensions; (b) exploded; (c) side view.</div>

Figures 3.6 and Figure 3.7 show the S-parameters and gain (at $\theta = 0^o, \varphi = 0^o$) for monopole antenna with and without AMC to see the effect of AMC. From these figures, we see that the application of AMC reduces the impedance bandwidth but increases the gain of the composite structure. Impedance bandwidth reduces due to the loading of the antenna by AMC. It is evident that the AMC increases the gain of the antenna by more than 5 dB.
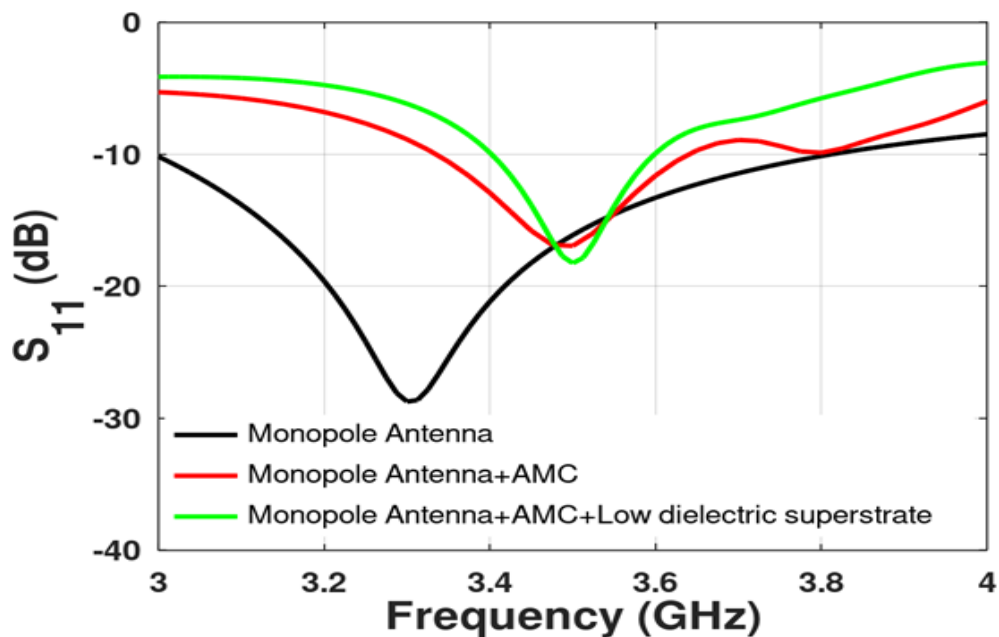
<div align="center">Figure 3.6: Simulated S-parameters of monopole antenna.</div>
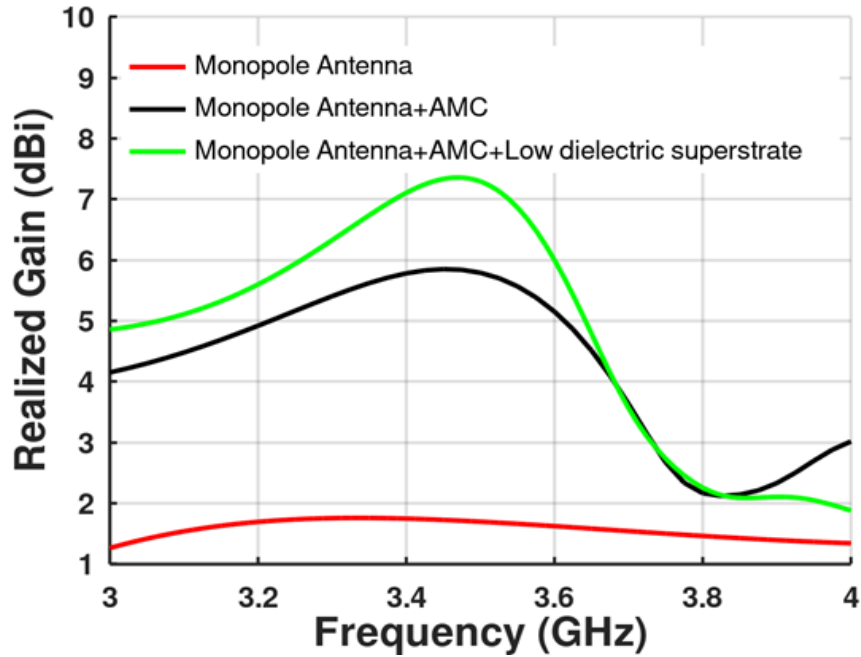
Figure 3.7: Simulated realized gain of the monopole antenna.

3.3 Design of Superstrate based Monopole Antenna

Once the AMC is designed, work on superstrate design is progressed. For typical superstrates, mostly metasurface substrates are used. In current work, it shows three designs of superstrates that can be used in place of each other and have similar properties. The reason to come up with three designs is to give flexibility to the designers so that they do not have to depend on one method for substrate design. It also gives the flexibility to choose the most economical superstrate. We will also see later that two of these substrates can also be directly 3D printed and do not need cumbersome PCB etching for its design in line with [77-79]. The superstrate helps to create a cavity effect in line with the Fabry-Perot effect [75-76] and its transmission and reflection behaviour decides the overall gain from the antenna. A Cavity is formed on one side by AMC and on the other side by superstrate. Three superstrates created and then compare their properties to see if they provide a similar response. Metasurface superstrate is also studied in a similar way as AMC but, instead of just reflection as is the case in AMC, its transmission behaviour is also studied when it is combined with an antenna [75-76].

3.3.1 Design and Analysis of Metasurface Superstrate Monopole Antenna

In this case, a metasurface superstrate with 1.6 mm thickness and permittivity of 4.4 is used. The metasurface superstrate comprises a 5×5 grid of metallic square patches with sides of

7.26 mm. The metasurface superstrate layer is placed above the antenna with an air gap of 21.4 mm i.e., at $\lambda/4$ as shown in Figure 3.8 (a).
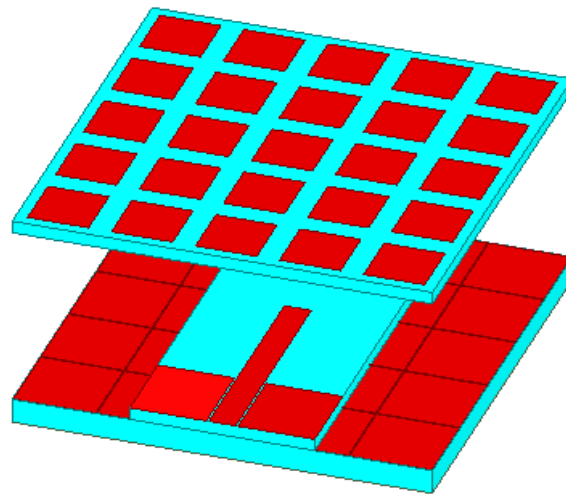
(a)

3.3.2 Design and Analysis of High Dielectric Superstrate Monopole Antenna

This superstrate needs a high dielectric material of permittivity of 16.1. The high dielectric superstrate with 1.6 mm thickness is placed above the antenna with an air gap of 21.4 mm i.e., $\lambda/4$. This superstrate needs high dielectric material to enhance the gain of the antenna as shown in Figure 3.8 (b).
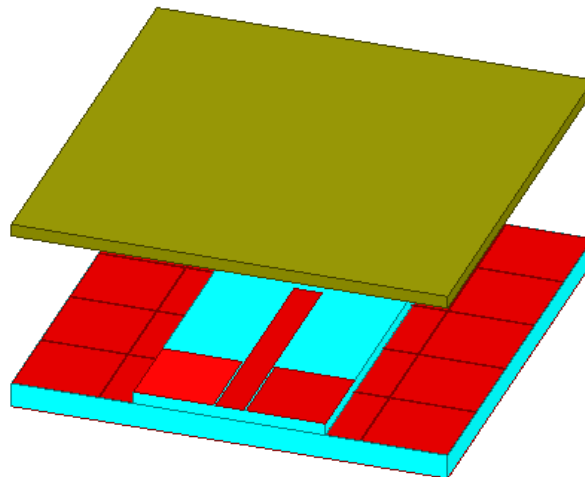
(b)

3.3.3 Design and Analysis of Low Dielectric Superstrate Monopole Antenna

In this case, a low dielectric superstrate with 8 mm thickness and permittivity of 4.4 is placed above the antenna with an air gap of $g_p = 21.4$ mm i.e., $\lambda/4$ as shown in Figure 3.8 (c)
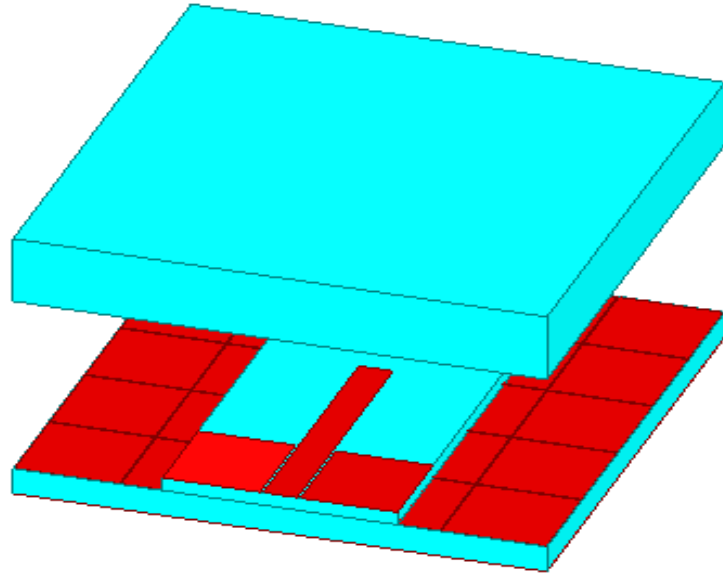
(c)
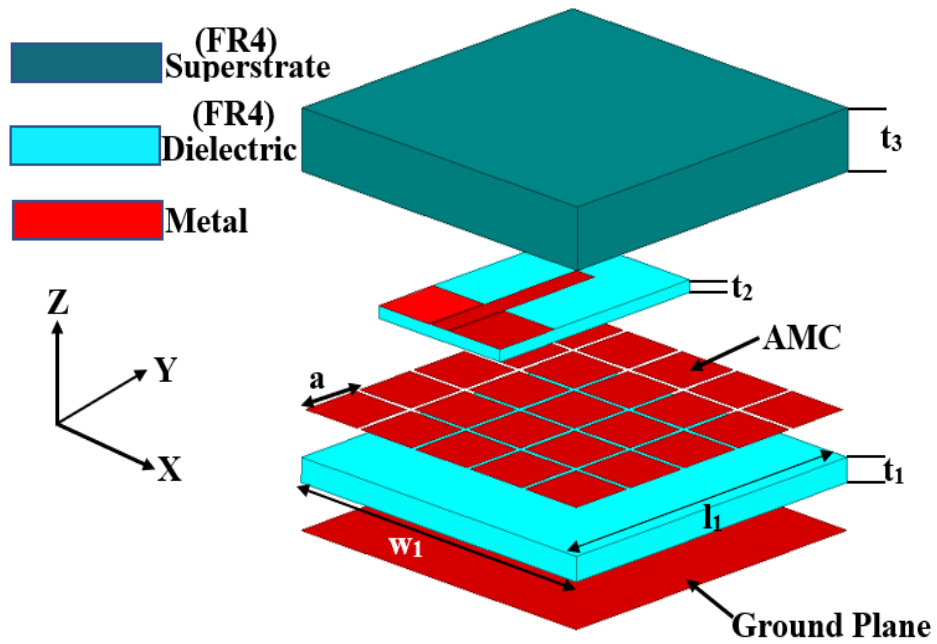
(d)
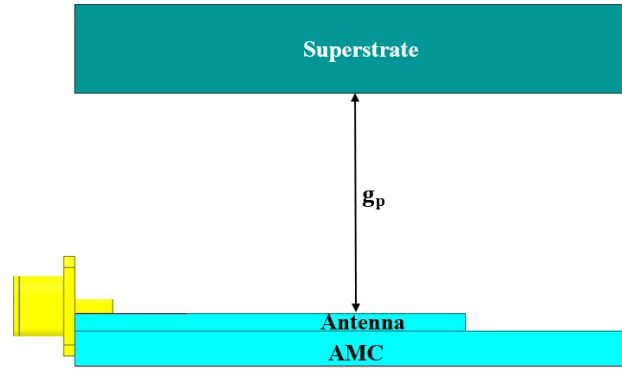
(e)

Figure 3.8: Antenna with different superstrates: (a) metasurface superstrate; (b) high dielectric superstrate; (c) low dielectric superstrate; (d) low dielectric superstrate layered structure; (e) low dielectric superstrate antenna side view.

All three superstrate designs have been simulated and analyzed by considering an equivalent dielectric method as described in [77-79]. Next, we place superstrates one-by-one on the antenna and then compare their characteristics. The comparison of S_{11} of the three superstrate antenna designs is shown in Figure 3.9. It is evident that the S_{11} of the three superstrate antennas are nearly similar and resonate at 3.5 GHz. It is observed from Figure 3.10 that the gains of the three superstrate antennas are nearly similar to each other.
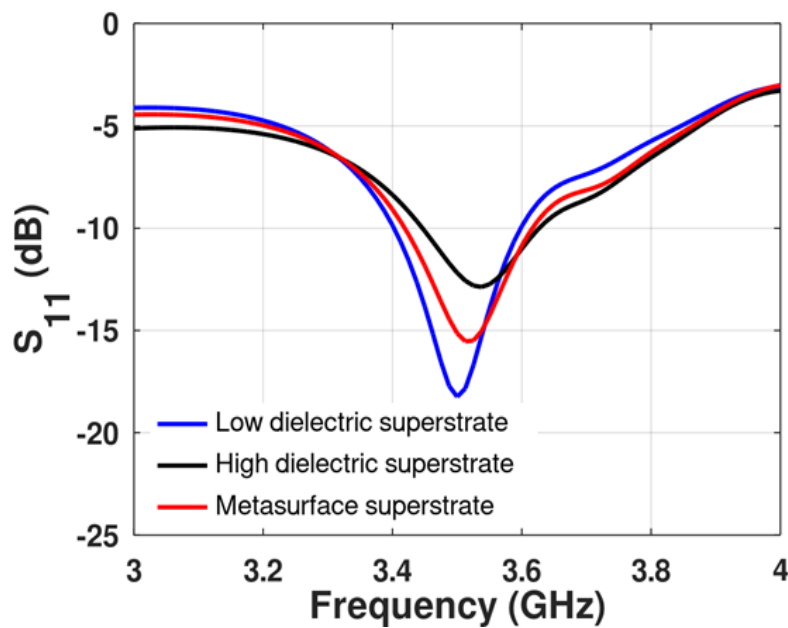
Figure 3.9: Comparison of simulated S_{11} of the three superstrate antennas.

53
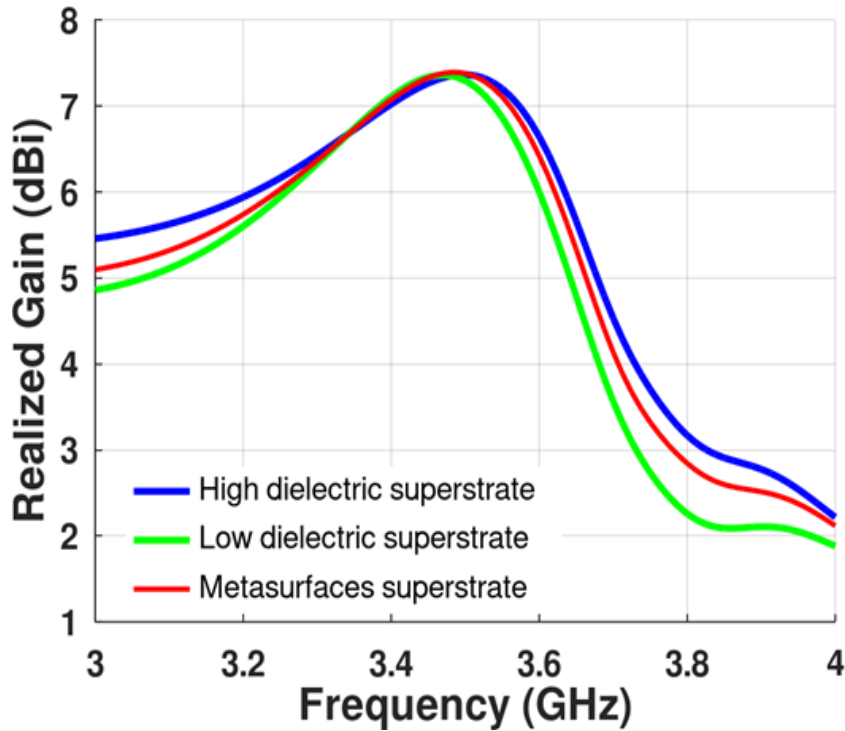
Figure 3.10: Comparison of simulated gain of the three superstrate antennas.

The three superstrate design simulations show that the gain of the proposed antenna can be increased by applying any of the superstrates. The high dielectric superstrate has a high value of permittivity i.e., 16.1 which is expensive and not easily available. Metasurface superstrate requires 5×5 metallic square patches to enhance the gain of the antenna. Low dielectric superstrate with 8 mm thickness has a permittivity of 4.4 which achieves the same gain as compared to high dielectric and metasurface superstrate antennas.

To get the insights into how all three superstrates have similar properties, the following alternate methods for analysis is shown [75-76].

3.4   Transmission/Reflection Analysis of Superstrates

We create periodic unit cells for all three superstrates and analyze these unit cells separately [78]. For this analysis, a unit cell of size 10 mm × 10 mm is used. Figure 3.11 shows the reflection and transmission behaviour of unit cells of three superstrates. By this comparison, we can see that all the superstrates show similar reflection and transmission characteristics. When a superstrate is used over the antenna, its transmission, as well as reflection behaviour, determines the cavity formation by the superstrate and ground near the radiating antenna. If

their reflection/transmission response is the same, they can be replaced with each other to get similar radiation characteristics from the antenna.

(a)   (b)

(c)   (d)
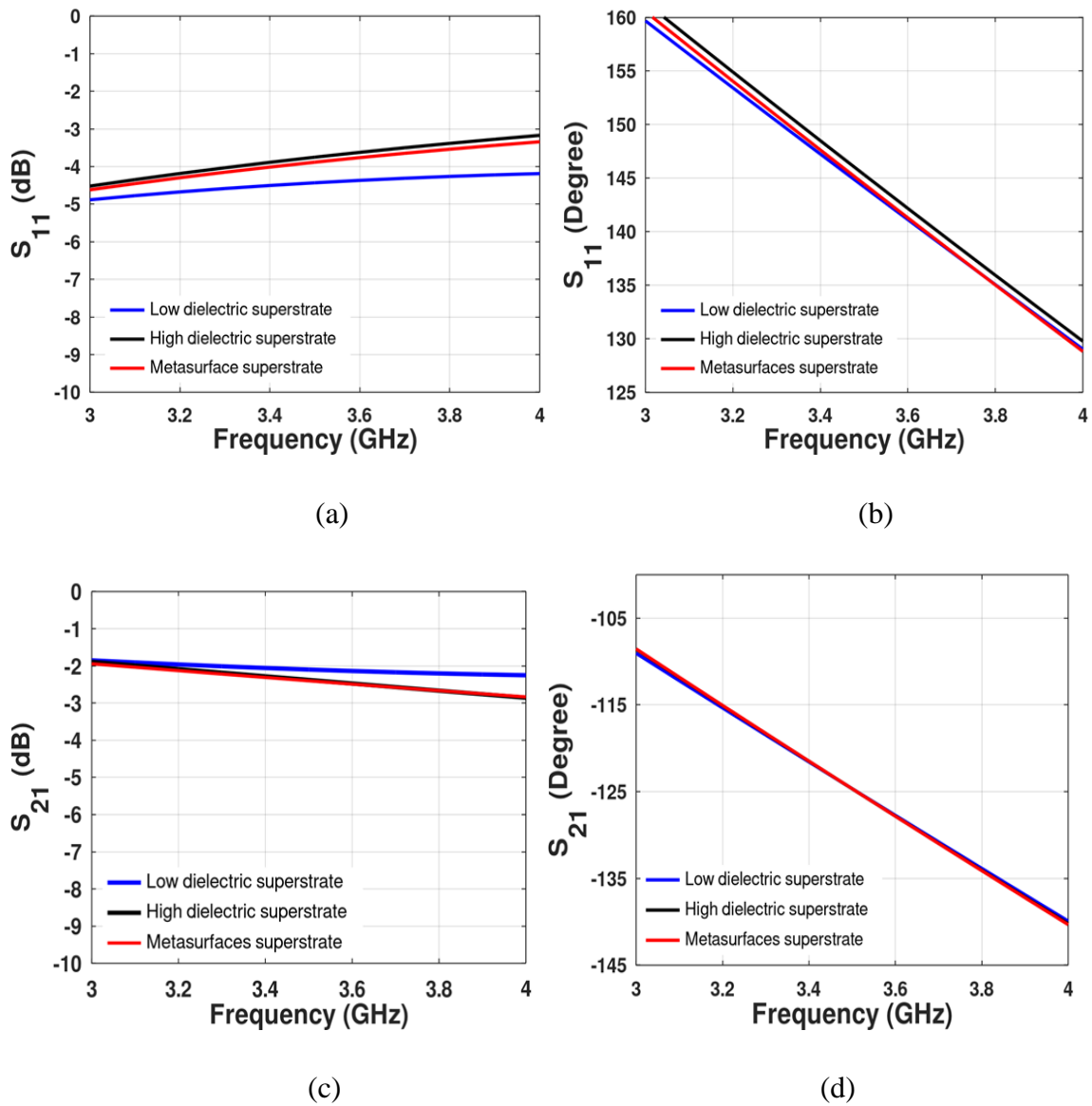
Figure 3.11: Simulated S-parameters and phase of the superstrate unit cell (a) S_{11} magnitude; (b) S_{11} phase; (c) S_{21} magnitude; (d) S_{21} phase.

3.5   Near Field Behaviour of Three Antenna Systems

To check the efficacy of the superstrate, we also analyze the near field behavior of three antenna systems previously shown in Figure 3.8. For this analysis, we take a horizontal line in the middle of the antenna and study the near field on this line as in [77]. For this analysis, the dominant electric field (here E_x in our case) is taken and analyzed on the surface of a line above the superstrate. The field measurement line is placed 1 mm above the superstrate to

calculate the E_x magnitude and phase. The superstrate should create uniform fields on top of the superstrate signifying that a near field with a uniform phase will create constructive radiation giving higher gain in presence of the superstrate. Dominant E_x field magnitude and phase values on the line are shown in Figure 3.12 (a) and Figure 3.12 (b). From the phase plot, we see that the phase is straightened in the case when a superstrate is present. It means that the near field will add constructively and that gives higher gain. Similar behaviour is observed when the measurement plane is used instead of a line for measuring the near fields as shown in Figure 3.12 (c-f). Straight horizontal phase lines in Figure 3.12 (b, d, f) show that the phase has been corrected by the introduction of superstrate and makes the radiating field converge and hence gives higher gain.

(a)

(b)

(c)

(d)

56

$$(e) \qquad\qquad\qquad\qquad (f)$$
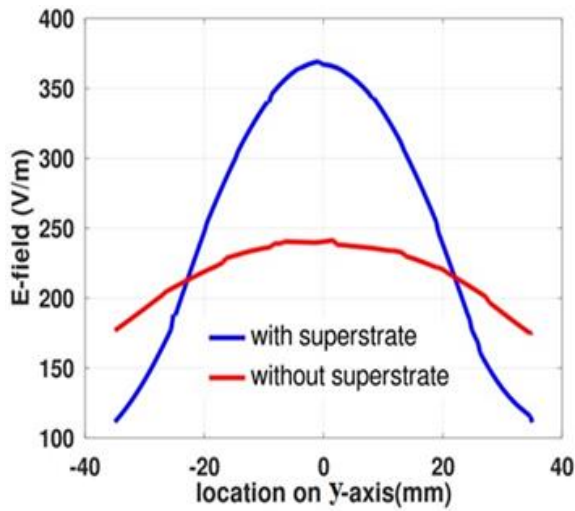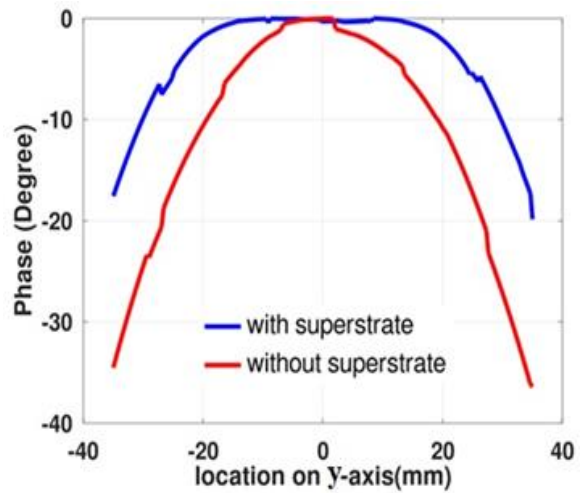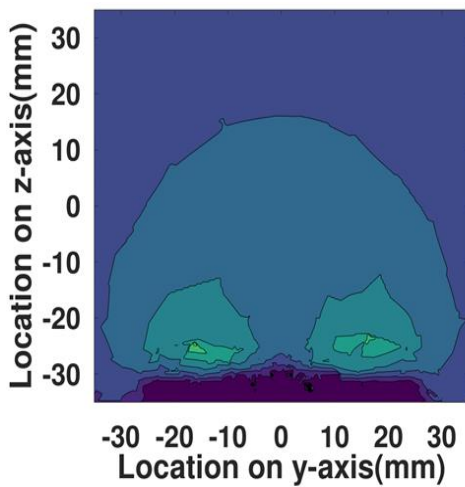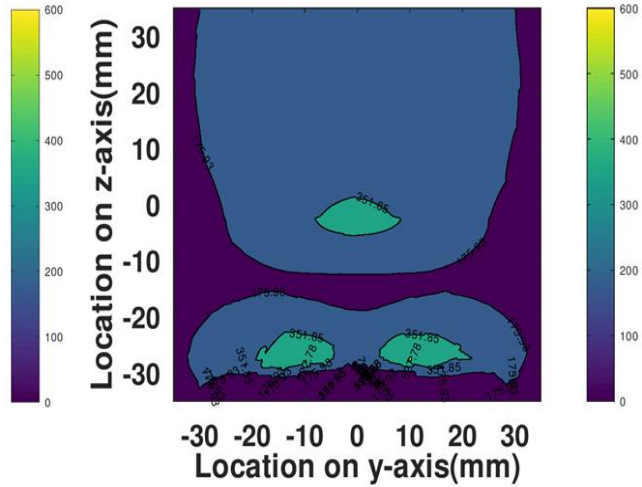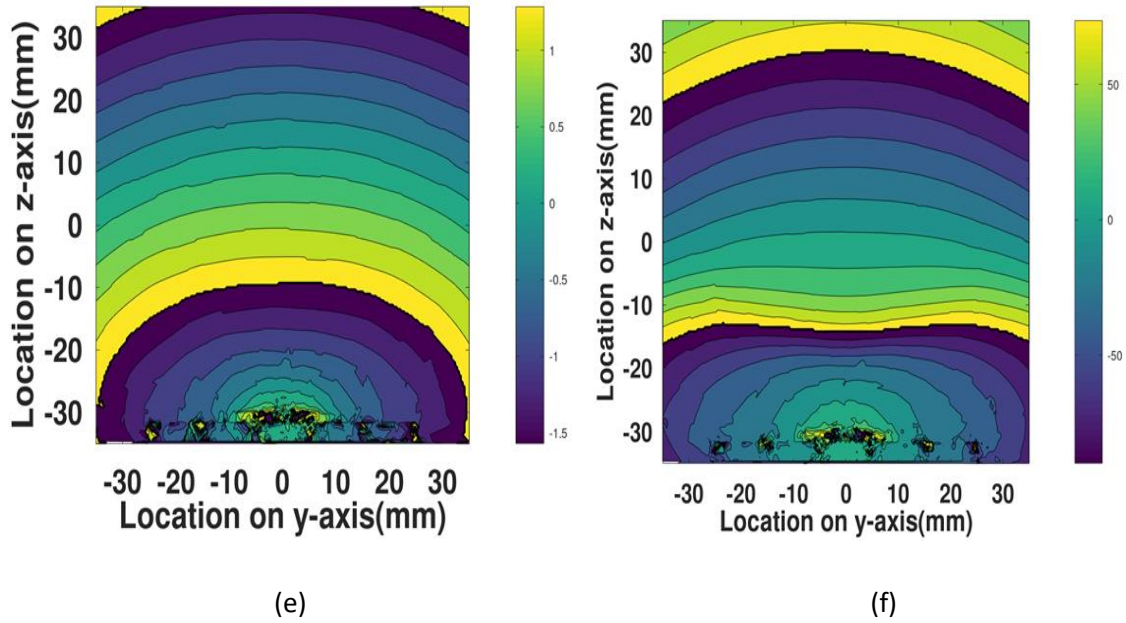
Figure 3.12: Near field performance of the proposed antenna: (a) E-field magnitude on a line; (b) E-field phase on a line; (c) E-field magnitude without superstrate on a plane; (d) E-field magnitude with superstrate on a plane; (e) E-field phase without superstrate on a plane; (f) E-field phase plot with superstrate on a plane.

3.6   Parametric Analysis

The parametric study is conducted to obtain the optimized dimensions of the antenna. The air gap between the antenna and superstrate, g_p, is analyzed against the performance of the proposed low dielectric superstrate antenna. The performance of the antenna against g_p is shown in Figure 3.13. It is depicted in Figure 3.13 that the S_{11} is sensitive to the variation of g_p.

For desired central frequency and bandwidth, the optimized value of g_p is chosen to be 21.4 mm.

Out of three superstrate antenna choices, we fabricate the thick dielectric superstrate to check how good simulated results match with measurements of the fabricated antenna.
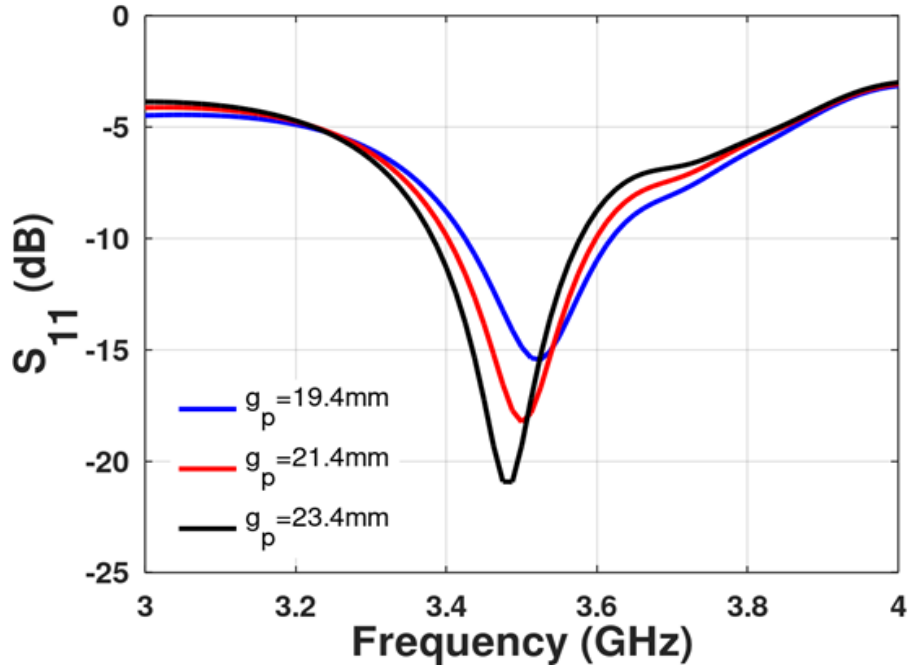
Fig. 3.13. Simulated S_{11} of the proposed antenna with different g_p.

3.7 Simulated and Measured Results

The different properties of the fabricated antenna shown in Fig. 3.14 are measured using the vector network analyzer and anechoic chamber.

The simulated and measured S_{11} of the proposed antenna is shown in Fig. 3.15. It can be seen that the simulated and measured impedance bandwidth of the proposed antenna is from 3.4-3.6 GHz and 3.2-3.75 GHz respectively. The simulated S_{11} of the proposed antenna has good agreement with the measured results. The fabricated antenna has wide impedance bandwidth for WiMAX and 5G applications.
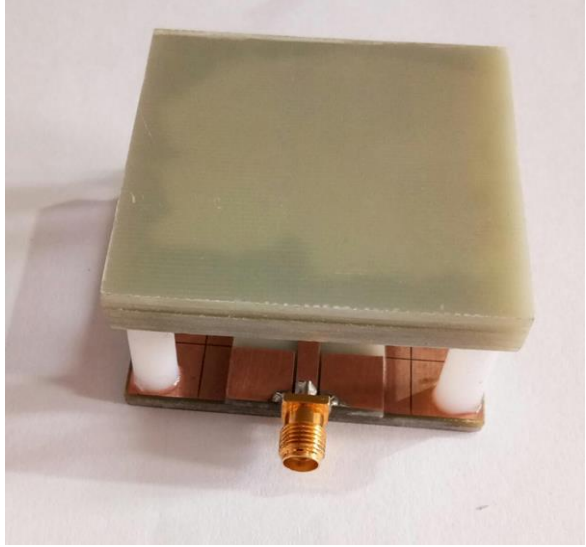
(a)

(b)

(c)

Figure 3.14: Fabricated proposed antenna: (a) top view; (b) bottom view; (c) antenna under measurements in an anechoic chamber.
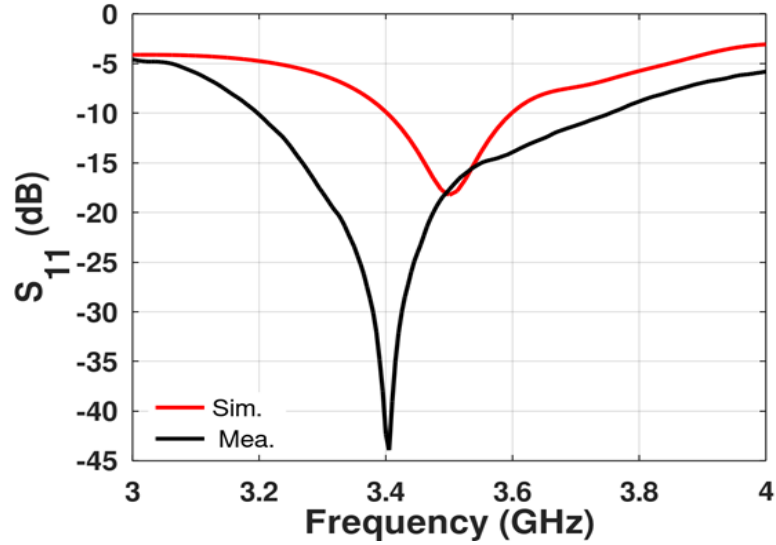
Figure 3.15: Simulated and measured S_{11} of the proposed antenna.

The radiation performance of the antenna is studied with simulated and measured radiation patterns at 3.5 GHz as shown in Figure 3.16. Red color lines are co-polarized and black color lines are for cross-polarized gain values. Continuous lines are for simulated values while the dotted lines are for measured values. It can be noted from the figures that the antenna has good cross polarization response.

(a)

(b)
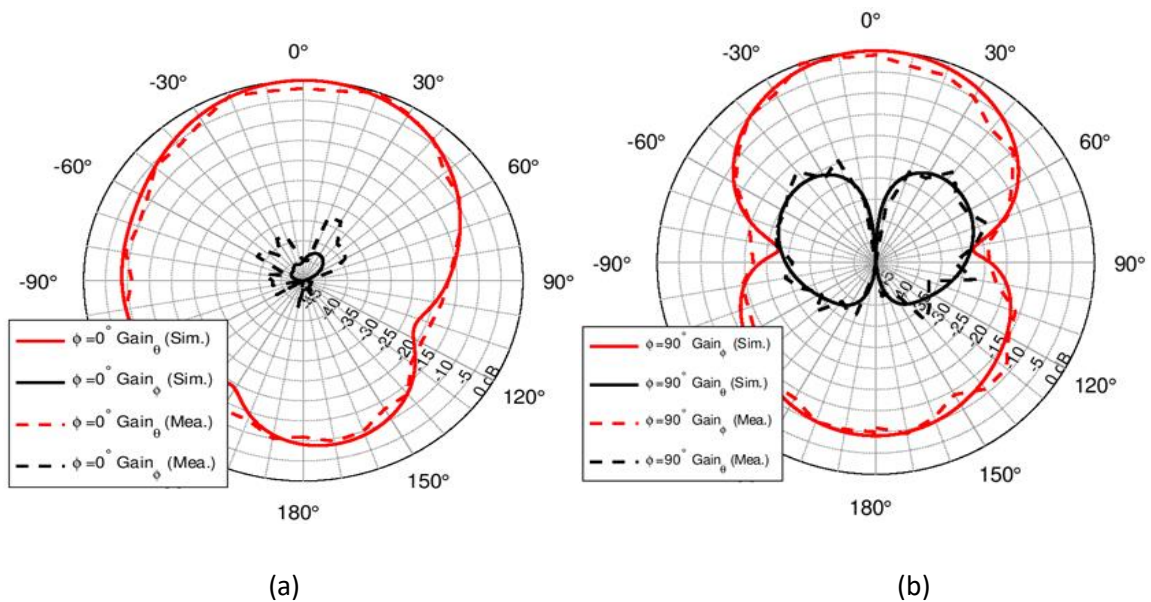
Figure 3.16. Simulated and measured radiation patterns at 3.5 GHz. (a) $\varphi = 0^o$ cut (b) $\varphi = 90^o$ cut.

Figure 3.17 shows that the simulated and measured gains are 7.3 dBi and 7 dBi at 3.5 GHz respectively. It is observed that simulated gain matches measured gain closely.
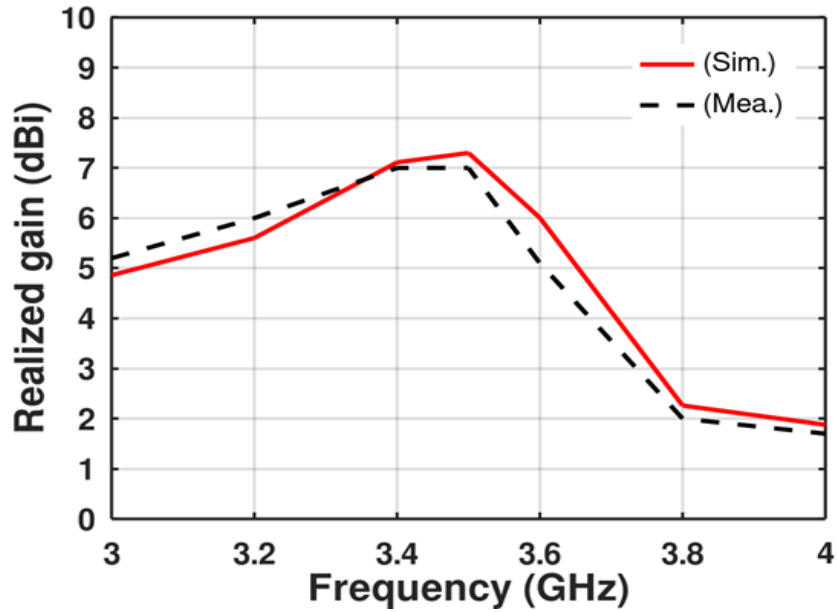
Figure 3.17: Simulated and measured gain of the proposed antenna.

Figure 3.18 shows the simulated as well as measured radiation efficiency of the proposed antenna. Imperfect fabrication, material properties not matching with their datasheet values and imprecise measurements may have led to difference in measured and simulated results. It can be noted from the figure that the antenna is moderately efficient. The efficiency can be increased if materials with smaller losses are used. But in the current design, we wanted to keep the cost of the antenna low so FR4 was used instead of costlier dielectrics with low loss tangent.
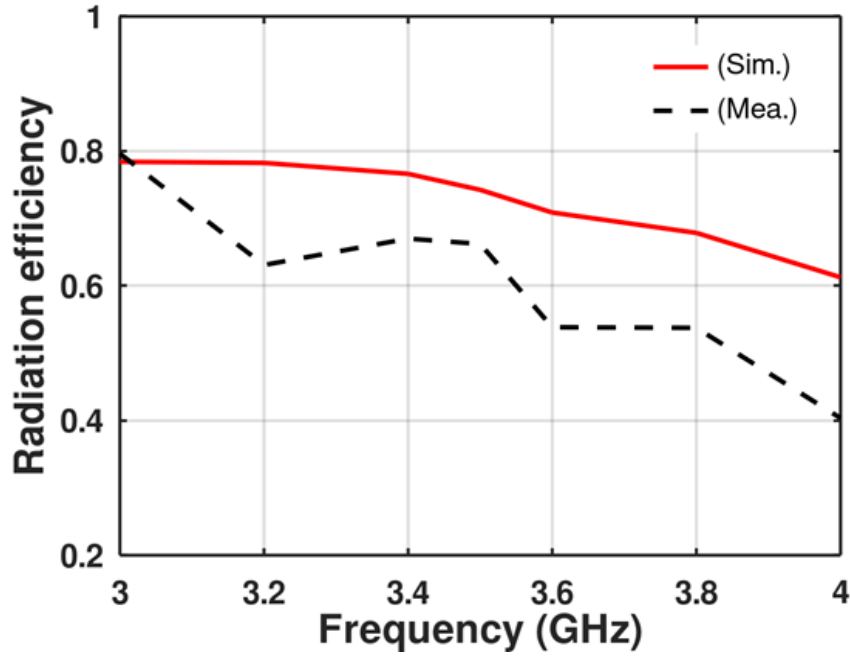
Figure 3.18: Efficiency of the proposed antenna.

3.8　Observations and Comparisons of Proposed Antenna with Existing Design

The performance of the proposed designed antenna has been discussed in this section. Table 3.1 gives the comparison between related reference antennas published in the literature [63, 64, 68, 71, 74] and presented antenna.

Table 3.1 shows the comparison of different antennas in literature and the proposed antenna in this work. We can see that the proposed antenna has the highest gain compared to other antennas while its size is also very competitive. With these characteristics, this antenna can be used for WiMAX. It can be a good candidate for 5G if used with similar antennas in MIMO configuration.

Table 3.1 Comparison of the proposed antenna with other reported work

References	Size (λ^3)	Bandwidth (GHz)	Realized Gain (dBi)
[63]	$\frac{\pi}{4} \times 0.82^2 \times 0.24$ ($\pi/4 \times 3^2 \times 29\ mm^3$)	2.38–2.54 (6 %)	3.9

[64]	-	2.15–4.6 (72 %)	3.7-5.46
[68]	$0.32 \times 0.32 \times 0.025$ ($42.8 \times 42.8^2 \times 3.57\ mm^3$)	1.98 - 2.08 (4.9 %)	3.7
[71]	$1.12 \times 1.12 \times 0.09$ ($61.1 \times 61.1 \times 4.9\ mm^3$)	4.83–6.25 (12 %)	6
[74]	$4.05 \times 4.05 \times 1.21$ ($100 \times 100 \times 31.6\ mm^3$)	5.71-5.87 (2.7 %)	6.8
This Work (Design 3)	$\mathbf{1.22 \times 1.22 \times 0.798}$ ($50 \times 50 \times 32.6\ mm^3$)	**3.2-3.75 (15.8 %)**	**7**

3.9 Conclusion

In this chapter, a coplanar waveguide fed monopole antenna over an artificial magnetic conductor with three different superstrates is designed. The performance of the proposed antenna with three different superstrates was studied and an antenna-AMC composite was fabricated with one of the superstrates.

Design -1 is based on a metasurface superstrate placed over the AMC-based monopole antenna where the grid of 5×5 metallic square patches is printed on the dielectric. The proposed metasurface superstrate increased the gain of the antenna, however, such type of material fabrication is not easy.

Design-2 is based on a high dielectric superstrate over the AMC-based monopole antenna. The proposed high dielectric superstrate increases the gain of the antenna however, these

materials are either not available commercially-off-the-shelf or are very expensive compared to traditional dielectrics.

Design-3 is based on a low dielectric superstrate over the AMC-based monopole antenna. The low dielectric superstrate AMC-based monopole antenna increases the gain of the antenna. The low dielectric superstrate is cheap and easily available. In this way, we discussed three different superstrates and discuss how they can be used in place of each other without sacrificing the antenna performance. Finally, one of these three superstrates is fabricated with the monopole and AMC combination.

Its performance in terms of gain, S_{11}, and radiation pattern have been simulated and measured. The proposed antenna operated in the 3.2-3.75 GHz band, which achieved a high gain of 7 dBi and can be used for 5G and WiMAX applications.

CHAPTER 4

Metasurface Superstrate Beam Steering Antenna with AMC

4.1   Introduction

In the last two chapters, the concept of the artificial magnetic conductor (AMC) and superstrate techniques was proposed and discussed. Based on these concepts, the high gain has been achieved in different antennas i.e., PIFA as well as a monopole antenna.

Conventional antennas cannot be used for 5G until they have the capability of beam steering. In 5G, the beam steering capability of the antenna plays the main role for efficient coverage to all users.

Literature reveals, based on the monopole antenna achieving beam steering technique, there are many published research attempts to beam steering in antenna [85-98]. The waffle and waffle iron waveguides used obtained beam scanning of 10° but it makes the design bulky and fabrication is also complex [85]. However, Birefringent Prisms achieved beam scanning but it has the limitation of beam walkof [87]. The optical phased array on silicon-on-insulator which achieves 2.3° at a wavelength of 1550 nm and 14.1° steering whereas the cost is high and has a complex design [89]. The limitation of complicated design can also be overcome using a grid of 5× 5 electrically small rectangular-shaped metallic pixels on the upper layer of the parasitic layer which are connected by switches [89].

In this chapter, we explore a beam-steering antenna based on a non-uniform metasurface superstrate and AMC as beam steering with low scan loss is going to be a necessity for 5G communications.

Figure 4.1 gives the designed methodology of the presented antenna in this chapter.
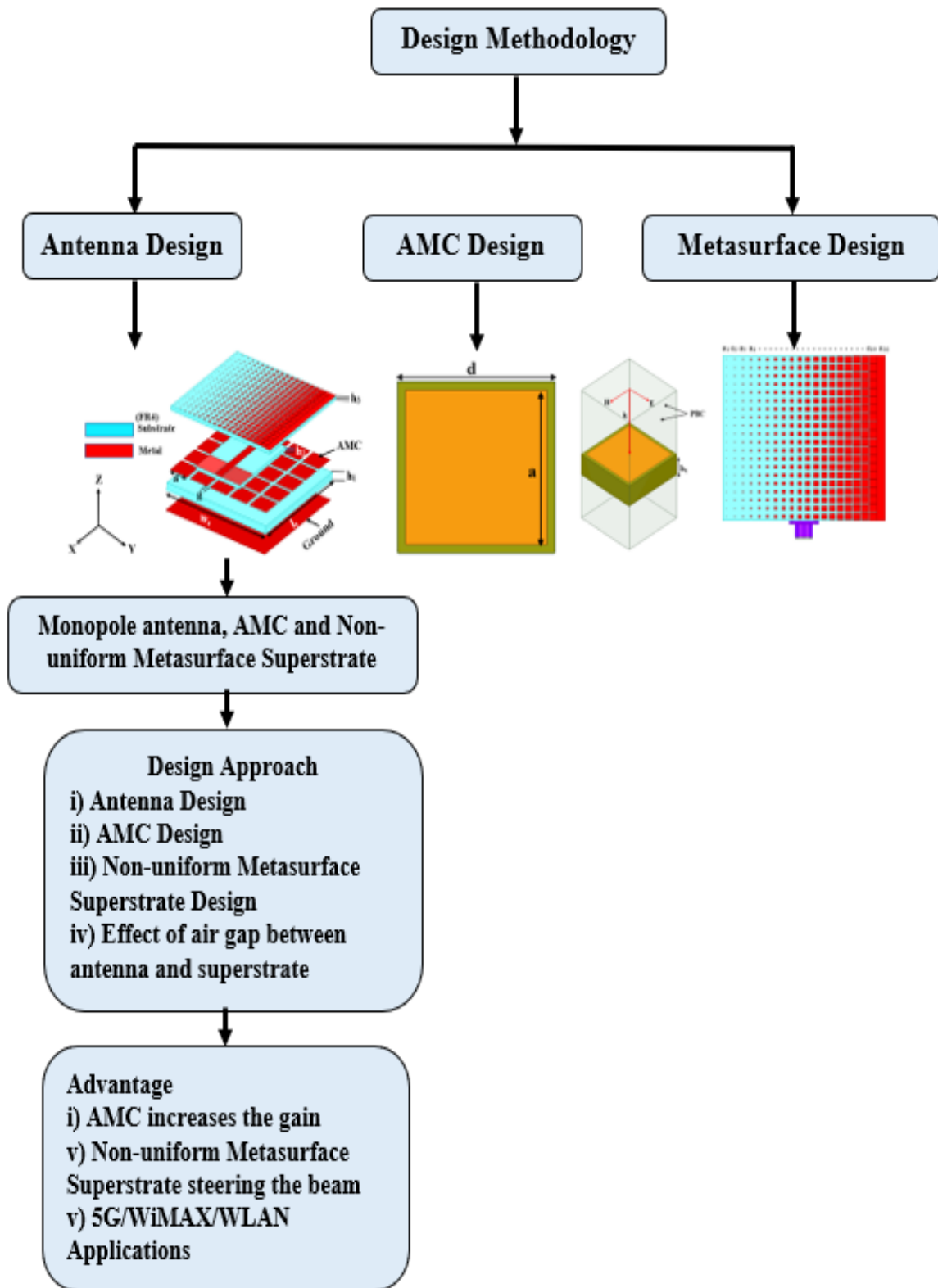
Figure 4.1: Designed methodology of the chapter-4 antenna.

4.2   Geometry of the Proposed Antenna

4.2.1 Design of CPW-fed Monopole Antenna

The radiating element, CPW-fed monopole antenna, geometry is shown in Figure 4.2. Due to the simple design and single side design on the substrate, this radiating element is selected for this research. For design, the length of the monopole antenna is denoted as l, and width is denoted by W. The monopole antenna is fed through a 50 Ω SMA connector. The antenna is fabricated on an FR4 ($\varepsilon_r = 4.4, \tan\delta = 0.02$) substrate with a thickness of 1.6 mm. The other dimensions of the antenna are given as: $L_p = 35, W_p = 22, l = 16.7, m = 9.1, g = 0.3, l_1 = 10$ (all dimensions are in mm).
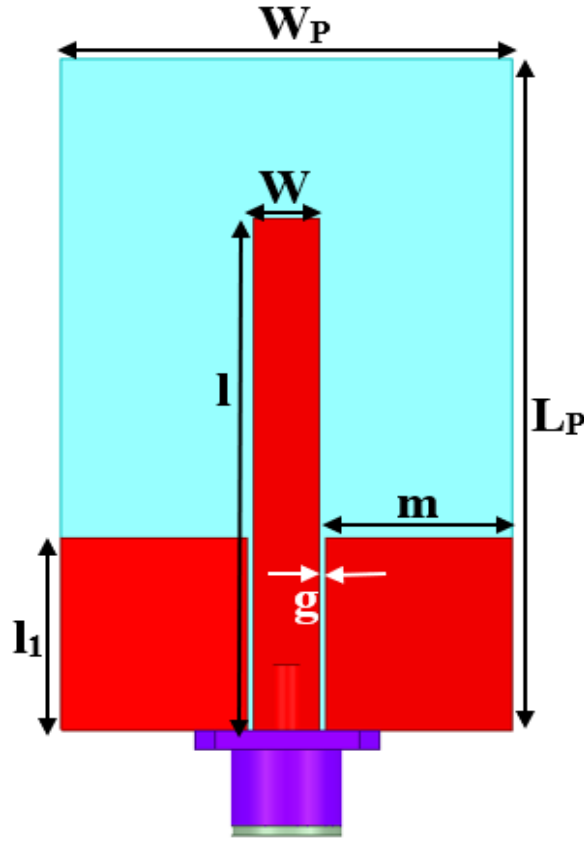
Figure 4.2: Proposed CPW fed monopole antenna.

4.2.2 Design of AMC for CPW fed Monopole Antenna

The center frequency of AMC operation is chosen to be 3.5 GHz. A unit cell of periodicity 10 mm × 10 mm is used for AMC design. Square-shaped metallic patches of side 'a' are

printed at the center of the unit cell on FR4 substrate as shown in Figure 4.3 (a). The substrate has a thickness, $h_1 = 3.2$ mm with permittivity of 4.4 and a loss tangent of 0.02. For analysis of AMC, the periodic boundary condition (PBC) is used. It facilitates quick results instead of simulating the large structure of AMC. By using PBC, shown in Figure 4.3 (b), the reflection phase is calculated by simulation with the help of Floquet port excitation.

In order to ascertain that the AMC is indeed working on desired 3.5 GHz, a unit cell simulation with the variable side of the square pixel, *a*, is run and an attempt is made so that the reflection phase is 0° at desired 3.5 GHz. From Figure 4.3 (c), we can see that when the side of the pixel, *a,* is 9.6 mm, the reflection phase is 0°. Henceforth, we will use AMC made of unit cells with $a = 9.6$ mm to use with the monopole antenna discussed earlier.

(a)

(b)

(c)
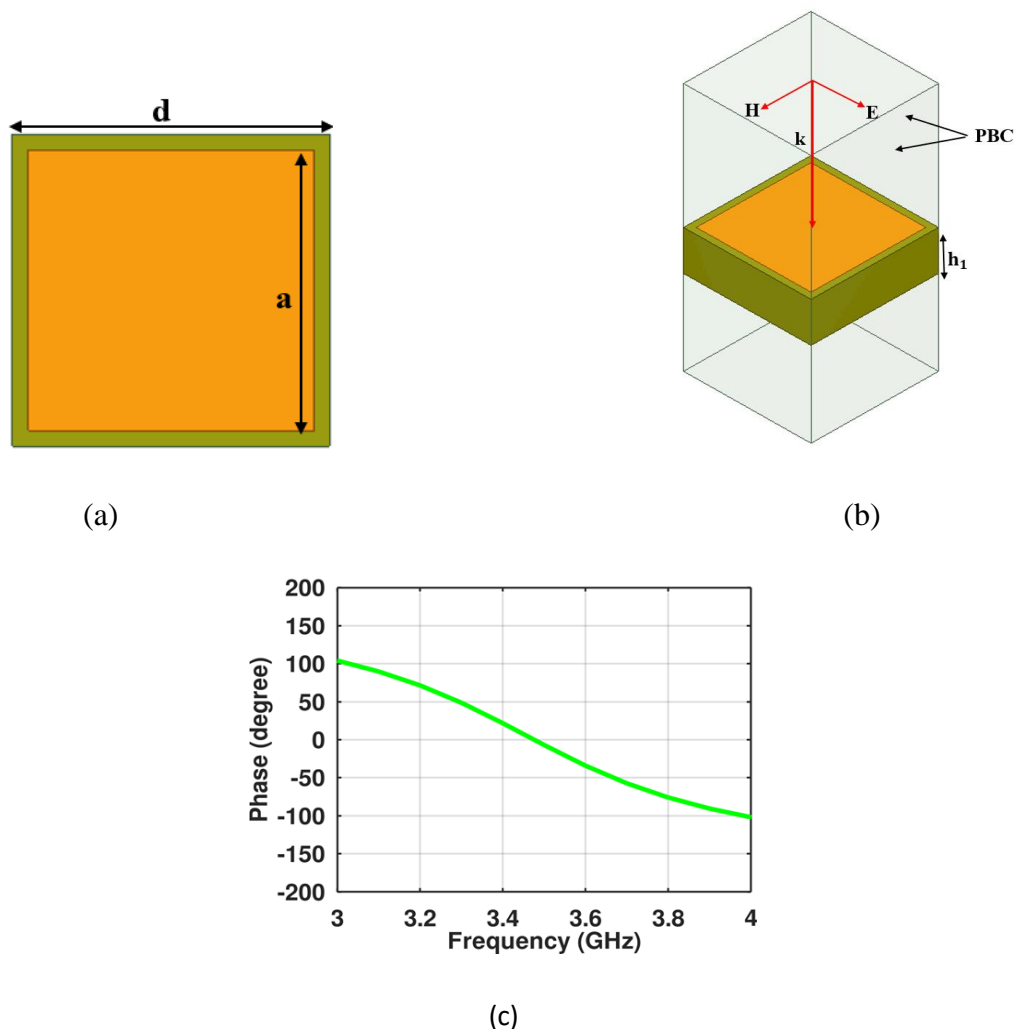
Figure 4.3: AMC design for proposed CPW fed monopole antenna, (a) top view of AMC, (b) isometric view of AMC, (c) reflection phase behaviour of the AMC.

4.2.3 Design of Composite CPW fed Monopole Antenna with AMC and Superstrate

In the previous section, AMC is designed. Next, place AMC is placed underneath the antenna substrate as shown in Figure 4.4 so that the AMC enhances the radiation in the forward direction, i.e., along vertically up direction. It can be seen from Figure 4.4 that a grid of 5×5 AMC unit cells is placed under the monopole antenna. It is well known that the superstrate can be used to increase the gain of the antenna [24, 25, 26, 27]. Mostly, the superstrate used for enhancing the design is either in the form of uniform pixels or pixels whose size changes radially out from the center of the superstrate. In such applications, the primary role of superstrates is to work in Fabry-Perot configuration and enhance the gain of the antenna element. In this research, we have a dual purpose of the superstrate. On one hand, we want to modify the gain of the antenna and on the other, we want to steer the beam emanating from the antenna in the desired direction. This type of beam steering is very important for upcoming 5G systems. Figure 4 (a) shows the geometry of the proposed superstrate which comprises of metallic patches of different sizes from a_1 to a_{20}. The dimensions of the proposed superstrate are given in Table 4.1.

In order to steer the beam in a direction away from the broadside, there should be phase variation for waves emanating from different locations of the superstrate. This phase-varying behavior is provided by a nonuniform metasurface printed on the dielectric substrate acting as a superstrate. For this purpose, the size of the unit cells of the superstrate increases monotonically from one edge to another of the superstrate as shown in Figure 4.5 (a). In this way, the superstrate will help to steer the beam in an off-broadside direction. If this superstrate sends the beam in $+\theta$, rotating the superstrate by 180°, taking the z-axis for rotation, will help to send the beam in the $-\theta$ direction. In order to send the beam in the broadside direction, the superstrate is removed. To ease the rotation, the interchange of the superstrate may be accomplished by a mechanical solution. In this way, this design can be said to be reconfigurable. However, the speed of beam steering will depend upon how quickly the mechanical motor can help to rotate or remove the superstrate.

Figure 4.5 (b) shows the layered structure of the proposed CPW fed monopole antenna with AMC and superstrate with different views. The fabricated prototype of the proposed antenna is shown in Figure 4.6.
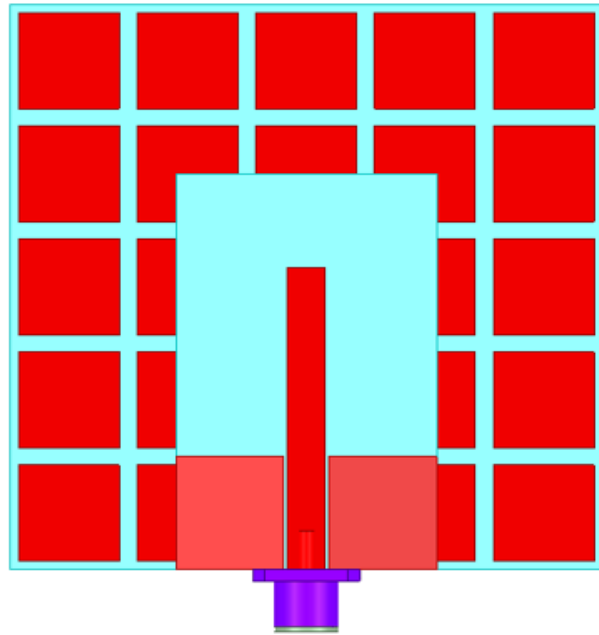
Figure 4.4: CPW fed monopole antenna with AMC.

Table 4.1 Patch dimensions (in mm) used in metasurface superstrate.

a_1	a_2	a_3	a_4	a_5	a_6	a_7	a_8	a_9	a_{10}
0.125	0.25	0.375	0.5	0.625	0.75	0.875	1	1.125	1.25
a_{11}	a_{12}	a_{13}	a_{14}	a_{15}	a_{16}	a_{17}	a_{18}	a_{19}	a_{20}
1.375	1.5	1.625	1.75	1.875	2	2.125	2.25	2.375	2.5
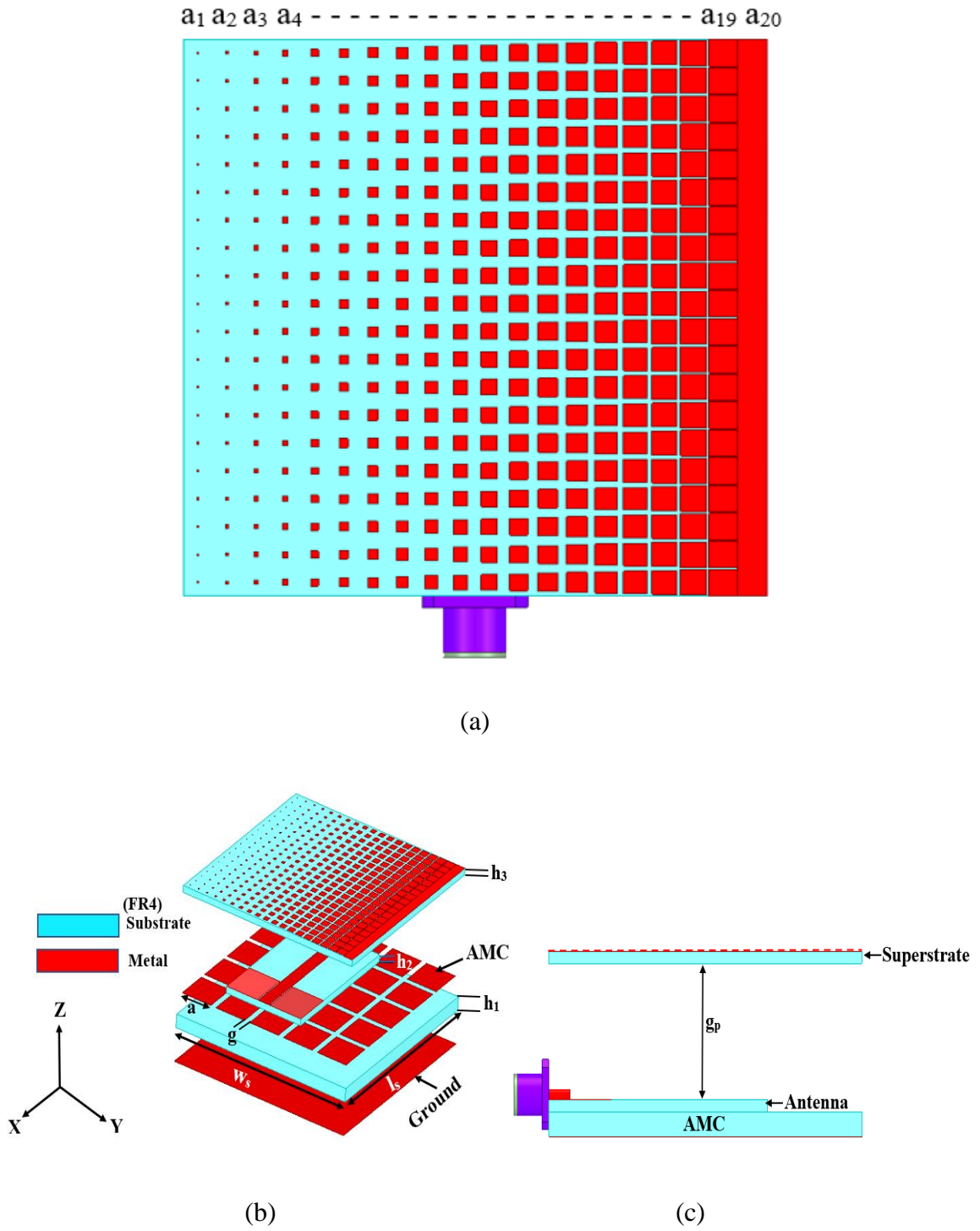
Figure 4.5: CPW fed monopole antenna with AMC and superstrate. (a) layered structure, (b) side view.

($l_s = 50, W_s = 50, h_1 = 3.2, h_2 = 1.6, h_3 = 1.6, g = 0.17, g_p = 7.2$, all dimensions in mm)
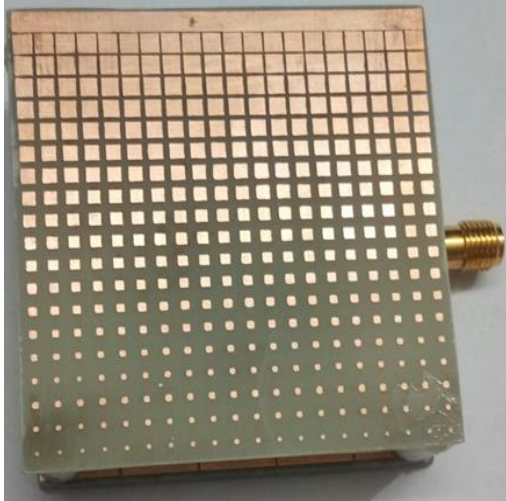
(a)
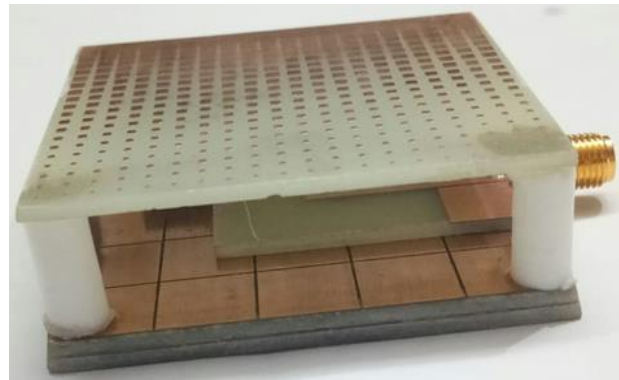
(b)
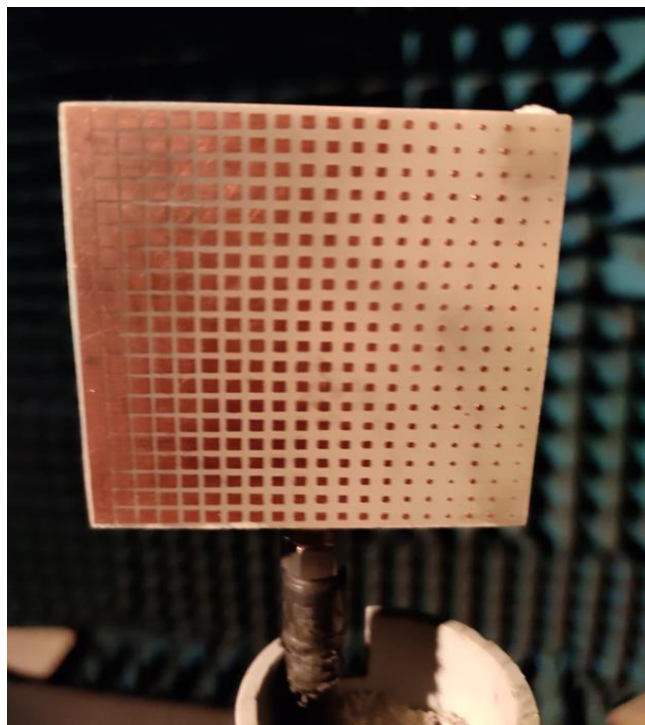
(c)

Figure 4.6: Prototype of the proposed CPW fed antenna with AMC and superstrate, (a) top view, (b) side view, (c) antenna in an anechoic chamber for measurement.

4.3 Parametric Analysis

The parametric studies of the dimensions of the monopole antenna, the gap between antenna and superstrate has been carried out to achieve good impedance matching and desired frequency band.

4.3.1 Length of Monopole Antenna

The length of the monopole antenna, l, is varied from 20 mm to 30 mm with the step size of 5 mm. As shown in Figure 4.7 (a) the reflection coefficient S_{11} is lower than -10 dB for desired frequency bands. It can also be observed that the S_{11} resonance moves to a lower frequency as the length of the monopole increases.

4.3.2 Air Gap Between Antenna and Superstrate

The gap between antenna and superstrate is varied from 4.2 mm to 10.2 mm with a step size of 3 mm. It can be seen from Figure 4.7 (b) that there is hardly any effect of varying the gap on the antenna performance. In this way, the antenna will give almost the same results even if the gap changes due to slight mishandling of the antenna.

(a)   (b)
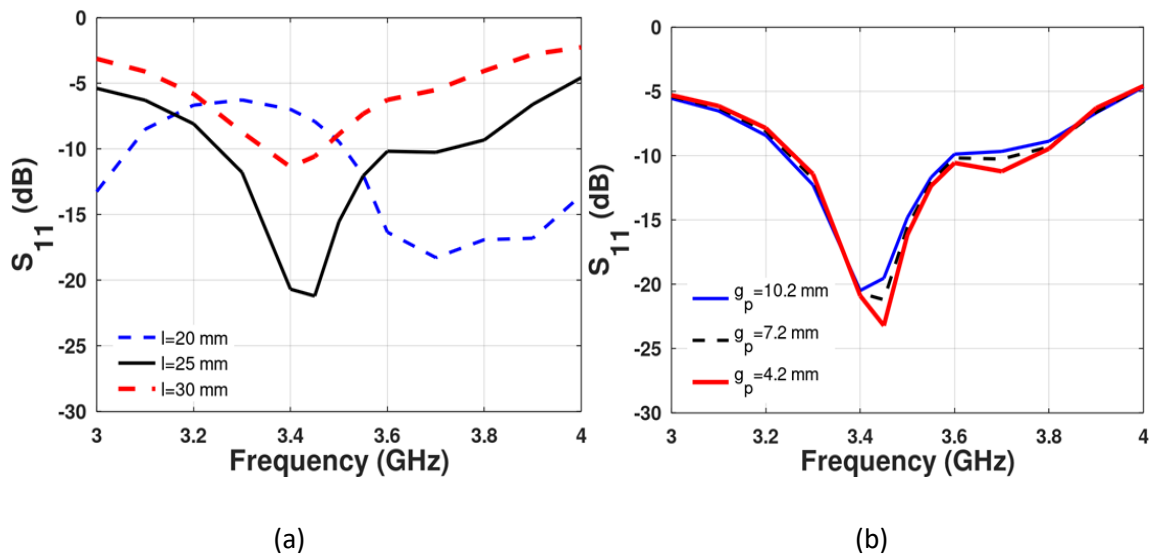
Figure 4.7: Parametric analysis of the antenna using: (a) monopole antenna length 'l'; (b) gap between antenna, and superstrate 'g_p'.

4.4 Simulated and Measured Results

All the simulations in this work are conducted using Ansys HFSS, a full-wave simulator. The simulated S-parameter comparison of the monopole antenna, monopole antenna with AMC, monopole antenna with AMC, and superstrate is shown in Figure 4.8.
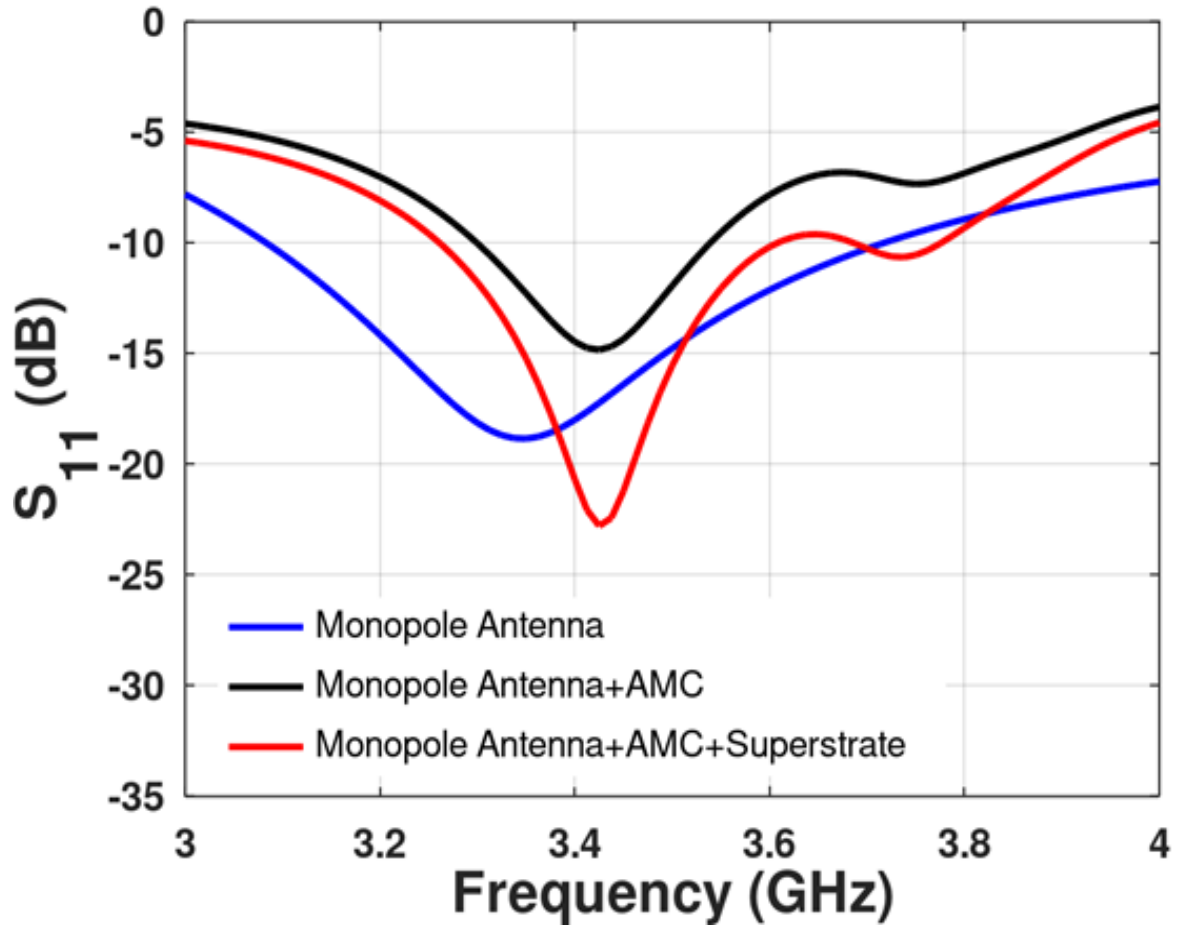
Figure 4.8: S-parameter comparison of the monopole antenna with AMC and superstrate.

The comparison of the realized gain for monopole antenna with AMC and superstrate is shown in Figure 4.9. It can be observed that there is a 3.84 dBi increment in gain after applying AMC on the monopole antenna. Furthermore, when the superstrate is applied, the gain of the antenna is 5.5 dBi at 3.5 GHz.
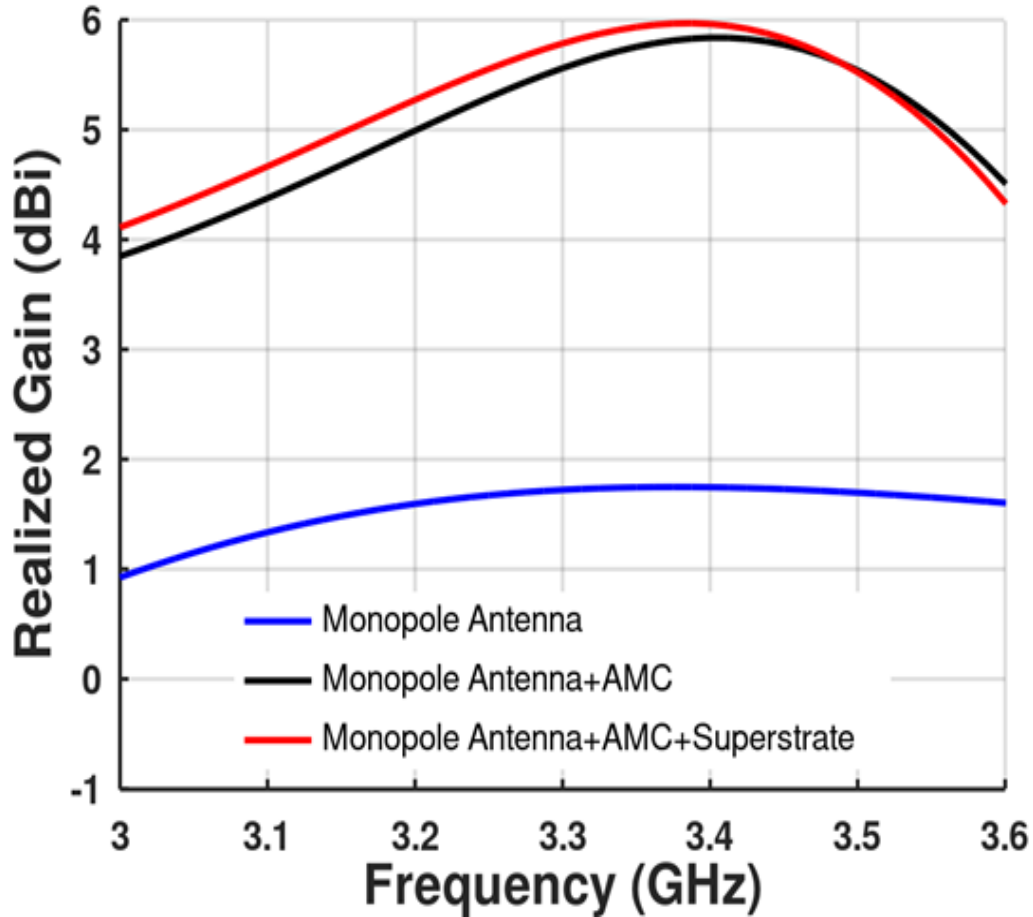
Figure 4.9: Realized gain comparison of the monopole antenna with AMC and superstrate.

In order to get insights into the working of the superstrate, near field behaviour is very helpful. The far-field pattern, being the Fourier transform of the near-field pattern, can give a better understanding of how the superstrate is changing the near field that will eventually change the far-field characteristics. To accomplish it, a vertical plane in the center of the antenna is placed on which the dominant component of the near field is studied. In our case, E_x is the dominant electric field as the monopole is aligned along the x-axis. In Figure 4.10 and Figure 4.11, E_x magnitude and phase behavior in the absence and presence of the superstrate are shown. It is evident from Figure 4.10 (a) and Figure 4.11 (a) that the placement of the superstrate confines the fields and hence shows slightly higher field magnitude in the case of the superstrate. It is also evident from Figure 4.10 (b) and Figure 4.11 (b) that due to placement of the superstrate, the direction of the equi-phase front changes. The phase front is changed towards the left, signifying that the outward radiation is expected towards the left side when

75

the superstrate is placed. From these figures, it is easy to understand that the absence or presence of the superstrate decides the beam steering direction.

(a)   (b)
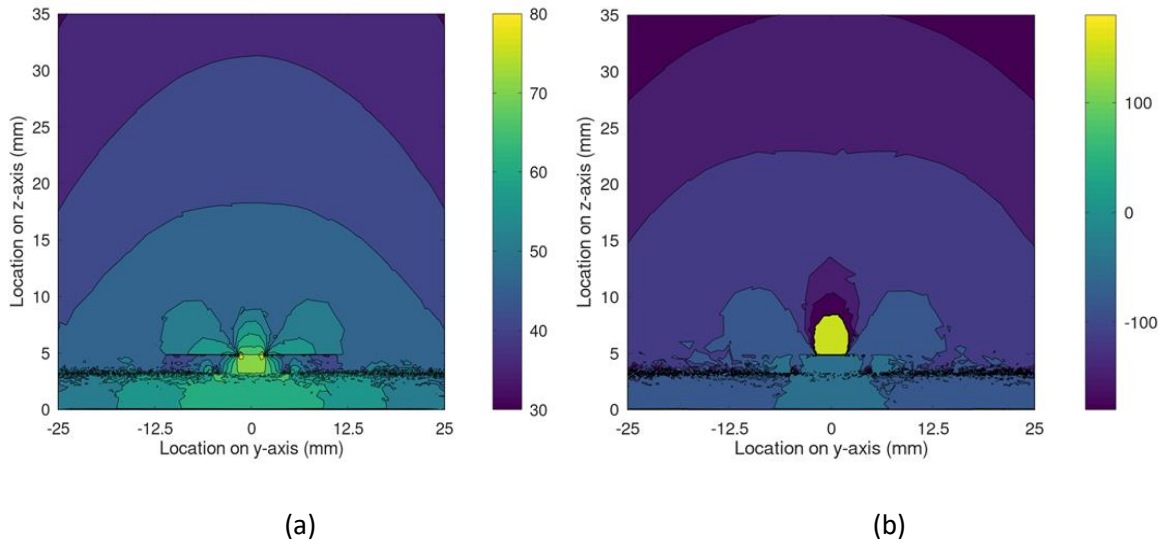
Figure 4.10: Near field performance of the antenna in absence of superstrate (a) E-field magnitude on a plane, (b) E-field phase on a plane.

(a)   (b)
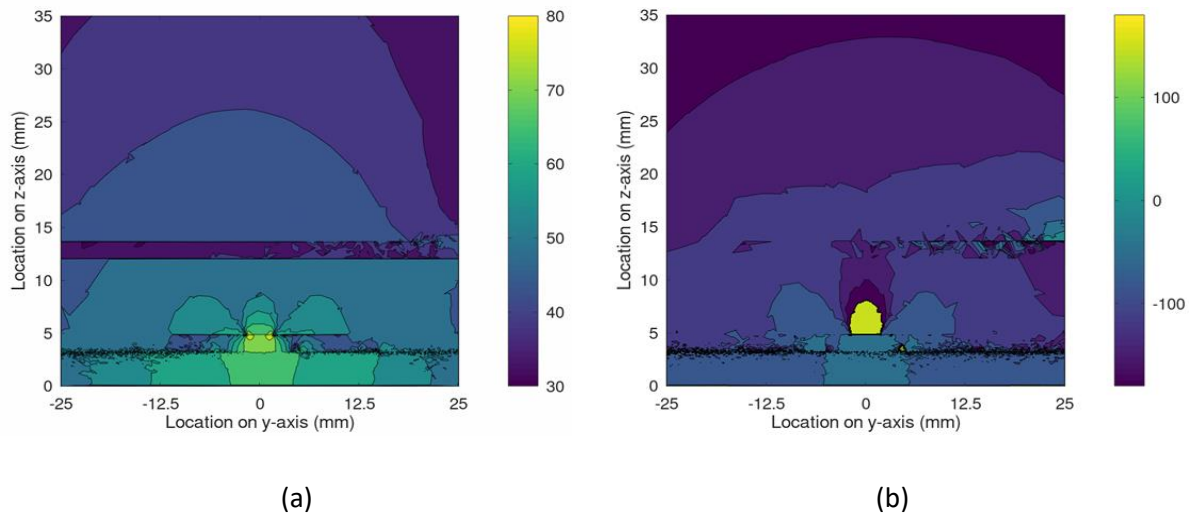
Figure 4.11: Near field performance of the antenna with superstrate (a) E-field magnitude on a plane, (b) E-field phase on a plane.

After getting the desired radiation properties, the prototype of the antenna is fabricated as shown in Figure 4.6. The proposed antenna is tested using an R & S ZNB40 vector network analyzer and anechoic chamber for its properties.

The simulated and measured S-parameters of the antenna are shown in Figure 4.12. For acceptable performance, the proposed antenna needs to provide good reflection coefficients, $|S_{11}|$, in the desired frequency band. From Fig. 12, it is evident that the fabricated antenna has $|S_{11}| < -10$ dB over the frequency band of 3.1-3.7 GHz. The simulated and measured S-parameters are in good agreement. The fabricated antenna has wide impedance bandwidth for 5G, WiMAX, and WLAN applications.
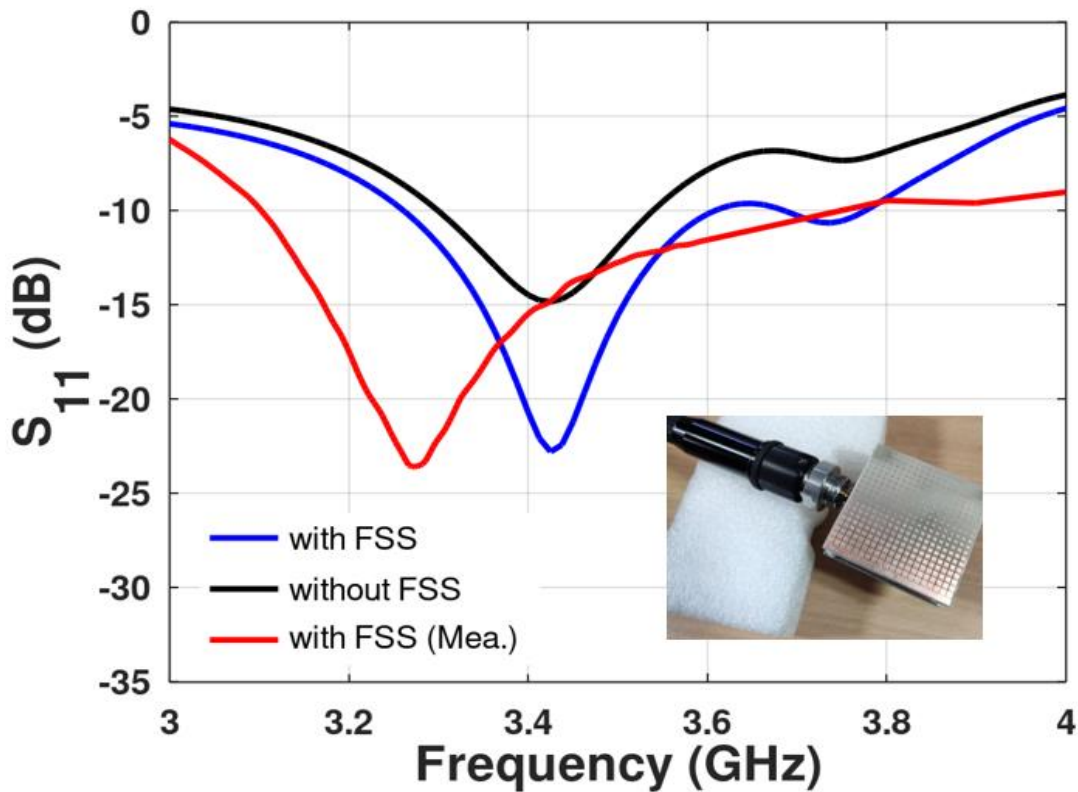
Figure 4.12: Measured and simulated S_{11} of the proposed antenna.

Figure 4.13 shows the radiation pattern of the proposed antenna for φ=0° cut. The non-uniform superstrate was designed to steer the beam in θ=±18°. The superstrate needs to be mechanically rotated or removed depending upon the desired steering beam direction. While, currently, we manually operated of mechanically placing and removing the superstrate but the superstrate can be moved by mechanical motor to automate this operation. This type of mechanical movement of a superstrate is simple and can be easily accomplished by mechanical motors. It can be seen from Figure 4.14 that the beam scans in ±18° and 0° in elevation directions in presence of superstrate and in absence respectively. It is also interesting

to note that the antenna does not show sidelobes in this plane. The realized gains at these steered angles are 5.5 dBi signifying that the antenna shows almost zero scan loss for ±18° scanning angles.
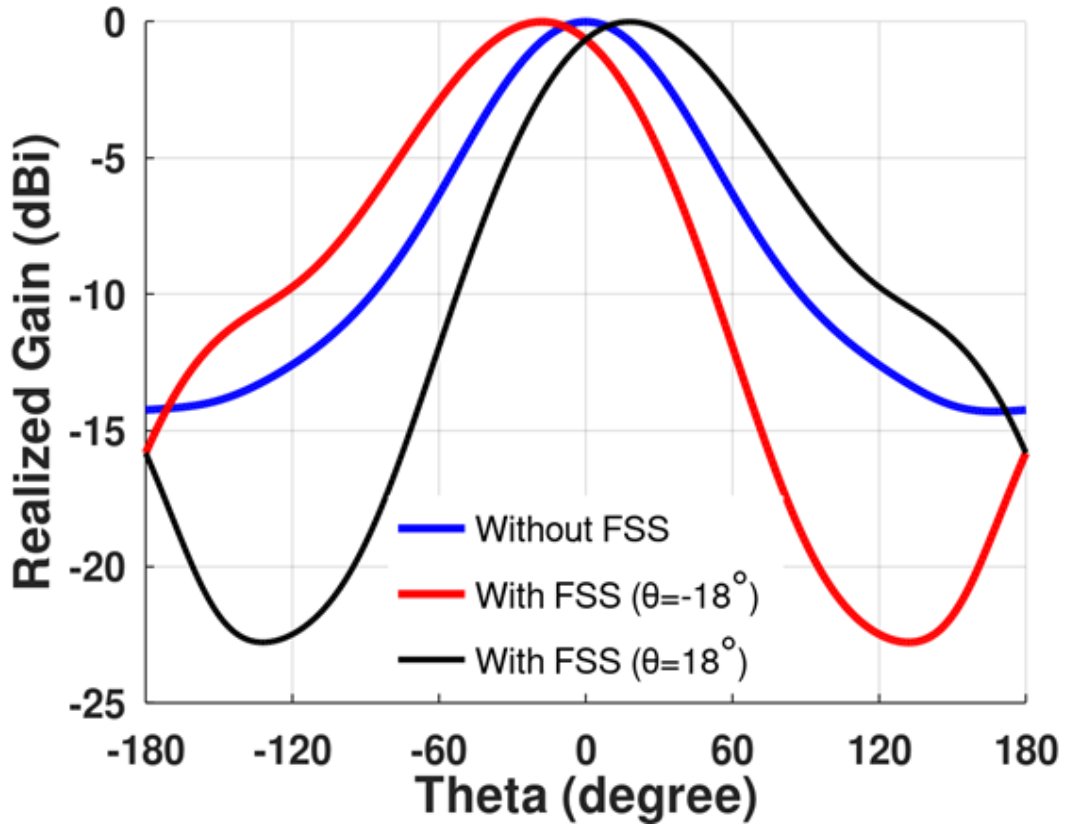
Figure 4.13: Radiation pattern in absence and presence of superstrate.

The proposed antenna radiation patterns (co- and cross-polarization) are measured in an anechoic chamber at 3.5 GHz as shown in Figure 4.14 and Figure 4.15. In these figures, co-polarization is shown by red lines and cross-polarization by black lines. It is evident from Figure 4.14 and Figure 4.15, that the antenna has very low cross-polarization components. The simulated and measured results are also in good agreement.

(a)   (b)
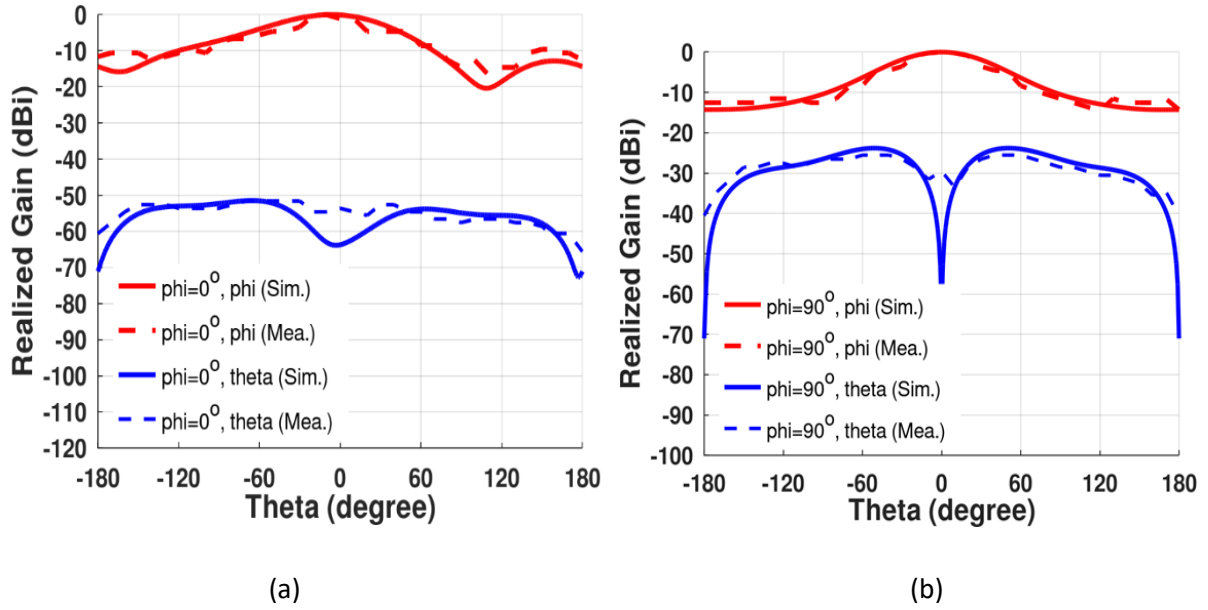
Figure 4.14: Simulated and measured radiation pattern of the antenna without superstrate, (a) φ=0° cut (b) φ=90° cut.

(a)   (b)
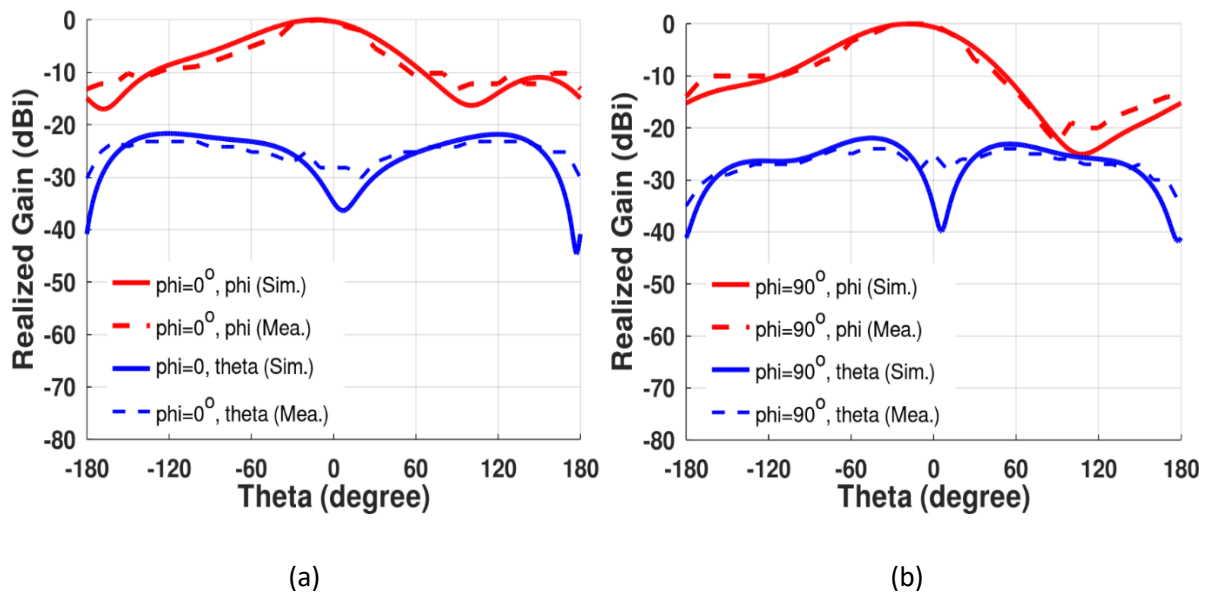
Figure 4.15: Simulated and measured radiation pattern of the antenna with superstrate, (a) φ=0° cut (b) φ=90° cut.

Figure 4.16 shows the simulated and measured gain of the antenna with and without superstrate. It is observed that the gain of the antenna in both cases is 5.5 dBi at 3.5 GHz. The simulated and measured values are also in good agreement.
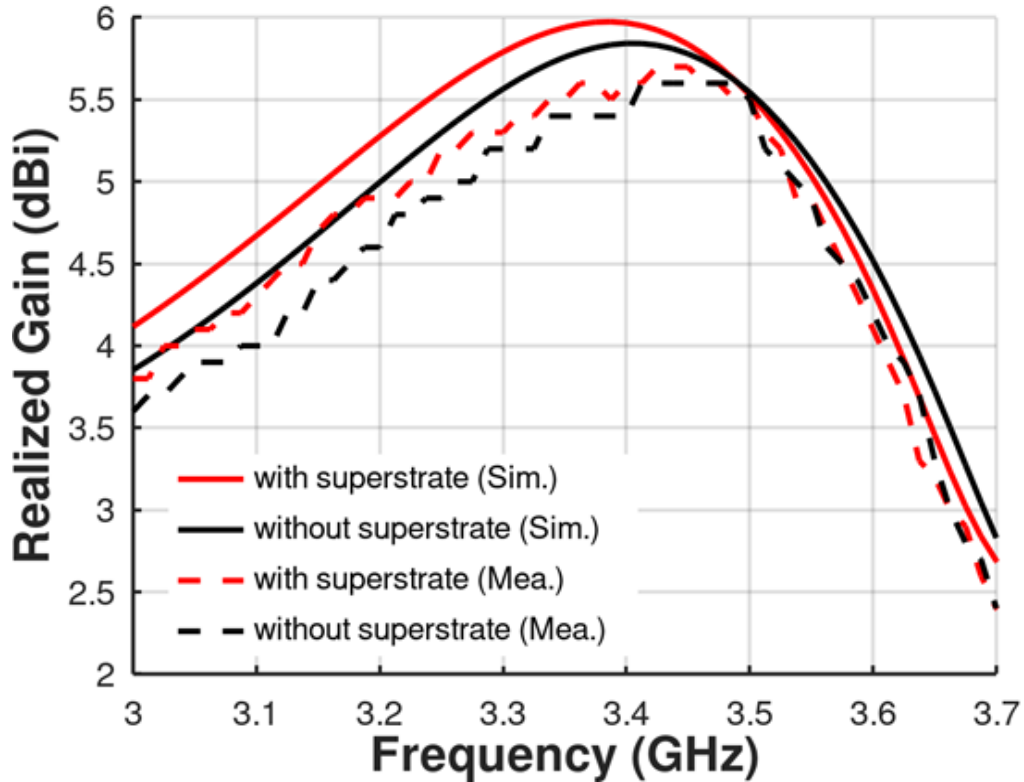
Figure 4.16: Peak realized gain of the antenna when the beam is steered in different directions.

4.5 Observations and Comparisons of Proposed Antenna with Existing Design

This section explores the antenna performances of the proposed antenna and compares them with other published work based on the beam steering techniques. Table 4.2 shows the relative comparison among the related reference antennas which have been published in the literature [85-90, 93-94, and 95] and proposed antenna. Most of the researchers were used phased arrays, Birefringent Prisms, lumped capacitances, and electronic switches to achieve beam steering but it increases the complexity and cost of the design.

The performance of the proposed designed antenna has been discussed in this section. In Table 4.2, all existing designs are compared with the current work. It is evident from Table 4.2 that the proposed antenna gives a good beam steering with a compact design.

Table 4.2 Comparison of present work with the previously published antennas

Ref	Antenna type	Size (λ^3_0)	Frequency band (GHz)	Realized gain (dBi)	Beam scanning (Degrees)
[90]	Phased array and reconfigurable PRS structure	$3.1 \times 3.1 \times 0.55$	5.5 to 5.7	12	$\pm 15^o$
[93]	Parasite patches and lumped capacitances	$1.56 \times 0.63 \times 0.013$	2.45	5-8	$\pm 15^o$
[94]	Parasitic phased array antennas	$0.30 \times 0.78 \times 0.005$	1	7.4	$\pm 15^o$
[95]	Tunable parasitic	$0.49 \times 0.49 \times 0.0013$	2.43-2.47	3.36	$\pm 40^o$
This Work	Metasurface monopole Antenna	$0.58 \times 0.58 \times 0.16$	3.1-3.7	5.5	$\pm 18^o$

4.6 Conclusion

In this chapter, a non-uniform metasurface superstrate is utilized over the AMC-based monopole antenna to obtained beam steering operating at 3.5 GHz (3.1-3.7 GHz). The proposed antenna structure consists of a top layer of non-uniform metasurface superstrate made of a 20×20 grid of electrically small square-shaped metallic pixels while the bottom part consists of AMC with a grid of 5×5 pixels. The radiating element, CPW-fed monopole

antenna, is placed between AMC and the superstrate. The antenna can steer the beam along θ = -18° and 18° in elevation while maintaining a uniform gain of 5.5 dBi with the non-uniform superstrate and along θ = 0° in the absence of the superstrate with almost zero scan loss.

The antenna due to these qualities is an ideal candidate for 5G, WiMAX, and WLAN applications.

CHAPTER 5

Wideband Slotted Planar Inverted-F Antenna using Eccosorb MCS Absorber for Millimeter-Wave Applications

---

5.1 Introduction

The concept of artificial magnetic conductors (AMCs), superstrates, uniform metasurface superstrates, and non-uniform metasurface superstrates was addressed in the last chapters. Still, all the above techniques lag the wide bandwidth for 5G communication. But, higher bands of frequencies provide wider bandwidth and can be used for beamforming. The mm-wave band, which has an unused wide spectrum, is a potential possibility in this regard. Researchers are looking into the mm-wave band for future fifth-generation (5G) antennas to avoid some of the concerns mentioned above [99].

In this chapter, radiation pattern transformation with wide band and high gain has been explored. The RF absorber (Eccosorb MCS) is used to improve the performance of the antenna in terms of pattern transformation, wide band, and high gain.

In literature, various structures have been proposed which are either embedded inside the antenna or used as a cover over the antenna to achieve high gain, radiation pattern transformation, or wideband operation. The distorted radiation pattern at mm-wave is improved by stacking of six pieces of the substrate, placed in a radome [101]. However, radiation pattern improvement is carried out by conducting post around the slots which supress the surface wave and remove the ripples from E-plane [109]. The high impedance surface (HIS) suppress the surface waves which enhance gain and obtained wide bandwidth in [110]. Various research articles are presented including phased array, MIMO, parasitic patches, metasurfaces, substrates to obtain radiation pattern transformation, high gain and wide bandwidth [99-106].

To achieve high gain and wide bandwidth, Feng *et al*. a proposed a layer of three substrates is provided, with the top superstrate consisting of 77 square patch cells meta surface [112].

In this chapter, we explore a radiation pattern transformation technique of the slotted planar inverted-F antenna (PIFA) using an Eccosorb MCS absorber. Figure 5.1 gives the designed methodology of the presented antenna in this chapter.
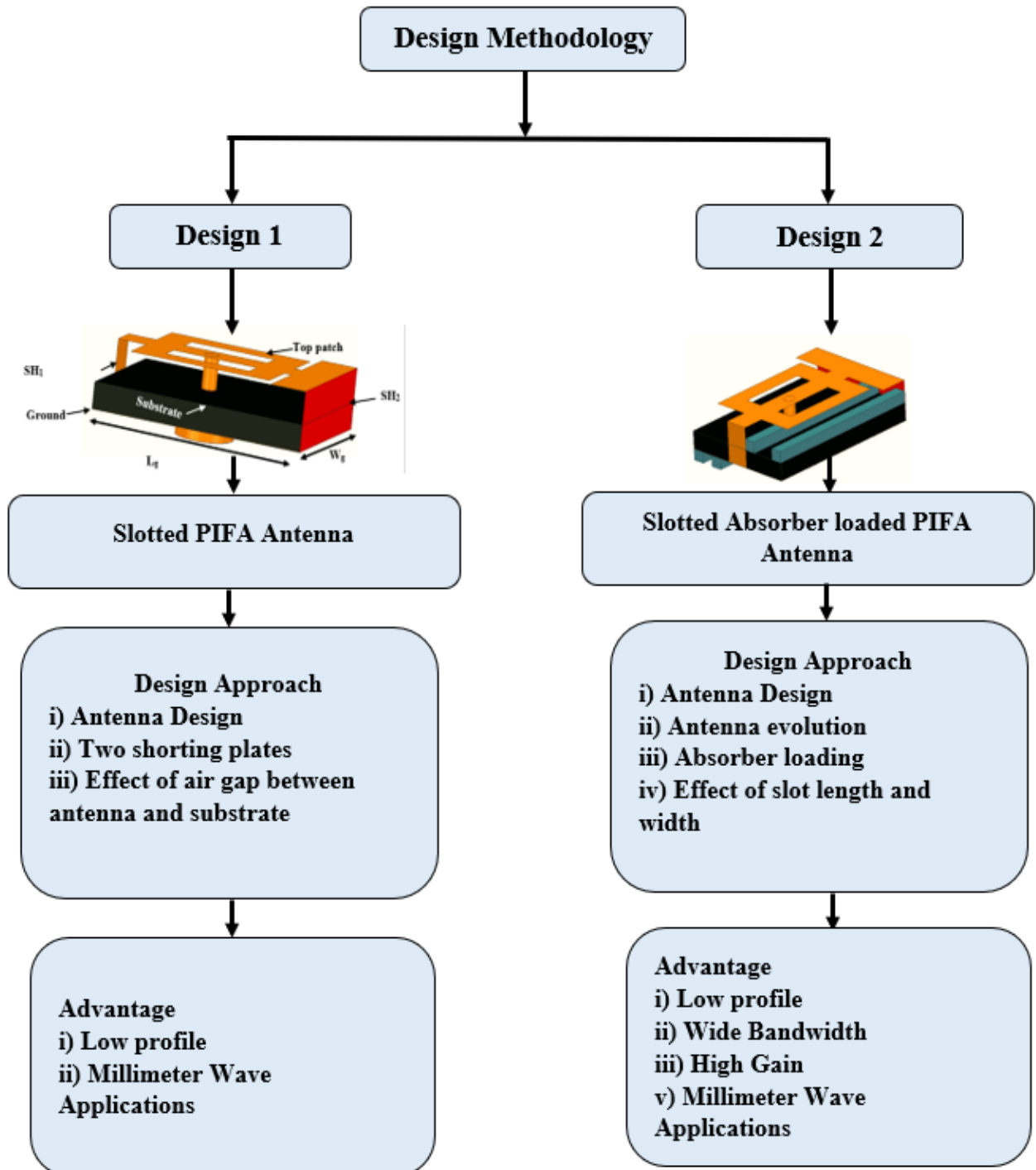
Figure 5.1: Designed methodology of the chapter-5 antenna.

5.2   Design of Slotted PIFA Antenna

Figure 5.2 shows the proposed slotted planar inverted-F antenna design. The antenna is designed on a 1.6 mm thick RT/Duroid substrate with 20 mm (L_g)×10 mm (W_g). The patch's dimension are $0.90\lambda_o \times 0.72\lambda_o \times 0.32\lambda_o$ (λ_0 at 27.3 GHz). The laminate used has a relative permittivity of 2.2 and a dielectric loss tangent of tan (δ) = 0.0009 and is separated by a 0.035 mm thick patch.

P= 0.18 λ_0 is the air gap between the patch and the substrate whereas SH_1 is the narrow plate and SH_2 is the wide shorting plate. The narrow shorting plate is soldered to one end of the radiator to the ground at a distance of F1 and the wide shorting plate is soldered to another end of the radiator at a distance of F2 from the feed position. The impedance of the antenna is maintained by the distance between both shorting plates and feed. The 2.92 mm N-type connector is used to feed the top copper radiator. Figure 5.2 (a) shows the two slots ($l_s \times W_s$) etched on the radiator and two stubs S_1, S_2 (0.27 λ_0×0.045 λ_0) which help to improve impedance bandwidth and affect the return loss.

(a)   (b)

(c)
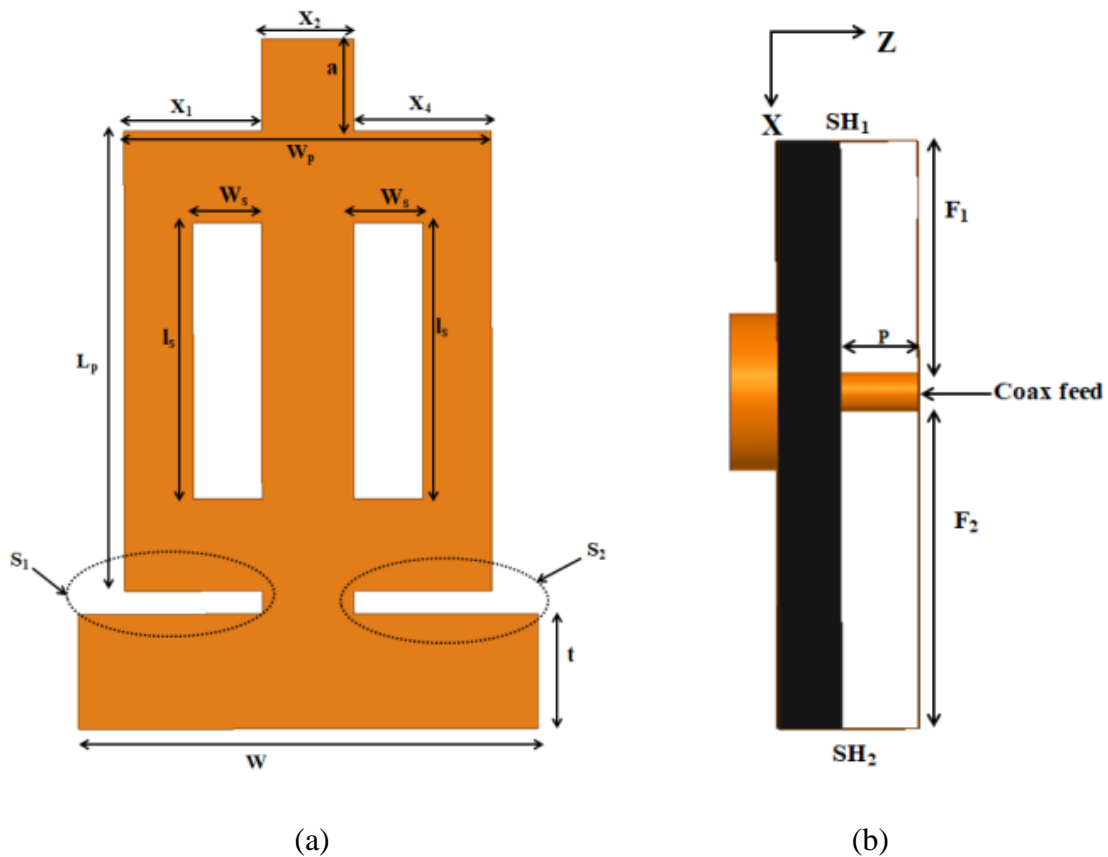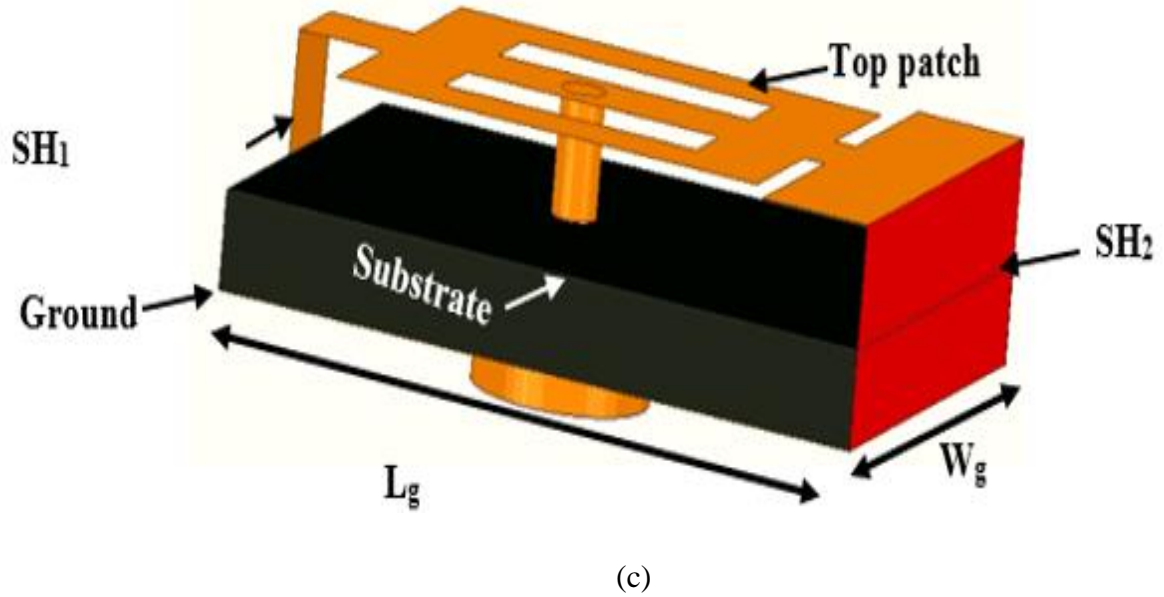
Figure 5.2: Geometry of the proposed slotted PIFA antenna (a) top view of the slotted patch, (b) side view (c) 3D view of the antenna.

Figure 5.2 depicts the proposed antenna's optimal parameters i.e., $L_p = 0.90\lambda_o$, $W_p = 0.72\lambda_o$, $W = 20$ mm, $X_1 = 3$ mm, $X_2 = 2$ mm, a = 2 mm, $X_4 = 3$ mm, $W_s = 1.5$ mm, $l_s = 6$ mm, t = 2.5 mm, $F_1 = 6.4$ mm and $F_2 = 8.6$ mm, respectively.

5.3 Design of Eccosorb MCS Absorber Slotted PIFA Antenna

Figure 5.3 depicts the absorber-loaded slotted PIFA antenna geometry. On the top and bottom parts of the substrate, four strips of elastomeric microwave absorbers are loaded. The absorber's relative permittivity is $\varepsilon_r = 15$ and the loss tangent is $\tan(\delta) = 0.002$. The absorber loaded PIFA antenna has a dimension of $3.4\lambda_o \times 2.7\lambda_o \times 1.2\lambda_o$ and a thickness of 1 mm. The two absorber strips are placed above the substrate with 'Y_2' space between them. The remaining two strips are positioned near the other edge of the substrate, on the bottom part of the substrate with a gap of 'X_3'.
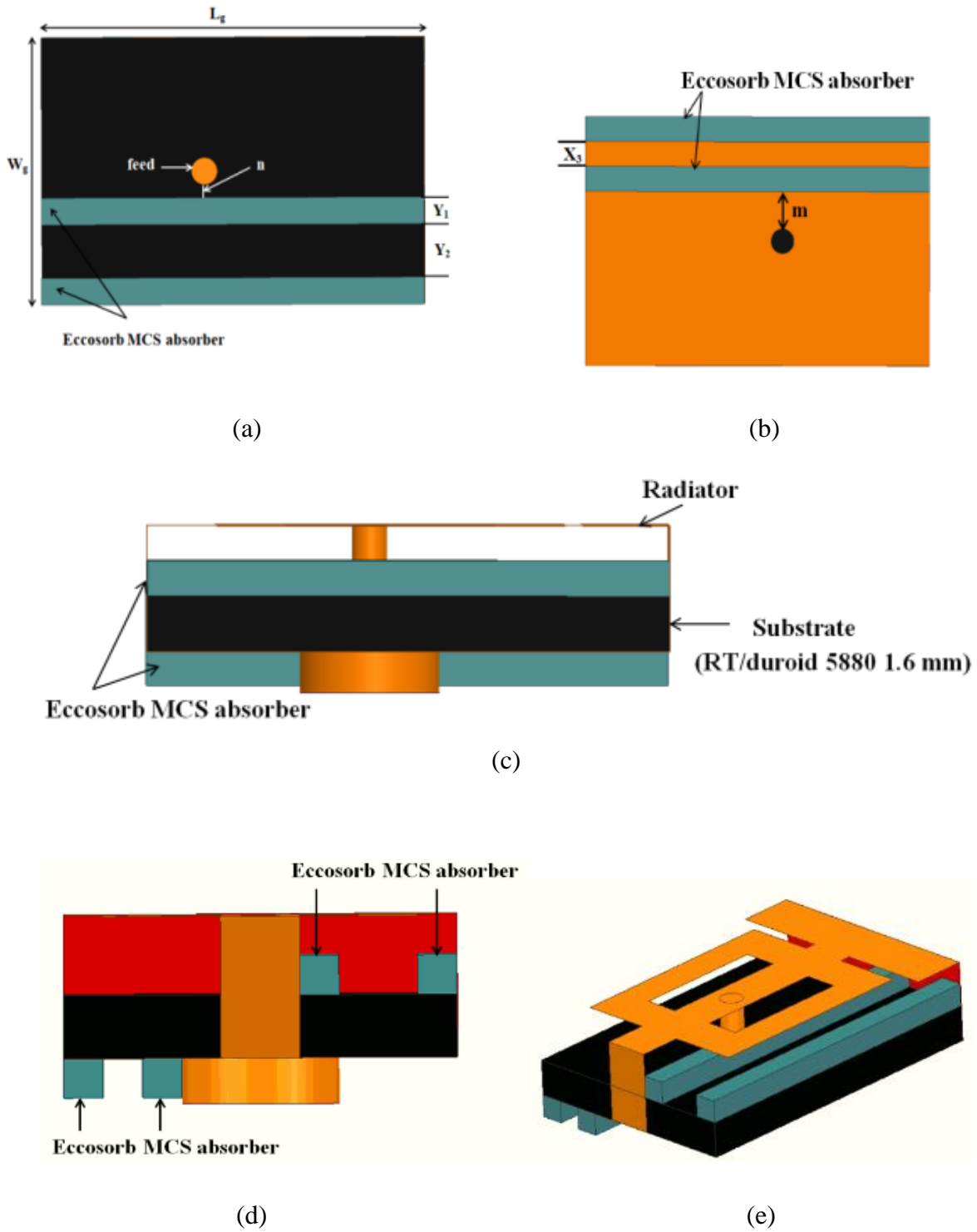
Figure 5.3: Geometry of the absorber loaded PIFA antenna (a) top view of the substrate, (b) bottom view (c) side view (d) front view (e) 3D view $L_g = 20$, $W_g = 10$, $Y_1 = 1, Y_2 = 2, n = 0.5, X_3 = 1, m = 1.5$, units in mm).

5.3.1 Evolution of the Absorber Loaded Slotted PIFA Antenna

Figure 5.4 and Figure 5.5 demonstrate how the absorber loaded slotted PIFA antenna was designed from the slotted PIFA antenna to obtained miniaturization and wideband operation. The Ant1 starts with a narrow shorting plate where SH_1 connects the top radiator's narrow strip to the ground plane. The distance between the feed and the shorting plate determines the antenna's impedance bandwidth of 4.31 GHz, which covers the 26.31-30.63 GHz band. The antenna's impedance was determined to be Z = 66.4+j3.3.

SH_1 is removed for better impedance matching, and SH_2 is shorted to the broad side of the patch with a wide-width shorting plate. The bandwidth of 4.67 GHz is achieved because of the wide-width shorting plate. The Ant2's impedance is Z = 54.7-j7.9. Two shorting plates are shorted at both ends of the patch to the ground after two steps of the antenna evolution. Ant3 has a 53.9-j10.4 antenna impedance and a 3.48 GHz operational bandwidth, which covers the 27.22-30.7 GHz band. The final design, Ant4, evolved which resonates at 27.3 GHz, and covering an 18.22-33.22 GHz band with a 15 GHz bandwidth. The proposed Ant4 has an impedance of Z = 56.6+j3.4 and maintains $S_{11} \leq -10$ dB impedance matching throughout the band.

(a)   Ant1   (b) Ant2

| (c)   Ant3 | (d) Ant4 |
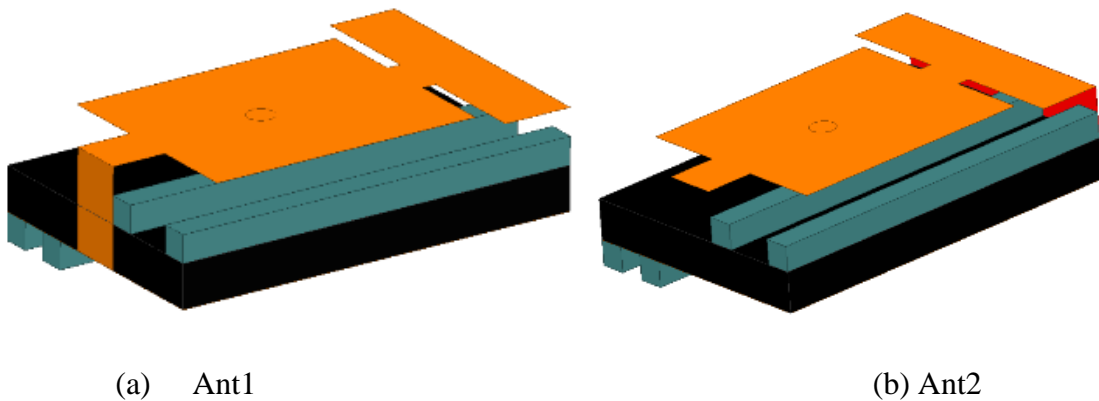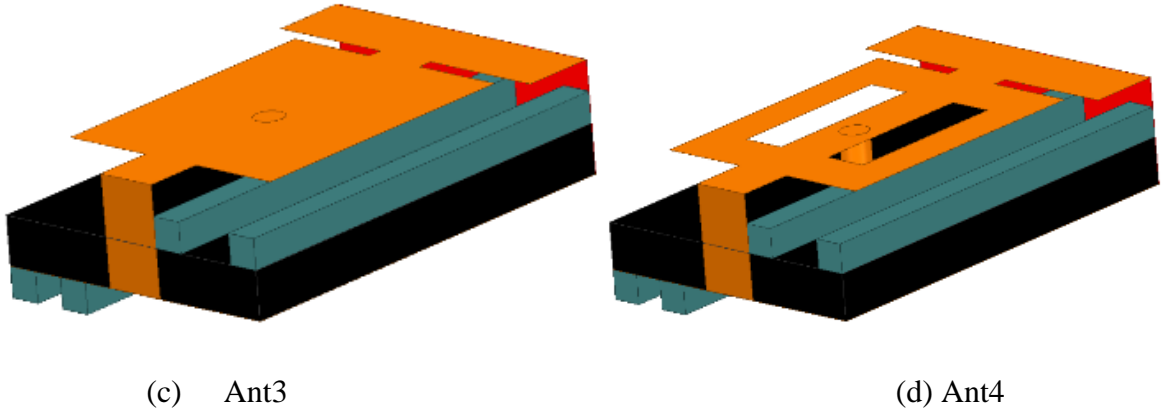
Figure 5.4: Evolutions of the proposed absorber-loaded slotted PIFA antenna.
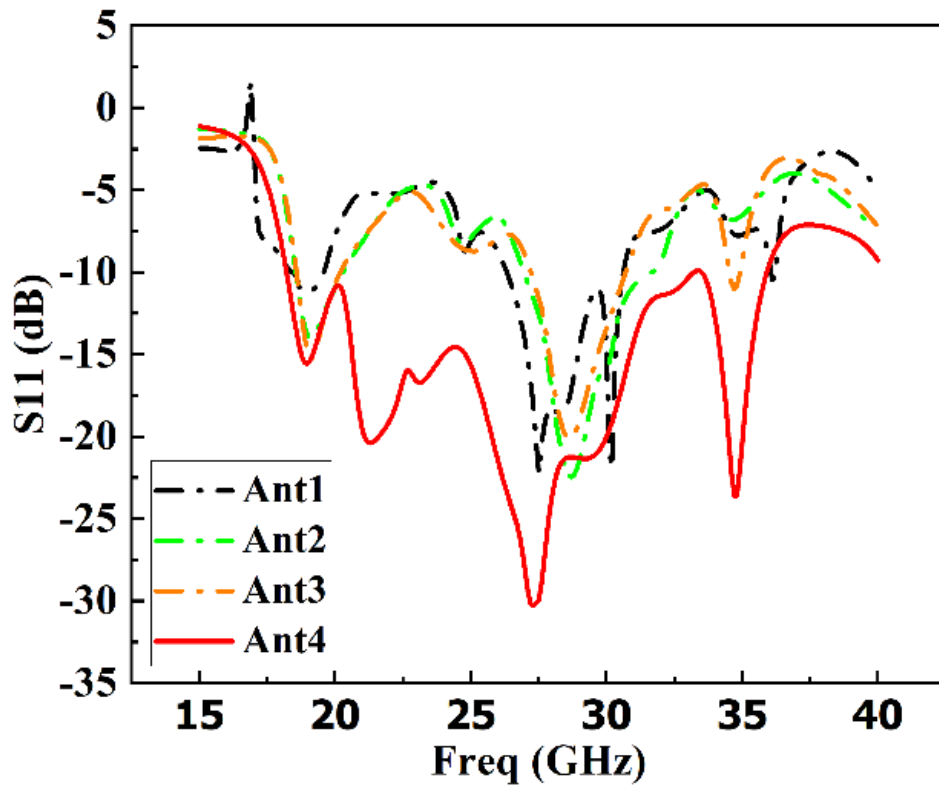
Figure 5.5: S-parameters of evolved proposed absorber-loaded slotted PIFA antenna.

5.4   Parametric Analysis of the Absorber Loaded Slotted PIFA Antenna

A parametric analysis is used to investigate the impact of parameter modification on the antenna's performance. The high-frequency structure simulator is used to do the antenna's parametric analysis (HFSS).

The slot length is changed from 5 to 7 mm, but the other parameters X_1, X_2, X_3, X_4, L_P, W_P, S_1, S_2, t, W, F_1, F_2, n, m, Y_1, Y_2, g_1, g_2 are kept unchanged. Figure 5.6 (a) demonstrates that increasing the slot length reduces the return loss at various frequencies and increases the overall impedance bandwidth. The slot length of 6 mm is thought to be acceptable for the structure that provides the requisite wideband.

The width of the both slots, W_s, is also altered at discrete values of 1.1 mm, 1.5 mm, and 1.9 mm, while the rest of the parameters remain fixed. As demonstrated in Figure 5.6, the 1.5 mm slot's width gives the widest bandwidth when compared to the other width of the slots (b). The lengths of both stubs S_1, S_2 affect the antenna's impedance, which is not depicted here for simplicity.

(a)   (b)
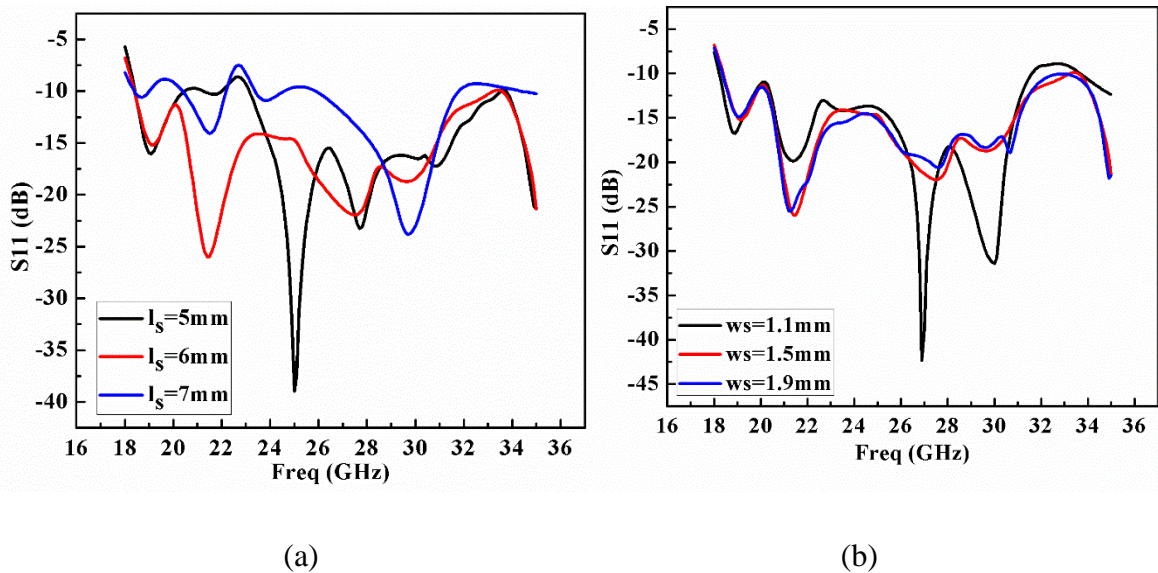
Figure 5.6: Parametric analysis of the proposed antenna (a) slot length and, (b) slot width.

5.5   Simulated and Measured Results

Figure 5.7 shows a photograph of the fabricated proposed antenna. Simulated and measured results are used to demonstrate the antenna's performance. The S-parameter comparison of the traditional PIFA and the Eccosorb MCS absorber-loaded PIFA is shown in Figure 5.8. The slotted PIFA antenna, without an absorber, covers a frequency range of 24.88 to 26.39 GHz and has a bandwidth of 5.89 %. The bandwidth of the proposed antenna is enhanced by 57.8% after loading the absorber in the slotted PIFA antenna. The absorber-loaded PIFA antenna covers a frequency band of 18.22 to 33.22 GHz, which resonates at 27.3 GHz, and

the performance of the reflection coefficient is increased. Figure 5.9 depicts the proposed antenna's simulated and measured S-parameter plot. The proposed antenna's measured bandwidth is 42 %, covering 19.7 to 30.32 GHz, respectively.

Figure 5.7: Fabricated absorber-loaded slotted PIFA antenna.
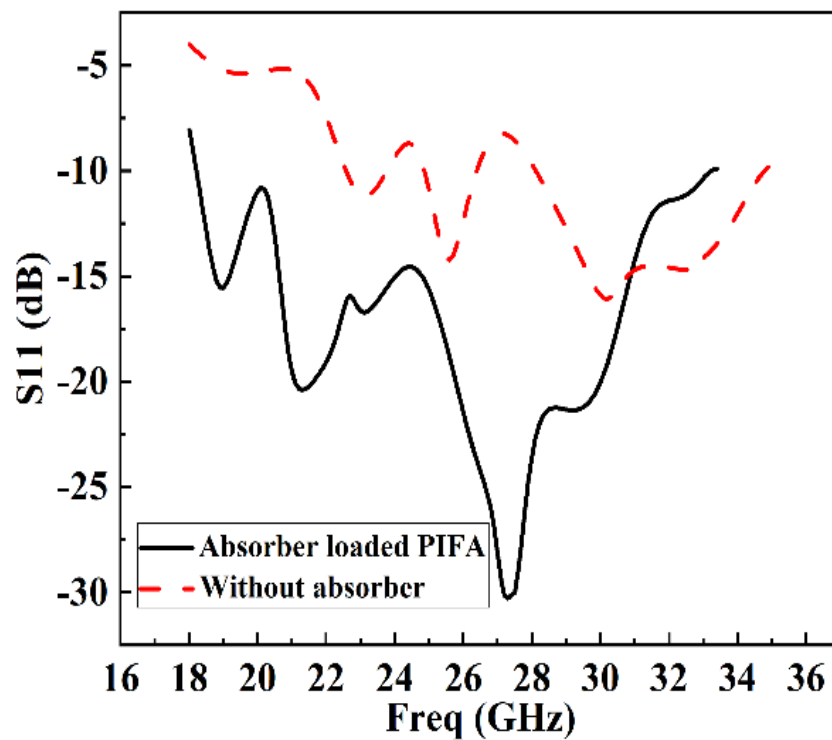
Figure 5.8: Simulated S-parameter of the PIFA antenna.
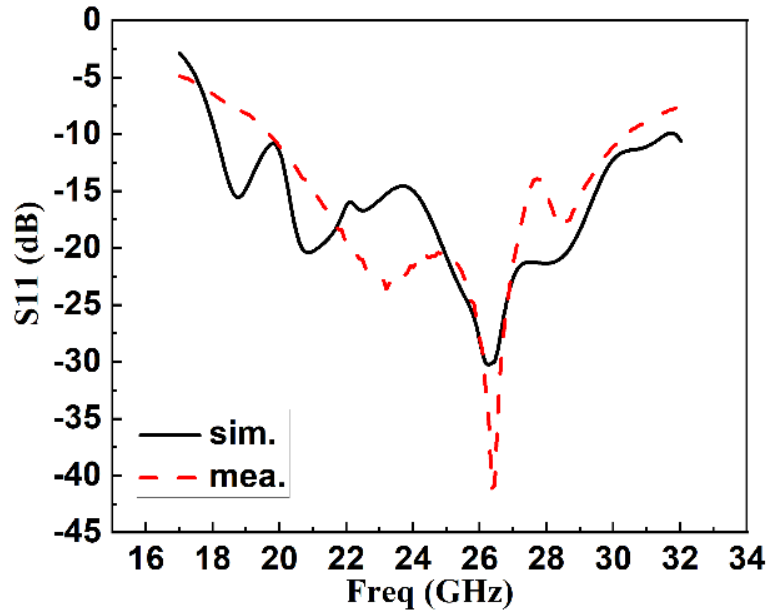
Figure 5.9: Simulated and measured S-parameter of the proposed absorber loaded slotted PIFA antenna.

Figure 5.10 shows the slotted PIFA's simulated 3D radiation patterns with and without the absorber at 27.3 GHz. The deep null in the boresight direction is observed in slotted PIFA antennas without absorbers; however, absorber loading eradicated the null, and the antenna achieves maximum radiation in the boresight direction. Radiation patterns are shown in 2D in Figure 5.11 for easier understanding, and it can be observed that the measured and simulated patterns are very similar.

(a)   (b)
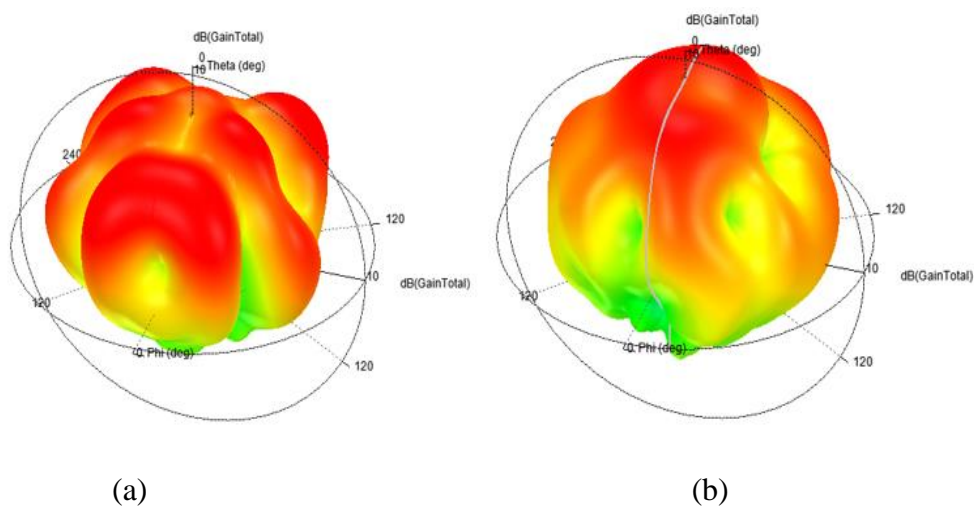
Figure 5.10: 3D radiation pattern of the antenna (a) without absorber (b) with absorber at 27.3 GHz.
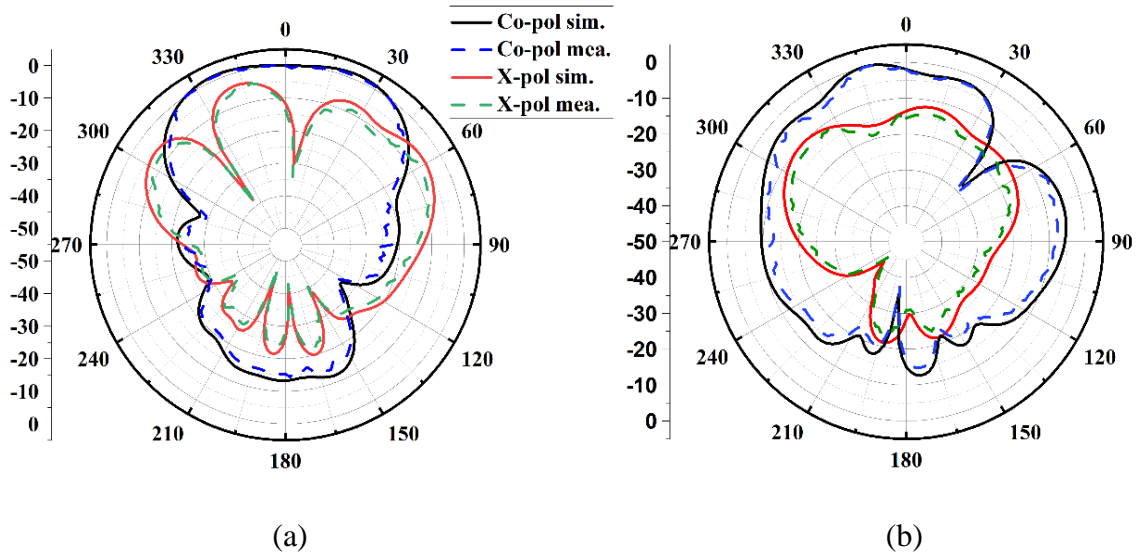
Figure 5.11: Simulated and measured radiation patterns of the proposed absorber loaded slotted PIFA antenna at 27.3 GHz (a) E-plane (b) H-plane

The antenna's realized gain is depicted in Figure 5.12. When an absorber is placed near the PIFA antenna, we can see that the gain increases. It is also clear that the absorber loading provides gain across the antenna's whole bandwidth. At 27.3 GHz, the absorber-loaded PIFA antenna has a gain of 7.3 dBi. The gain's simulated and measured values are very similar.
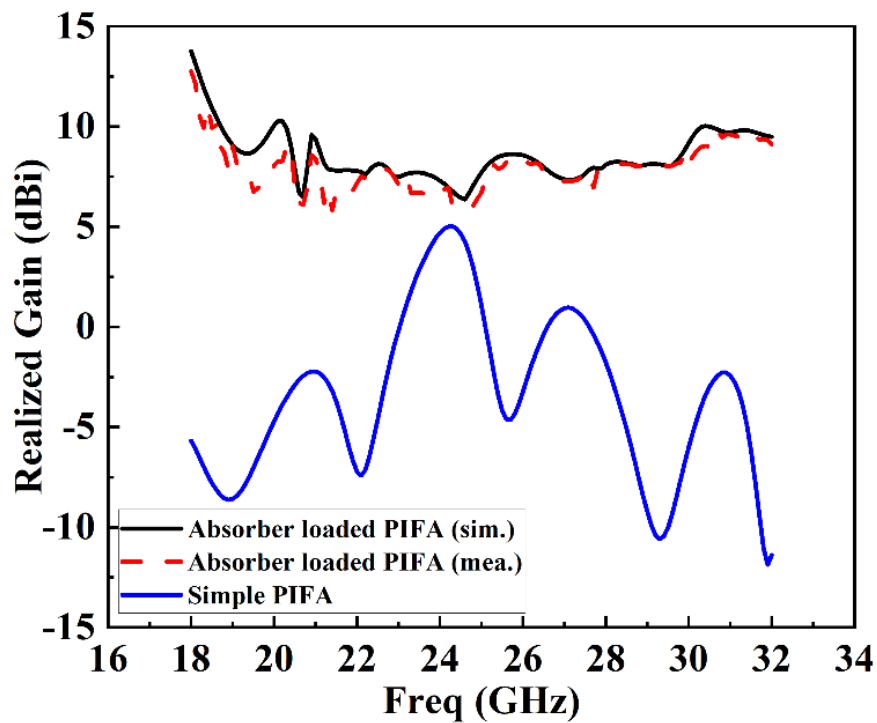
Figure 5.12: Realized gain of the proposed antenna.

The surface current on the antenna element is shown in Figure 5.13 (a). In the patch antenna, there are two slots. The current on the surface around the slots is symmetric without the absorber. When the absorber is positioned near one of the slots, the symmetry is broken since one of the slots is closer to the absorber than the other. As illustrated in Figure 5.13 (b), this change in symmetry results in a new distribution of surface current that is different from when the absorber is not loaded.

The position of the absorber also produces surface current near the feed point, which generates new far field components. Figure 5.10 shows how the new surface current distributions change the far-field pattern, which is different from the original, without the absorber-loaded antenna. In the presence of an absorber, the maximum current density on the radiator is 81.3 A/m, while it is 65.2 A/m when the absorber is removed.

| (a) | (b) |
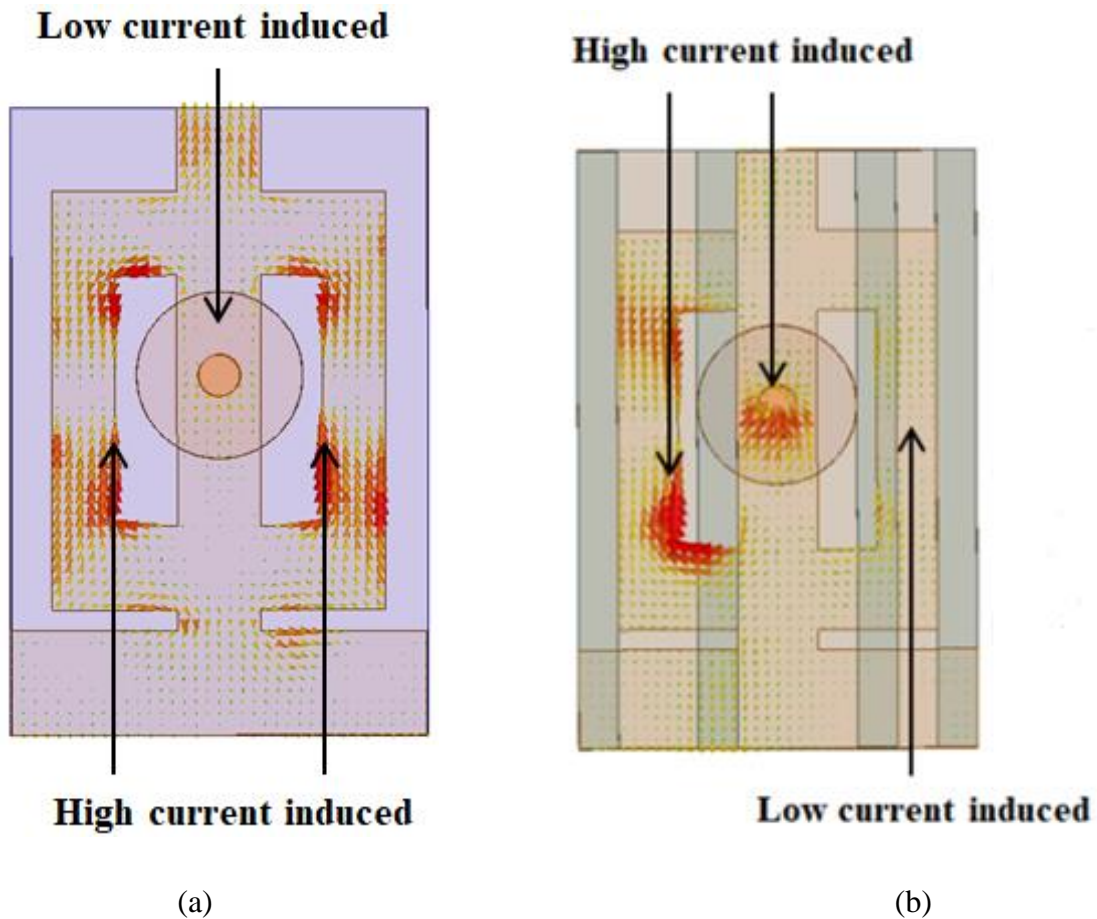
Figure 5.13: Surface current distribution of the proposed antenna (a) without absorber (b) with absorber

5.6   Observations and Comparisons of Proposed Antenna with Existing Design

This section explores the antenna performances of the proposed antenna and compares it with other published work based on the radiation pattern transformation, high gain, and wide bandwidth techniques. Table 5.1 shows the relative comparison among the related reference antennas which have been published in the literature [99-112] and proposed antenna performance. Most of the researchers were used phased array, MIMO, parasitic patches, SIW, stacking of substrate, more than one element to achieve radiation pattern transformation, high gain, and wide bandwidth but it increases size, complex fabrication, and cost.

The performance of the proposed designed antenna has been discussed in this section. In Table 5.1, all existing designs are compared with the current work. The antennas in the literature were decided based on comparable size, frequency of operation, method of operation, and comparable antenna output parameters. It is evident from Table 5.1 that the proposed antenna gives a good performance with a compact design.

Table 5.1 Comparison of present work with the previously published antennas

Ref.	Freq. Band (GHz)	Bandwidth (GHz)	Size (mm^3)	Gain (dBi)	Efficiency (%)	Number of Elements
[99]	37	0.6	-	10.8	-	4
[100]	21.5	1	$110 \times 55 \times 4.5$ $11.5\lambda_o \times 5.7\lambda_o \times 0.47\lambda_o$	12.5	95	8
[101]	24	few MHz	$3.78 \times 5.66 \times 77$ $0.44\lambda_o \times 0.67\lambda_o \times 9.1\lambda_o$	7	-	1
[102]	28	0.6-0.8	$1.3 \times 1.836 \times 0.381$	6.2	-	6

	38	0.3-0.38	$0.12\lambda_o \times 0.17\lambda_o \times .035\lambda_o$	6.8		
[103]	28	27.57-30.75	$4 \times 4 \times 1.34$ $0.56\lambda_o \times 0.56\lambda_o \times 0.18\lambda_o$	8.8	97.9-98.9	1
[104]	60/70	53-71	$14.4 \times 14.4 \times 1$ $6.8\lambda_o \times 6.8\lambda_o \times 0.47\lambda_o$	17.5	85	16
[105]	28	26.9-29	$30 \times 19.9 \times 0.79$ $4.2\lambda_o \times 2.7\lambda_o \times 0.11\lambda_o$	7.4	-	1
[106]	28/38	$27.575 - 28.425$	$6.8 \times 6.8 \times 0.254$ $0.94\lambda_0 \times 0.94\lambda_0 \times .035\lambda_0$	4	84 91	1
[107]	38	$34.1 - 38.9$	$15.6 \times 13 \times 0.254$ $3.4\lambda_0 \times 2.8\lambda_0 \times 0.05\lambda_0$	3.76	66.8	1
[108]	14.4/16.1	-	$41 \times 40 \times 3.2$ $2.9\lambda_0 \times 2.8\lambda_0 \times 0.02\lambda_0$	11.3 8.7	-	1
[109]	17	$16 - 18$	-	11.6	85	1
[110]	3	$2.68 - 3.65$	$66 \times 66 \times 5.77$ $1.32\lambda_0 \times 1.32\lambda_0 \times 0.12\lambda_0$	7.21	-	1
[111]	5.2	$4.69 - 5.7$	$9 \times 8 \times 4.5$ $0.25\lambda_0 \times 0.23\lambda_0 \times 0.13\lambda_0$	7.8	96.2	1
[112]	28/38	$26.65 - 29.2$ $36.95 - 39.05$	$14 \times 12 \times 0.38$ $1.94\lambda_0 \times 1.6\lambda_0 \times 0.05\lambda_0$ $13.6\lambda_0 \times 13.6\lambda_0 \times 0.16\lambda_0$	1.27	78 76	2

				1.8 3		
This work	**26.36**	**19.7 – 30.32**	**10 × 8 × 3.6** **3.4λ₀ × 2.7λ₀ × 1.2λ₀**	7.3	94	1

5.7 Conclusion

In this chapter, Eccosorb MCS absorber is loaded in slotted PIFA antenna to obtained pattern transformation, high gain, and wide bandwidth of 57.8 % (simulated), 42 % (measured), which covers 19.7 to 30.32 GHz respectively. The proposed design is comprised of absorbers, with two strips of absorbers positioned above the substrate and the other two strips placed below the substrate. The null existing in the boresight direction in conventional PIFA is removed with the help of the absorbers, and additional radiation is generated in the boresight direction. When compared to a PIFA antenna without an absorber, the proposed absorber-loaded PIFA antenna is 46.6 % smaller. Overall, the proposed antenna has good radiation properties and is a promising choice for millimeter wave applications.

CHAPTER 6

Beam Splitting Planar Inverted-F Antenna for 5G Communication

---

6.1   Introduction

Extending the work performed in the fifth chapter, a planar inverted-F multi-beam antenna using RF absorbers is addressed here. The mm-wave ranging from $1-10$ mm wavelength ($10-100\,\text{GHz}$) has many limitations. The tiny wavelength wave is affected by raindrops, oxygen absorption, and line of sight during its propagation. The beamforming, beam splitting, and directive antennas are the key solutions to overcome the problems raised at mm-waves. In this regard, the multibeam antenna offers independent beams in which the selected beams reduce the interference and provide greater coverage in desired the direction which is the compulsory requirement of $5\,\text{G}$ [83]-[84].

The multi-beam antennas mostly require a complex system of multiple antennas such as a phased array or MIMO antennas and make the system bulky as well as power-hungry. The proposed antenna circumvents these limitations and provides multiple beams from a single antenna with wide angular coverage.

In this chapter, the split beam has been explored using an RF absorber (Eccosorb MCS).

In literature, various structures have been proposed to achieve split beams. Beam steering capability ranges from -90° to $+90^{o}$ in theta plane with a switchable 3D coverage phased array antenna is presented [113]. The digital metasurface along with a lens is used to split the beam in [115]. The dual beams are formed through three pairs of metamaterials (MTM) arrays which make the antenna system large and costly [117].

In this chapter, we explored a split-beam technique of the slotted planar inverted-F antenna (PIFA) using an Eccosorb MCS absorber. Figure 6.1 gives the designed methodology of the presented antenna in this chapter.
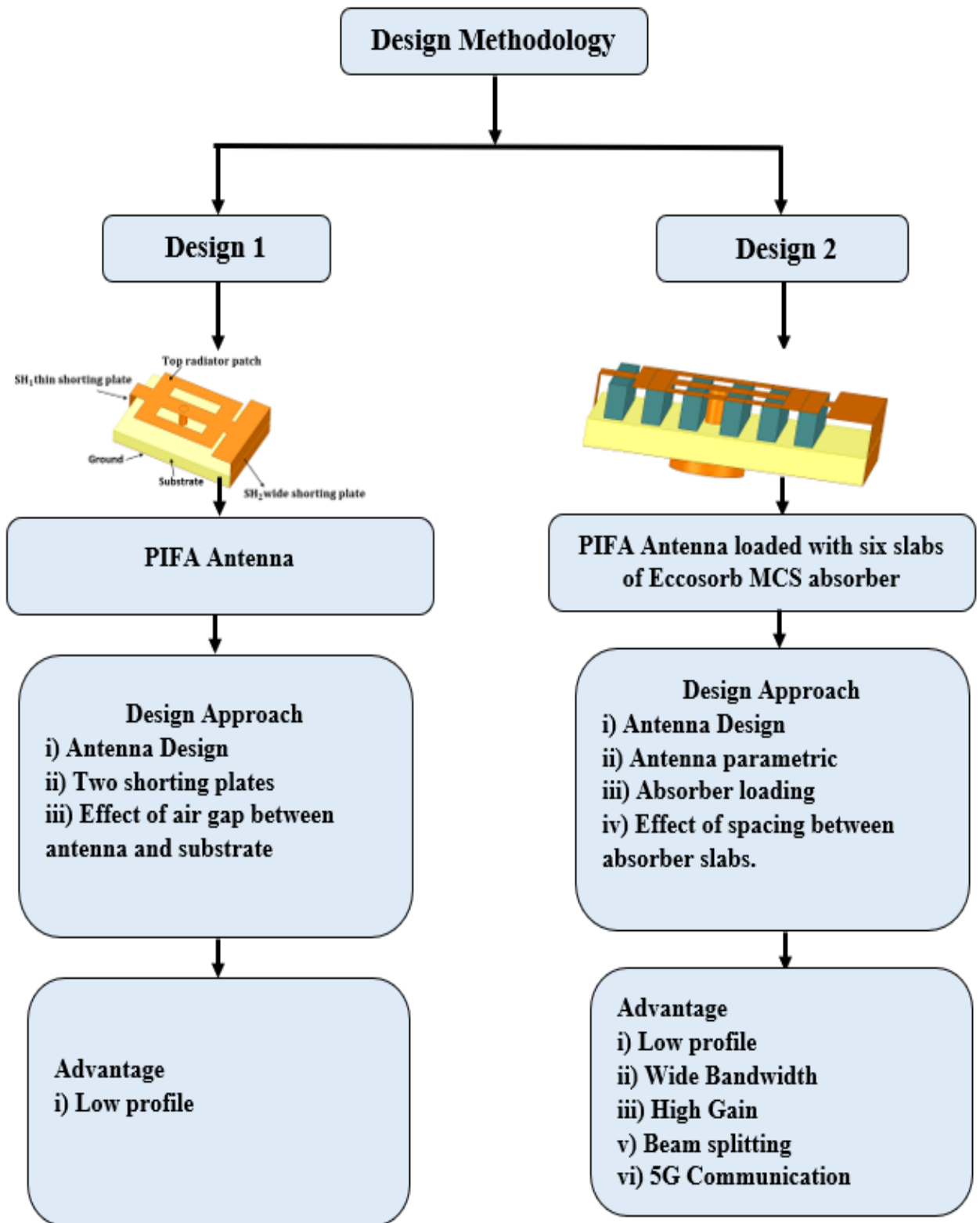
Figure 6.1: Designed methodology of the chapter-6 antenna.

6.2   Design of Slotted PIFA Antenna

The configuration of the proposed slotted planar inverted-F antenna is shown in Figure 6.1. The antenna has been designed on 1.6 mm thick RT/Duroid substrate, with the dimensions of $20\text{mm} \times 10\text{mm}$ and the dimensions of the patch are $0.90\lambda_o \times 0.72\lambda_o \times 0.32\lambda_o$ where λ_o is 12.24 mm for frequency of 24.5 GHz. The employed laminate has relative permittivity (ε_r) of 2.2 and a dielectric loss tangent $(\tan\delta)$ of 0.0009. The thickness of the copper patch is 0.035 mm. The air gap between the patch and the substrate is $0.18\lambda_o$. The shorting plate $SH_1(2\text{mm})$ and $SH_1(10\text{mm})$ are soldered to both ends of the radiator to the ground at distances of F_1 and F_2 from the feed position. The distance between both shorting plates and feed helps to maintain the impedance of the antenna. The top copper radiator is fed by an 2.92 mm N-type connector. As shown in Fig. 1 (a), two slots $(l_s \times W_s)$ are etched on the radiator, and there are also two stubs S_1, S_2 $(0.27\lambda_o \times 0.045\lambda_o)$ to maintain the impedance bandwidth and the S-parameter.

The design equations of the PIFA antenna define dimensions as:

$$L_p + W_p - W_{SH_1} - W_{SH_2} = \lambda/4 \tag{6.1}$$

$$f_o = \frac{c}{4(L_p + W_p - W_{SH_1} - W_{SH_2})} \tag{6.2}$$

where L_p, W_p are the length and width of the top patch and W_{SH_1}, W_{SH_2} are the width of the narrow and broad shorting plate, respectively. Also, c is the speed of light and λ is the wavelength of the desired resonant frequency (24.5 GHz).

(a)   (b)

(c)
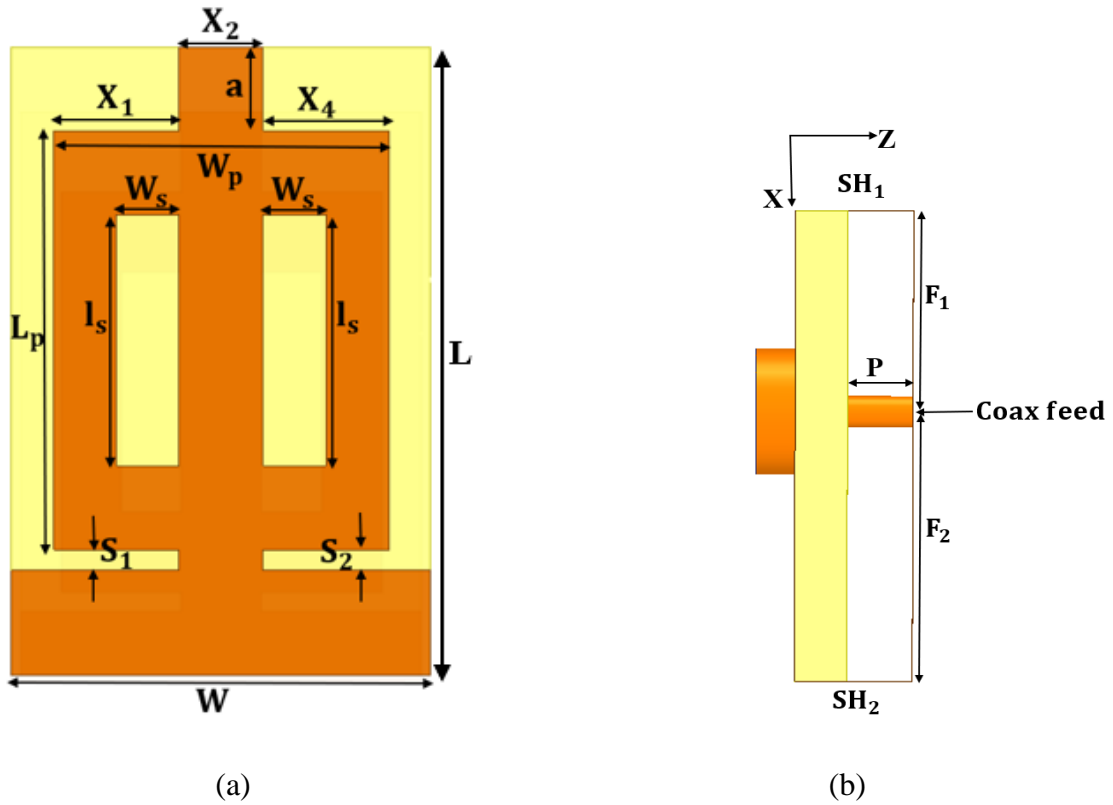
Figure 6.2: Geometry of the proposed slotted PIFA antenna (a) top view of the slotted patch; (b) side view; (c) 3D view of the antenna.

The optimized parameters of the proposed antenna are shown in Figure 6.2 are $L_p = 0.90\lambda_o$, $W_p = 0.72\lambda_o$, $W = 10mm$, $X_1 = 3mm$, $X_2 = 2mm$, $a = 2mm$, $X_4 = 3mm$, $W_s = 1.5mm$, $l_s = 6mm$, $t = 2.5mm$, $F_1 = 6.4mm$, $F_1 = 8.6mm$, $L = 20mm$, respectively.

6.3   Design of Beam Splitting Slotted PIFA Antenna

The split beam absorber loaded PIFA antenna configuration is shown in Figure 6.3. The Eccosorb MCS absorber from Laird Technologies, Inc. has high permittivity, ε_r of 15 which reduces the overall voltage standing wave ratio (VSWR). This material is designed for the suppression of surface currents over a wide range of frequencies. In MIMO configuration, this material plays a very good role to reduce the RF coupling. The conventional normal RF absorbers do not have a good response at high frequency. So, for high frequency, high-performance absorbers are needed and the Eccosorb MCS serves the purpose. Eccosorb absorber is a highly lossy, flexible, nonconductive broadband silicone absorber. In the antenna structure, six strips of the Eccosorb MCS absorber are placed periodically between the substrate and radiator. The bottom part of the absorber is touched to the surface of the substrate and the upper part of the absorber is touches the radiator. The separation distance between all absorbers is 1 mm, denoted by 's', which plays a significant role in achieving split beams and the height of the absorber is denoted by 'h_b'. The width of the absorber is denoted by 'g' and the gap 'g_1' is in between the narrow shorting plate and absorber. The gap between the wide-width shorting plate and the absorber is 'g_2'. The overall size of the beam splitting antenna is $3.2\lambda_o \times 2.5\lambda_o \times 1.2\lambda_o$.

(a)   (b)
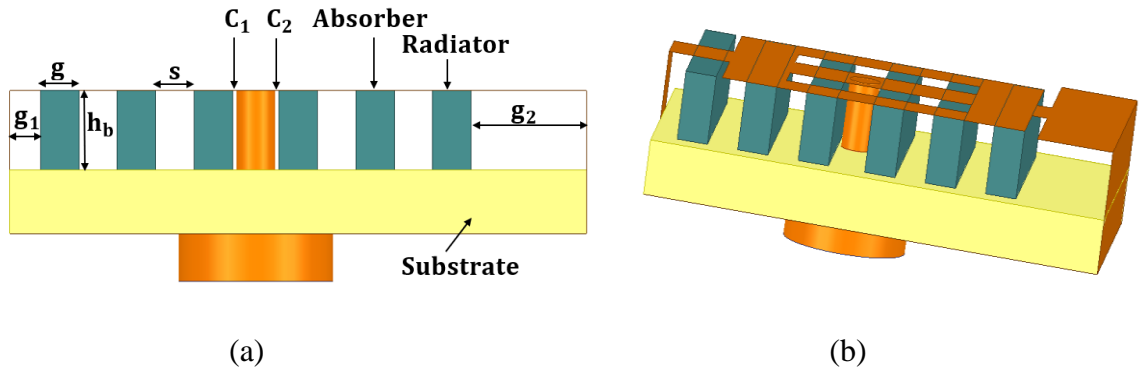
Figure 6.3: Geometry of the proposed beam splitting antenna (a) side view; (b) 3D view
$g_1 = 0.8$, $g = 1$, $h_b = 2$, $C_1 = C_2 = 0.1$, $g_2 = 3$, (units in mm).

6.3.1 Parametric Analysis of Beam Splitting Slotted PIFA Antenna

The parametric analysis performed on the gap 's' between the absorbers of the antenna is shown in Figure 6.4. The value of 's' is increased from $0.7mm$ to $1.3mm$ with a step size of 0.3 mm. It can be seen that the optimized value of 's' is $1mm$ which gives good S-parameter and bandwidth. The parametric analysis is carried out with high -frequency structure simulator (HFSS) software.
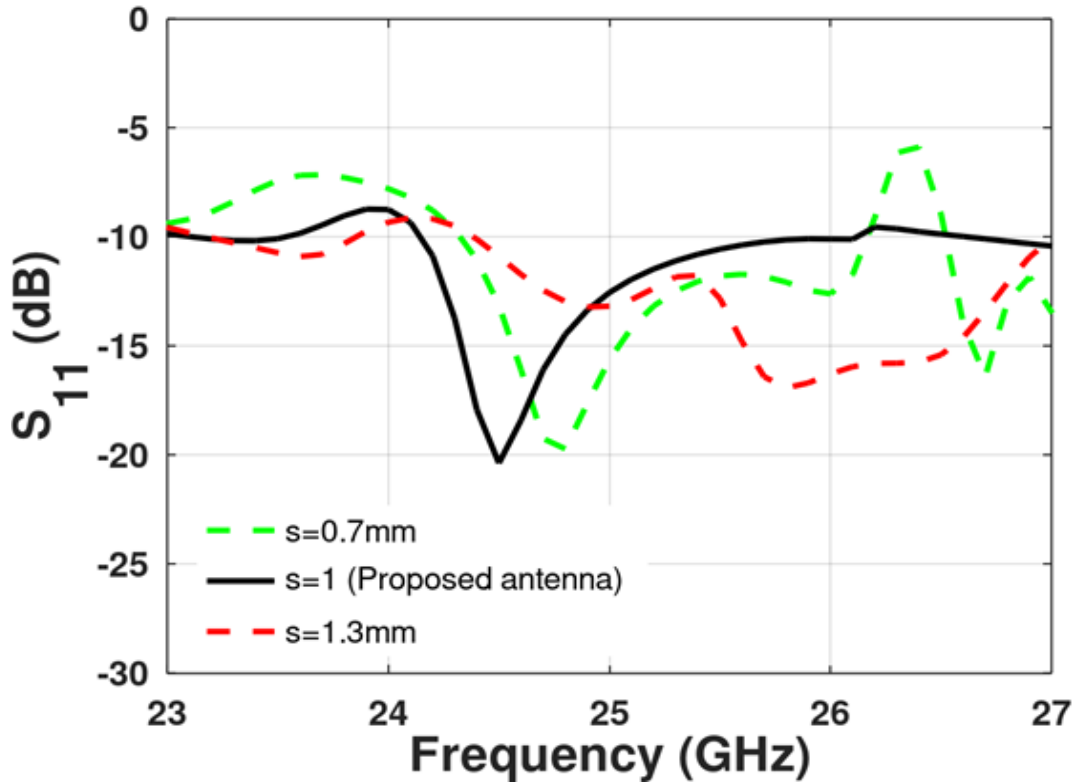
Figure 6.4: Parametric analysis of the proposed antenna.

6.4 Beam Splitting Technique

In this section, to get a better understanding of the beam splitting behaviour of the antenna, numerical equations are derived and are discussed below. When the absorber is embedded periodically in between the patch and substrate with equal distance, the size of the antenna is reduced in accordance with the decreased wavelength as:

$$\lambda_g = \frac{c}{f\sqrt{\varepsilon_r}} = 3.16mm \qquad (6.3)$$
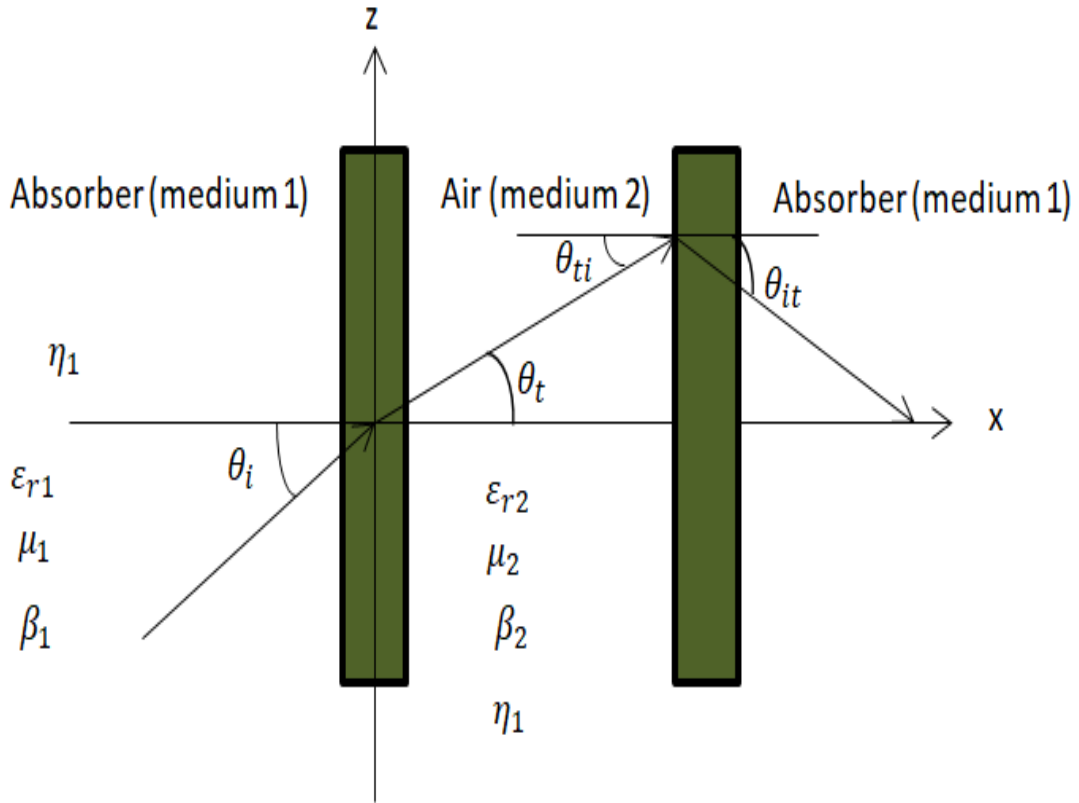
Figure 6.5: Propagation of electric fields through different media.

whereas,

$$\varepsilon_{r1} = 15, \mu_1 = 1, \varepsilon_{r2} = 1, \mu_2 = 1 \tag{6.4}$$

For $\theta_t = 26^o$, θ_{ti} is found to be 6.48^o as shown in Figure 6.5.

Figure 6.6 (a) and Figure 6.6 (b) show that the two cases of the propagation are obtained:

Case (i) oblique incidence and reflection of a plane wave.

Case (ii) for parallel polarization.

Oblique incidence and reflection of a plane wave as shown in Figure 6.6.

Absorber (medium 1)   Air (medium 2)
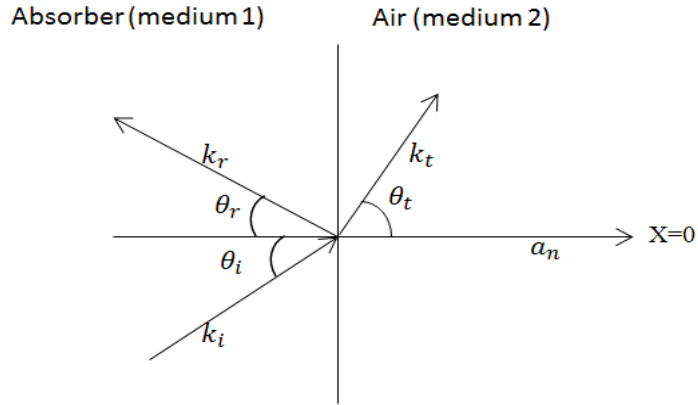
(a)

where a_n is the plane of incidence, θ_i is the angle of incidence between k and a_n. As shown in Figure 6.6 (a), it seems that incident and reflected waves are in medium 1 and transmitted or refracted wave is in medium 2.

The incident electric field is given as

$$E_{i1} = E_o e^{-\alpha z} \cos(\omega t - \beta_1 z + \theta_i + 180^o) \tag{6.5}$$

In eq. 6.3, 180° phase shift is added because the electric field is incident from dense media to rare media.

The reflected wave is given by,

$$E_{r1} = \Gamma E_{i1}$$

$$E_i = \Gamma E_o e^{-\alpha z} \cos(\omega t - \beta_1 z + \theta_i + 180^o) \tag{6.6}$$

where $\theta_i = 6.48^o, \beta_1 = 0.13, z = 0.001m$

$$E_{i1} = E_o e^{-0.001\alpha} \cos(\omega t - 186.4^o) \tag{6.7}$$

The reflected electric field is calculated with the help of the relation given below,

$$E_{r1} = \Gamma E_i$$

where Γ is the reflection coefficient which is computed using

$$\Gamma = \frac{\sqrt{\varepsilon_{r1}} - \sqrt{\varepsilon_{r2}}}{\sqrt{\varepsilon_{r1}} + \sqrt{\varepsilon_{r2}}} = 0.589 \tag{6.8}$$

and

$$E_{r1} = \Gamma E_{i1}$$

$$E_{r1} = 0.589(E_o e^{-0.001\alpha} \cos\cos(\omega t - 186.4^o) \tag{6.9}$$

The transmitted electric field is given as

$$E_{t1} = E_{to} e^{-\alpha z} \cos(\omega t - \beta_2 z + \theta_t + 180^o) \tag{6.10}$$

Here, $z = 0.002m, \beta_2 = 0.152, \theta_t = 26^o$

$$E_{t1} = E_{to} e^{-0.002\alpha} \cos(\omega t - 205.9^o) \tag{6.11}$$

$$E_{i2} = E_o e^{-0.002\alpha} \cos\cos(\omega t + 6.47^o) \tag{6.12}$$

When the wave propagates from medium 2 (air) to medium 1 (absorber),

$$\theta_i = \theta_t = 6.48^o, z = 0.001m \tag{6.13}$$

$$E_{i2} = E_{t1} \tag{6.14}$$

$$E_{r2} = \Gamma' E_{i2} \tag{6.15}$$

where,

$$\Gamma' = \frac{\sqrt{\varepsilon_{r2}} - \sqrt{\varepsilon_{r1}}}{\sqrt{\varepsilon_{r2}} + \sqrt{\varepsilon_{r1}}} = -0.589 \tag{6.16}$$

$$E_{r2} = -0.589 E_o e^{-0.001\alpha} \cos(\omega t + 25.9^o) \tag{6.17}$$

$$E_{t2} = E_{to} e^{-\alpha z} \cos(\omega t - \beta_2 z' + \theta_t'') \tag{6.18}$$

Here, $z' = 0.002m, \theta_t'' = 6.48^o$

$$E_{t2} = E_{to}e^{-0.002\alpha}\cos(\omega t + 6.47^o) \qquad (6.19)$$

The total incident wave is given as

$$E_i = E_{i1} + E_{i2} \qquad (6.20)$$

$$E_i = E_o e^{-0.001\alpha}(\omega t - 186.4^o) + E_o e^{-0.002\alpha}$$

The total transmitted wave is given as

$$E_t = E_{t1} + E_{t2} \qquad (6.21)$$

$$E_t = E_{to}e^{e-0.002\alpha}\cos\cos(\omega t - 205.9^o) + E_{to}e^{-0.002\alpha}\cos(\omega t + 6.47^o)$$

The total reflected wave is given as

$$E_r = E_{r1} + E_{r2} \qquad (6.22)$$

$$E_r = 0.589[E_o e^{-0.001\alpha}\cos\cos(\omega t - 186.4^o] - 0.589E_o e^{-0.001\alpha}\cos(\omega t + 25.9^o) \qquad (6.23)$$

Figure 6.6 (b) depicts the parallel polarization of electromagnetic waves.
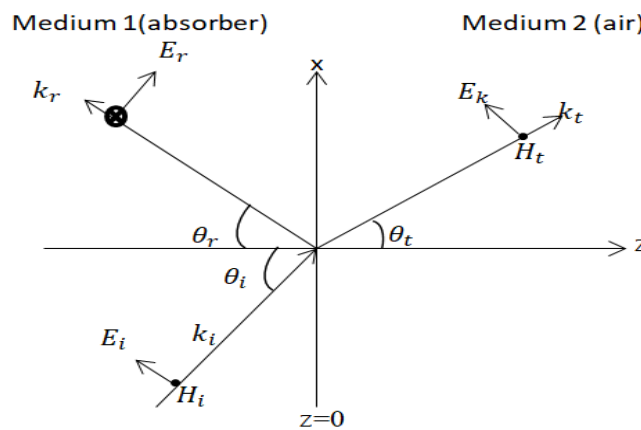
(b)

Figure 6.6: (a) Plane wave incident and reflection, (b) Parallel polarization of electromagnetic waves.

where $\theta_i = 6.48^o, \theta_t = 26^o, \beta_1 = 0.13, \beta_2 = 0.512$

$\eta_1 = 97\Omega, \eta_1 = 377\Omega, x = 0.002m, z = 0.001m$

$$E_{is} = E_{io}(a_x - 0.112a_z)e^{-0.000289j} \tag{6.24}$$

$$H_{is} = \frac{E_{io}}{\eta_1}e^{-j\beta_1(x\sin\theta_i + z\cos\theta_i)}a_y \tag{6.25}$$

$$H_{is} = 0.01E_{io}e^{-0.000289}a_z \tag{6.26}$$

$$E_{rs} = E_{ro}(\cos\theta_r a_x + \sin\theta_r a_z)e^{-j\beta_1(x\sin\theta_r - z\cos\theta_r)} \tag{6.27}$$

$$E_{rs} = E_{ro}(a_x + 0.112a_z)e^{9.88\times10^{-5}j} \tag{6.28}$$

The transmitted electric field in medium 2 (air) is given by

$$E_{ts} = E_{to}(\cos\theta_t a_t - \sin\theta_t a_z)e^{-j\beta_2(x\sin\theta_t + z\cos\theta_t)} \tag{6.29}$$

where $\theta_t = 26^o, \beta_2 = 1, x = 0.002m, z = 0.002m$

$$E_{ts} = E_{to}(0.89a_x - 0.43a_z)e^{0.0025j}$$

(6.30)

$$H_{ts} = \frac{E_{ts}}{\eta_2}e^{-j\beta(x\sin\theta_t + z\cos\theta_t)}a_y \tag{6.31}$$

$$H_{ts} = 0.0026E_{to}e^{-0.0012j} \tag{6.32}$$

The parallel polarization reflection coefficient is given by

$$\Gamma_{11} = \frac{\eta_2\cos\theta_t - \eta_1\cos\theta_i}{\eta_2\cos\theta_t + \eta_1\cos\theta_i} = 0.47$$

(6.33)

$$E_{ro} = \Gamma_{11}E_{io} \tag{6.34}$$

$$E_{ro} = 0.47E_{io} \tag{6.35}$$

The expression for propagation constant for the parallel polarization is given as

$$\tau_{11} = \frac{E_{to}}{E_{io}} = \frac{2\eta_2 \cos\theta_i}{\eta_2 \cos\theta_t + \eta_1 \cos\theta_i} = 1.63 \qquad (6.36)$$

6.5 Simulated and Measured Results

The fabricated prototype of the proposed beam splitting slotted PIFA antenna is shown in Figure 6.7. The thickness of the absorber, the number of strips, and the gap between them are optimized as discussed earlier.

(a)   (b)
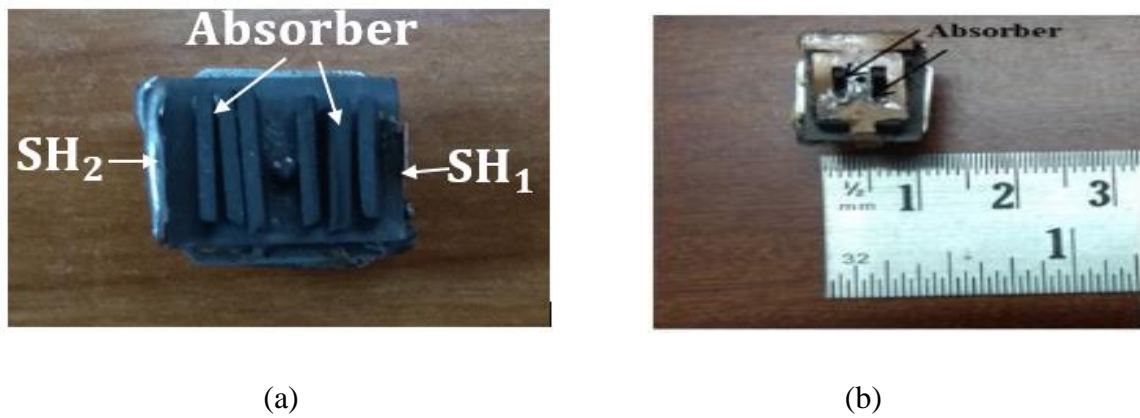
Figure 6.7: Fabricated beam splitting antenna (a) cross section (b) top view.

The electric field distribution of the patch which changes the direction and propagation of the field in the absorber is depicted in Figure 6.8. It can be seen that the electric field is diverted into two directions and the current path has also changed which gives the maximum radiation into two directions. However, in the middle of the patch near to the feed position, the current is very less, which gives a deep null in the boresight direction. The absorber produces constructive interference in two different directions giving rise to two split beams. The pair of vertically placed absorber slabs toward the wide shorting plate near the feed position have more electric fields in two different directions that produce the split beams at $\pm 26^o$.
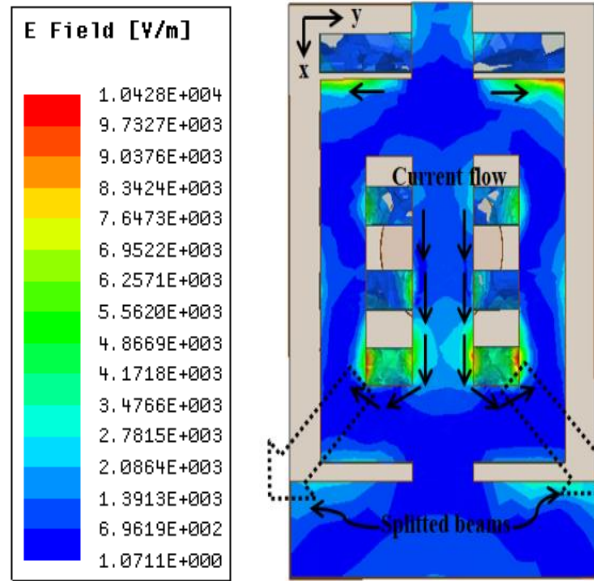
Figure 6.8: E-field distribution beneath the patch (in absorber) and surface current density on the radiator of beam splitting antenna at 24.5 GHz.

The reflection coefficient of the beam splitting antenna is measured by R & S ZNB 40 vector network analyzer. The measured and simulated S_{11} of the antenna are illustrated in Figure 6.9. The simulated S_{11} of the antenna has an impedance bandwidth of 8% in the frequency bands of $24.11 - 26.09$ GHz. It can be seen that the measured $S11 < -10$ dB in the frequency bands of $24.2 - 25.7$ GHz and has an impedance bandwidth of 6%.
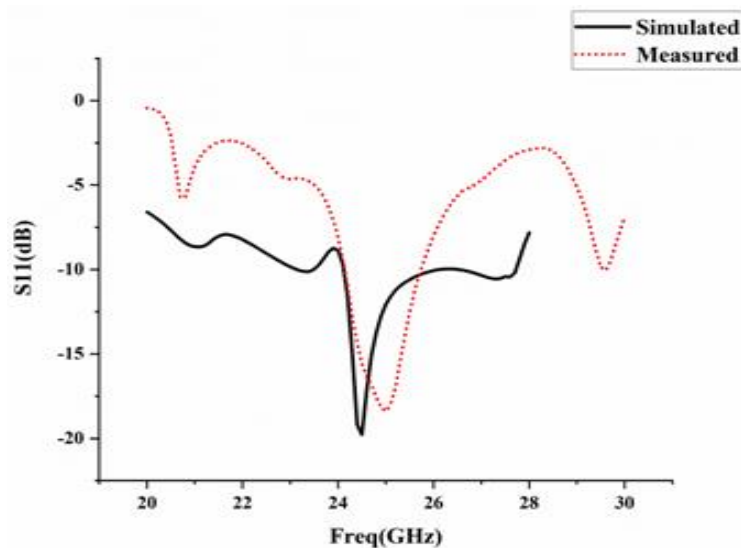
Figure 6.9: Simulated and measured S_{11} of the proposed beam splitting antenna.

The beam splitting antenna provides a peak gain of $10.3\,$dB at $24.5\,$GHz. Figure 6.10 shows good agreements between simulated and measured results for beam splitting antenna.
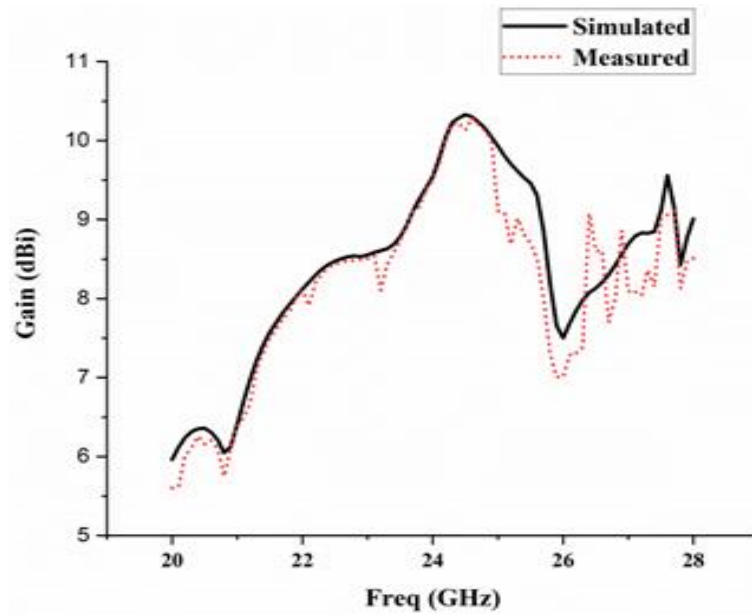
Figure 6.10: Gain of the proposed beam splitting antenna.

The simulated and measured co- and cross-polarization pattern of the proposed beam splitting antenna is depicted in Figure 6.11. A deep null is observed in the broadside direction and the maximum gain is obtained at $\pm26^{o}$. The half-power beamwidth (HPBW) of 28° and the first null beamwidth (FNBW) is found to be 52.82^{o}.
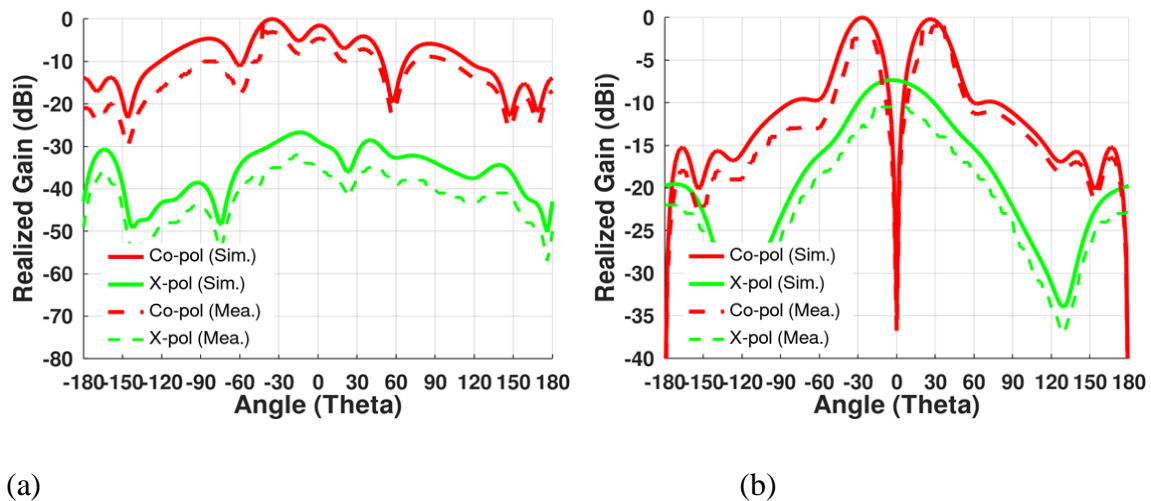
(a)   (b)

Figure 6.11: Simulated and measured radiation patterns at 24.5^{o} GHz. (a) φ= 0° cut (b) φ= 90° cut.

To get better insights, Figure 6.12 shows the 2D radiation patterns of the proposed antenna at different frequencies. It can be seen from Figure 6.12 that the antenna achieves beam splitting over the desired frequency band.
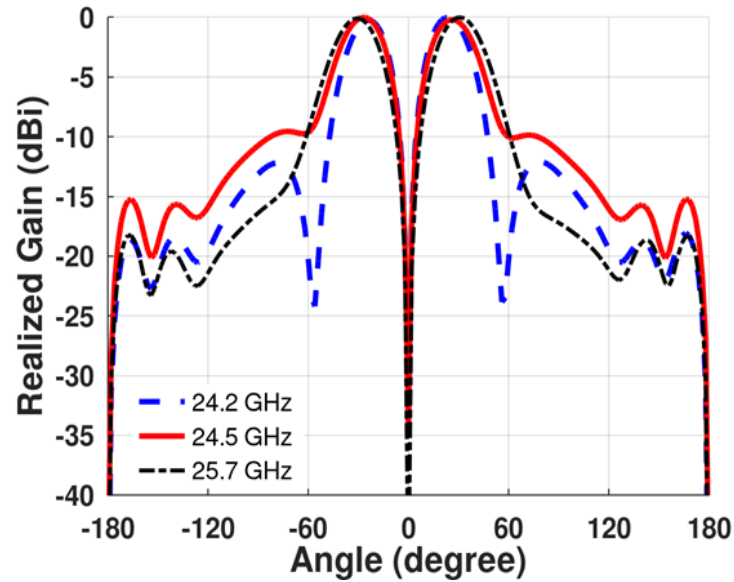
Figure 6.12: Beam splitting at different frequencies.

6.6 Observations and Comparisons of Proposed Antenna with Existing Design

In this section, the comparison between the presented antenna and its performances are compared with other published work. Table 6.1 shows the comparative comparison among the related reference antennas, which have been published in the literature [113-118], and presented antenna performance. The presented antenna gives the -10 dB impedance bandwidth, dual split beam with a single element, and good gain which are better compared to the published paper. It offers compact size with good gain throughout the band compared with existing structures.

Table 6.1 Comparison of present work with the previously published antennas

Ref.	Freq. Band (GHz)	Bandwidth (GHz)	Size (mm^3)	Gain (dBi)	Beam split	Number of Elements
[100]	21.5	1	110×55×4.5	12.5	yes	8

			$11.5\lambda_o \times 5.7\lambda_o \times 0.47\lambda_o$			
[105]	28	26.9-29	$30 \times 19.9 \times 0.79$ $4.2\lambda_o \times 2.76\lambda_o \times 0.11\lambda_o$	7.4	yes	1
[113]	11	10.42-11.22	$53.9 \times 53.9 \times 1.57$ $2.92\lambda_o \times 2.92\lambda_o \times 0.8\lambda_o$	18.6	yes	32
[114]	10	0.6	$256 \times 256 \times 3$ $13.6\lambda_o \times 13.6\lambda_o \times 0.16\lambda_o$ -		yes	multiple
[115]	26	$24.25 - 27.5$	$30 \times 30.5 \times 0.508$ $4\lambda_o \times 3.91\lambda_o \times 0.065\lambda_o$	7.4	yes	MIMO
[116]	5.5	$5.18 - 5.8$	$67 \times 74 \times 3.175$ $1.22\lambda_o \times 1.35\lambda_o \times 0.058\lambda_o$ &	7.92 at 35° & 5.94 at -33°	yes	1
This work	**24.5**	**24.2-26.1**	$\mathbf{10 \times 8 \times 3.6}$ $\mathbf{3.2\lambda_o \times 2.5\lambda_o \times 1.2\lambda_o}$	**10.07 at -2 & 10.3 at $+26^{\circ}$**	yes	1

6.7 Conclusions

This chapter discussed the designed and analysis of the dual split-beam slotted PIFA antenna based on the Eccosorb MCS absorber. PIFA antenna which achieves multi-beam behaviour by six slabs of absorbers placed periodically between the PIFA patch and substrate to split the beams into two directions at $\pm 26^o$.

The measured results show that the beam splitting antenna has realized a bandwidth of 6% which covers $24.2-25.7\,\mathrm{GHz}$ band with a maximum gain of 10.3 dBi respectively. With these characteristics, it can be concluded that the proposed antenna has better antenna performance compared to previously published works and can be a good candidate for 5G applications.

CHAPTER 7

Substrate Integrated Waveguide (SIW) Beamforming Antenna

7.1 Introduction

The different gain enhancement and beam scanning techniques have been addressed in the previous chapters and these techniques incorporate periodic structures like an artificial magnetic conductor (AMC), AMC with superstrates, metasurface, uniform superstrates, non-uniform superstrates, RF absorber (Eccosorb MCS). But, still, antennas for some applications need to have a wide scanning range with high gain and wide bandwidth, so the antenna can easily use for 5G communication. The substrate integrated waveguide (SIW) technology with metasurface and EBG (Electromagnetic bandgap) structure also provide beamforming with wide scanning. So, SIW technology can be an alternative option to fulfill the demands of the antenna designers and researchers.

The beamforming technology and scanning of the radiation pattern meet all 5G communication criteria [121]-[122]. The Rotman lens, Graded index lens, Hybrid reflector, Blass matrix, Hybrid lens, and Butler matrix are among the various beamforming structures reported in [123]. One of the most important aspects of beamforming antennas for 5G communication is the SIW. In addition to lowering sidelobe levels, it has low radiation loss, cross coupling, high gain, and outstanding radiation properties [124]-[125].

Peters *et al*. presented four beams SIW slotted antenna array with -20$^\text{o}$ to + 20$^\text{o}$ beam scanning using the slotted array [126].

In literature, mostly the research concentrates on the phased array, butler matrix [117]-[126] to achieve beamforming. There are multiple works reported [127]-[145] on SIW beamforming, and many other methods.

In this chapter, we explored circularly polarized hybrid mode SIW antenna for two-quadrant scanning beamforming. Figure 7.1 gives the designed methodology of the presented antenna in this chapter.
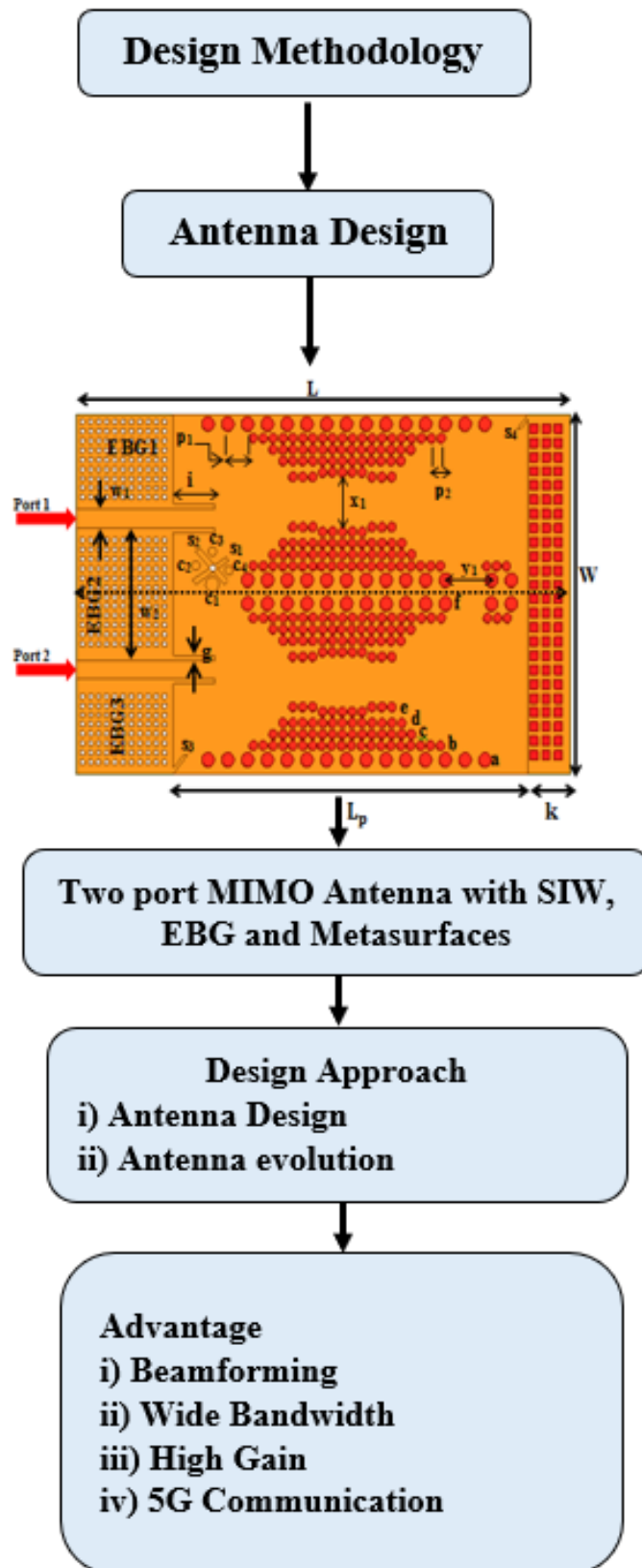
Figure 7.1: Designed methodology of the chapter-7 antenna.

7.2   Design of SIW Beamforming Antenna

Figure 7.2 depicts the structural design of the proposed SIW beamforming antenna for 5G applications. The structure's overall dimensions are $60\ mm\ (6.96\lambda_o) \times 38\ mm\ (4.4\ \lambda_o) \times 1.6\ mm\ (0.18\ \lambda_o)$. The antenna is fabricated on a Rogers 5880 substrate with a 1.6 mm thickness, permittivity of 2.2, and $tan\delta$ =0.0009. Vias of different diameters are used in this design. Vias with a larger diameter has four rows, whereas those with a smaller diameter have sixteen. As seen in Figure 7.2, the length of the rows varies depending on the location. Three EBG structures, EBG1, EBG2, and EBG3, are etched in the form of squares on the bottom ground (copper) layer. Each EBG square is $.5\ mm\ \times 0.5\ mm$.

The design equations consider for this work is shown below [142]-[143]:

$$W_{eff} = W - 1.08\frac{d^2}{p} + 0.1\frac{d^2}{W}$$

(7.1)

whereas d is the diameter of the via, p is the spacing between the vias, and the gap between two rows of vias is denoted by (W).

$$0.5 < d / p < 0.8$$

(7.2)

$$W = \frac{c}{2f\sqrt{\varepsilon_r}}$$

(a)   (b)
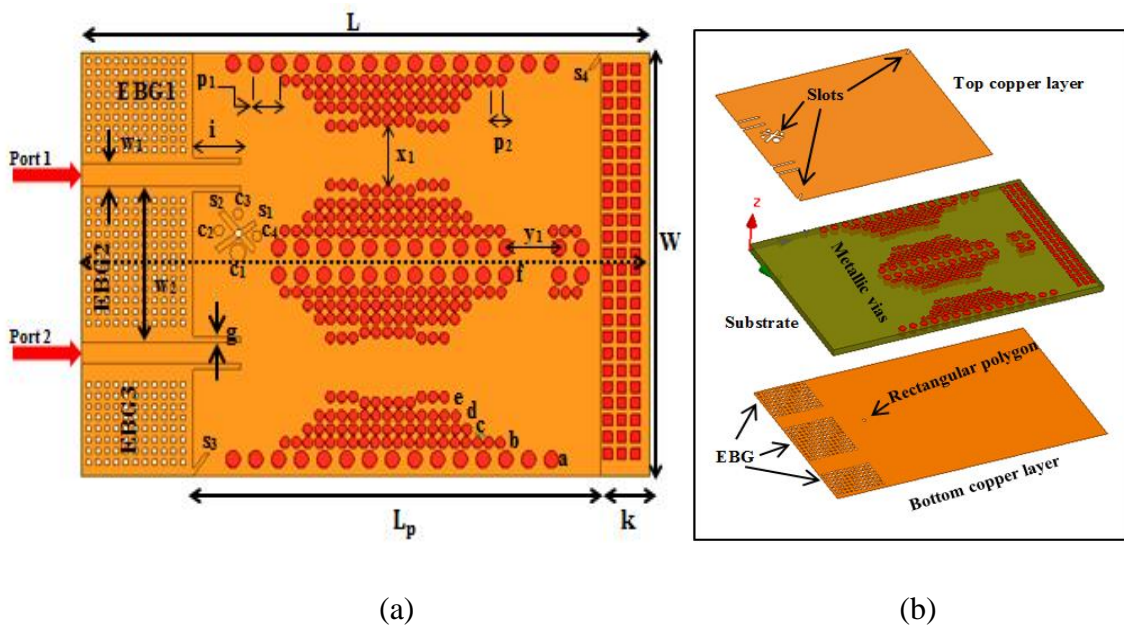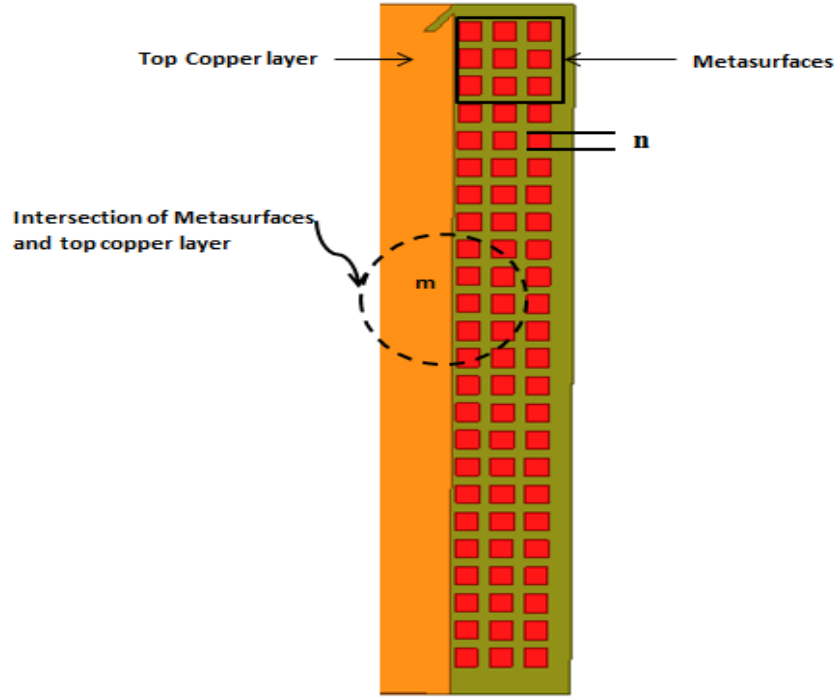
(c)

Figure 7.2: Layout of the proposed antenna (a) top view, (b) Layered structure, (c) metasurface cross section.

EBG1, EBG2, and EBG3 are configured as a matrix of 9×11, 12×11, 8×11. The distance between EBG1 and EBG2 is 4 mm, and the distance between EBG2 and EBG3 is 5 mm. On the top copper layer, two rectangular slots (S_1, S_2) with a $\pm 45^o$ inclination are orthogonally etched. Slot S_1 has length=4.8 mm, width=0.6 mm, whereas slot S_2 has a length of 4.8 mm, and width is 0.5 mm, respectively. On the bottom copper layer, immediately below the center of the cross slots, a six-segment rectangular polygon slot is etched. Two further slots, S_3 and S_4 are etched diagonally on a top copper layer with length and breadth of 1.8 mm and 1.9 mm, respectively. The cross-section of the metasurfaces is shown in Figure 7.2 (c). The 72 unit cells that make up the 2D metasurfaces are put on the substrate which is m distance away from the top metallic layer with a size of square metals n×n .

Table 7.1 shows the beamforming antenna's design parameters are given as $w_1 = 2$, $w_2 = 14$, $L = 60$, $W = 38$, $L_p = 43$, $k = 5.2$, $c_1 = 0.8$, $c_2 = c_3 = c_4 = 0.5$, $i = 5$, $g = 0.5$, $p_1 = 2.4$, $p_2 = 1.2$, $x_1 = 6.3$, $y_1 = 5.6$, $m = 0.2$, $n = 1$ (all units are in mm). Simulations were carried out by Ansys HFSS. Table 7.1 shows the detailed dimensions of the SIW rows. The fabricated proposed antenna is shown in Figure 7.3.

Table 7.1 SIW rows detailed dimensions

Vias Rows	a	b	c	d	e	f
Length (mm)	33.6	22.8	16.7	14.3	12	24
Width (mm)	1.5	1	1	1	2	1.5
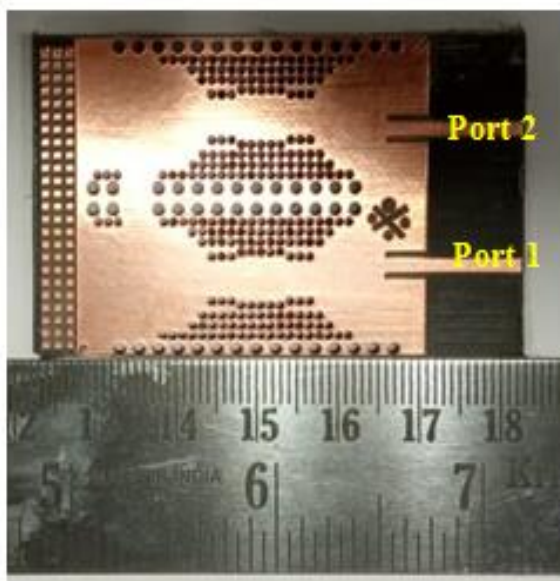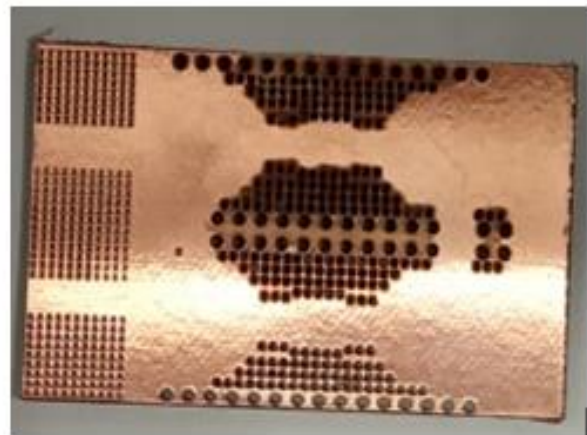
Figure 7.3: Prototype of the proposed antenna (a) top view, (b) bottom view, (c) metal filling of vias.

7.2.1 Design Evolution and Analysis of Proposed Antenna

Table 7.2 depicts the evolution of the proposed SIW beamforming antenna. The antenna's design evolution begins with a two-port microstrip patch antenna which is fed by an inset feed that resonates at 23 GHz, as illustrated in Ant1. The antenna's gain increases with frequency at first but the radiation pattern gets distorted. The length and width of slots S_1 and S_2 in Ant2 are configured to approximately $\lambda/4$, enabling the antenna to radiate. The radiation pattern is shifted with coverage of 60° in the azimuth plane because slots S_1, S_2 were inclined at 45°.

The two cross slots added capacitance and inductance, increasing gain while reducing return loss and axial ratio value. The antenna resonant frequency and S-parameters are unaffected by changes in slot length and width. As shown in Figure 7.4 (a), when the width of the slot S_1 was changed from 0.6 mm to 0.5 mm, all multi beams switched from the 2nd to the 1st quadrant without changing S-parameters. It is worth noting that the suggested antenna's 1st quadrant scanning ranges from 0° to 90°. Four circular slots were etched on the top patch to lower the axial ratio value and achieve circular polarization, but the antenna remained linearly polarized.

However, at its optimum dimensions of length = 4.8 mm and width = 0.6 mm, the proposed antenna scans 60° in the first two quadrants, as illustrated in Figure 7.4. (b).

(a)   (b)
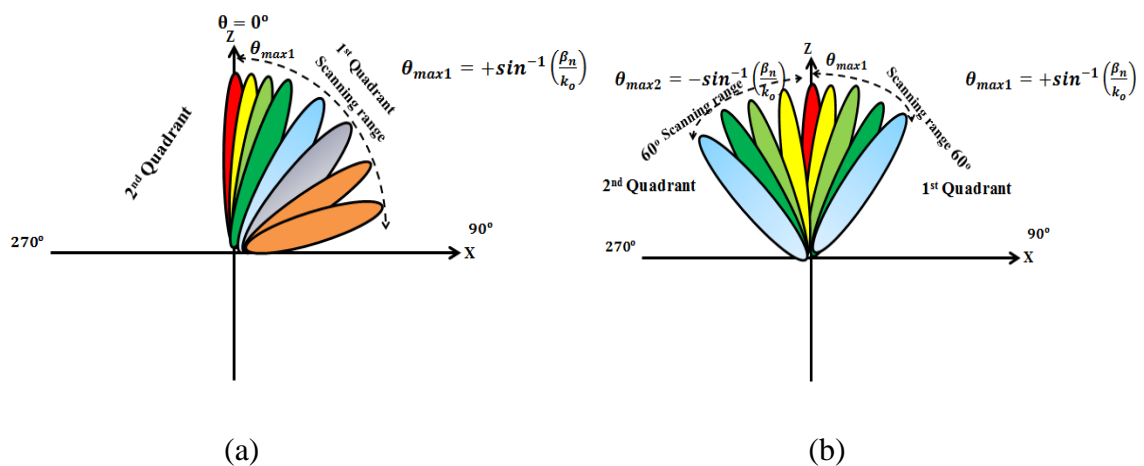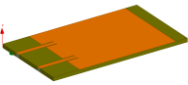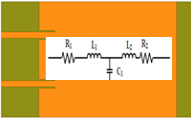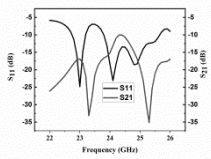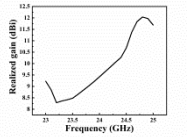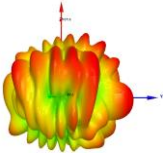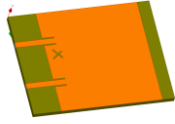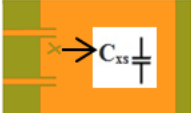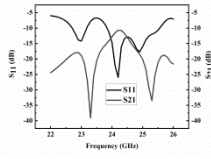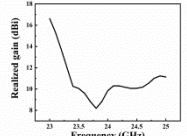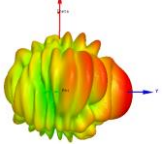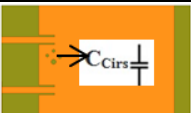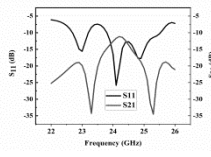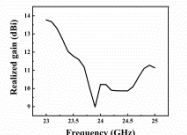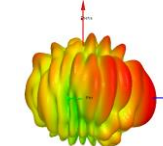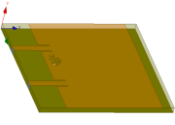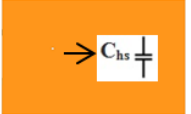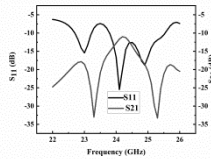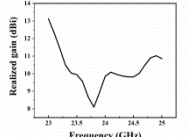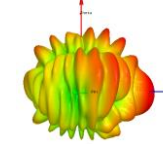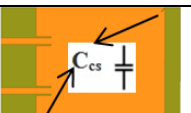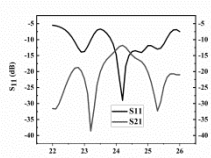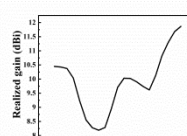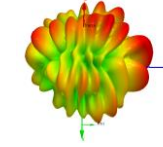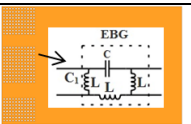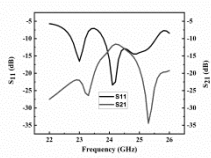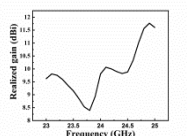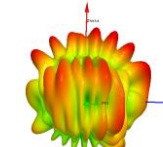
Figure 7.4: Quadrant scanning, (a) 1st quadrant radiation coverage 90°, (b) two quadrant radiation coverage 120° at 23.5 GHz.

Table 7.2 Evolution of the proposed antenna.

Antenna Evolutions	3D model	Structure with the equivalent circuit model	S-parameter	Realized Gain	3D Radiation Pattern
Ant1					
Ant2					
Ant3					
Ant4					
Ant5					
Ant6					

Ant7					
Ant8					
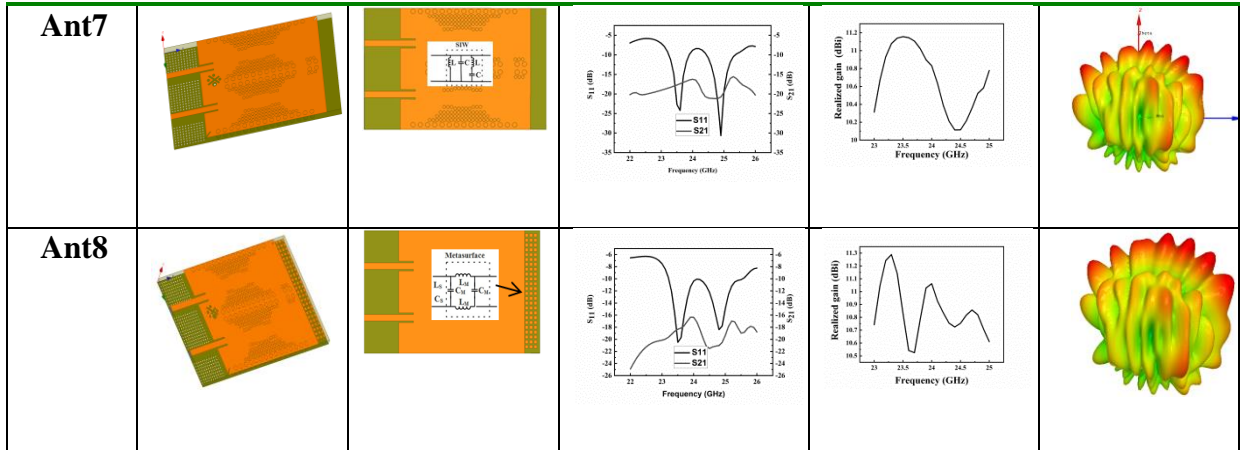
In Ant3, there is a minor change in S_{11} and S_{21}, but gain is better. Ant4 includes a rectangular polygon slot etched on the bottom layer of the ground plane which reduces the backward radiation. However, in Ant5, the two slots are diagonally etched on the top metallic layer, influencing the radiation pattern, isolation, and reducing the axial ratio also. The path of the current on the patch is controlled by a matrix of three EBG structures which also improves the isolation between the ports.

The spacing between the three EBG matrices has been adjusted to reduce port coupling. Without adding any additional decoupling circuit, the coupling between the ports is found to be below -10 dB. Figure 7.5 (a) depicts the coupling between the ports. It can be observed from Ant5 to Ant6, when the EBG structure is applied, the radiation in the unwanted direction is removed and the radiation pattern becomes more directed in the broadside direction.

The antenna's gain seems to have improved as well. Inductance and capacitance are created by the EBG's periodic structure, which increases the return loss and enhances isolation. It was also depicted that when the size of the metasurface units decreased, return loss improved and the frequency band shifted slightly lower band. The SIW cavity's length to width ratio is high, resulting in higher-order mode TE_{305}, which enhances gain. Figure 7.5 depicts the electric field distribution on the top metallic patch.

As shown in Figure 7.5, the maximum field in the y-direction is concentrated at the antenna's centre, i.e., E_{max}, with a value of 4.1103 V/m. In the x and z axes, however, the E_x and E_y fields are $< E_y$. Equation 1 calculates the hybrid mode's electric field distribution. 72 units of 2D metasurfaces are arranged on an extended section of the substrate, 0.2 mm away from the

top metallic layer, in the final design, Ant 8. Figure 7.6 compares the S-parameters of all antennas.

The normalized electric field for the conventional cavity mode TE_{m0p} can be written as

$$E_{yn} = \sin\left(\frac{m\pi x}{L_p}\right) * \sin\left(\frac{\pi z}{W}\right) \tag{7.3}$$

The electric field distribution for the proposed hybrid mode is calculated as

$$E_{yn|\text{mod}} = f(y) * \sin\left(\frac{\pi z}{W}\right) \tag{7.4}$$

$$f(y) = \sin\left(\frac{3\pi x}{L_p}\right) * \sin\left(\frac{5\pi}{W}\right) = \frac{1}{2}\left[\cos\left(\frac{3\pi x}{L_p} - \frac{5\pi}{W}\right) - \cos\left(\frac{3\pi x}{L_p} + \frac{5\pi}{W}\right)\right] \tag{7.5}$$

(a)   (b)
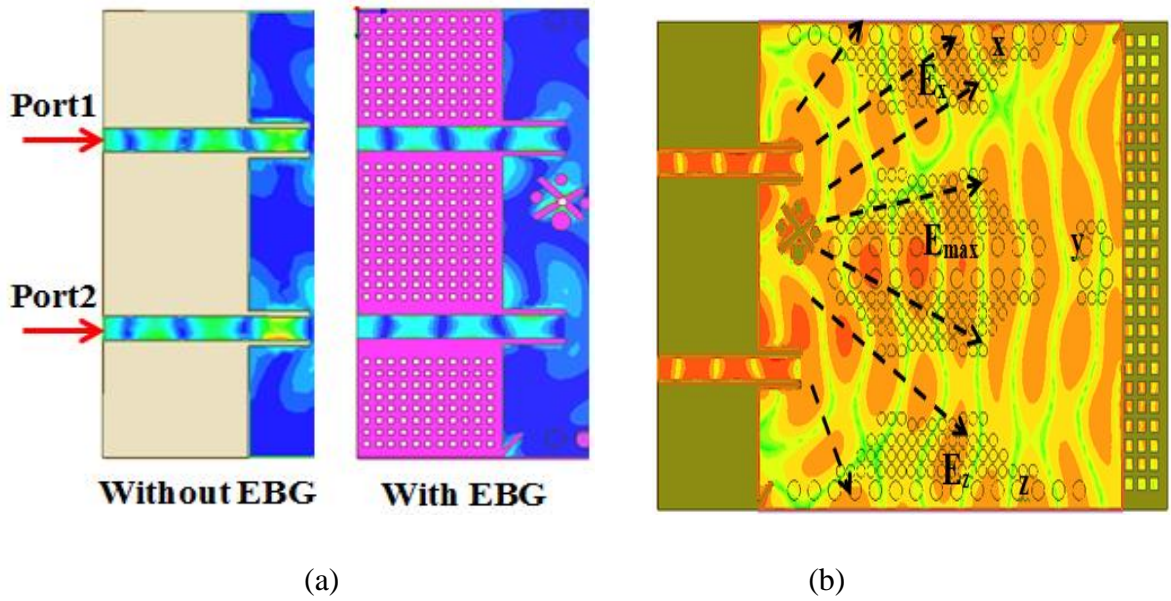
Figure 7.5: (a) Mutual coupling between the ports, (b) Electric field distribution of the proposed antenna.
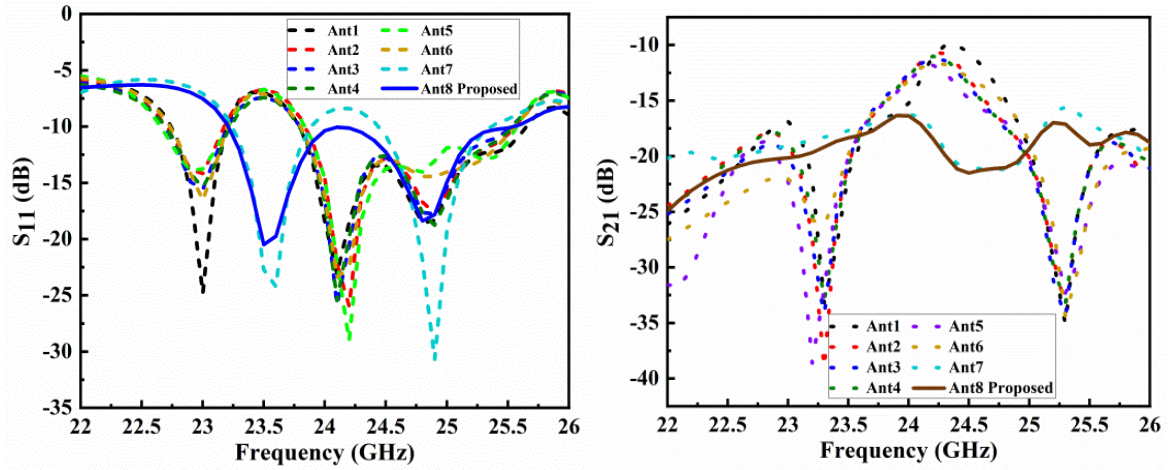
(a)   (b)
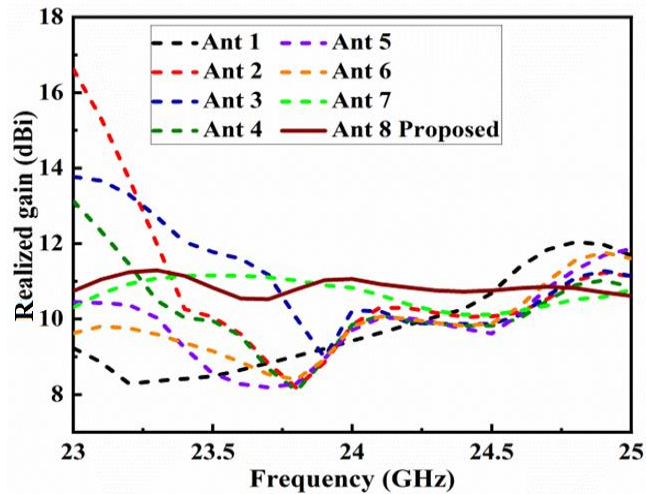
(c)

Figure 7.6: Simulated and measured results of the proposed antenna. (a) S_{11}, (b) S_{21}, and (c) realized gain.

The subwavelength rectangular structure of the metasurfaces depicted in this design has a dimension of $0.11\lambda_0 \times 0.11\lambda_0$. The periodicity in the metasurfaces' structure resulted in a gain of 10.8 dBi, which appears to be quite high when compared to the other antennas depicted in Figure 7.6.

7.3   Simulated and Measured Results

The proposed antenna is fabricated and R & S ZNB40 vector network analyzer is used to test the EBG-based SIW beamforming antenna. Figure 7.7 depicts the simulated and measured S-parameters.

(a)   (b)
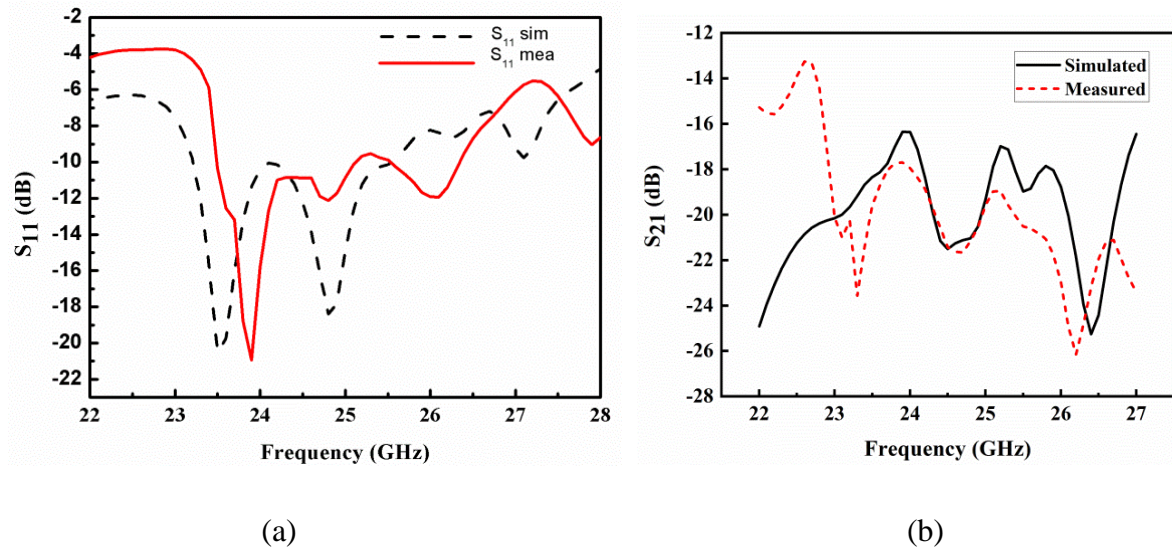
Figure 7.7: Simulated and measured S-parameters of proposed, (a) S_{11}, (b) S_{21}.

Figure 7.7 (a) shows that the proposed antenna covers 23.5-25.5 GHz band, whereas Figure 7.7 (b) shows that the ports are isolated by 19 dB. As shown in Figure 7.8, the measured values of realized gain and radiation efficiency are 9.8 dBi and 94.5 %, respectively. Within the band, the axial ratio is less than 3 dB, as indicated in Figure 7.8. (c).

(a)   (b)
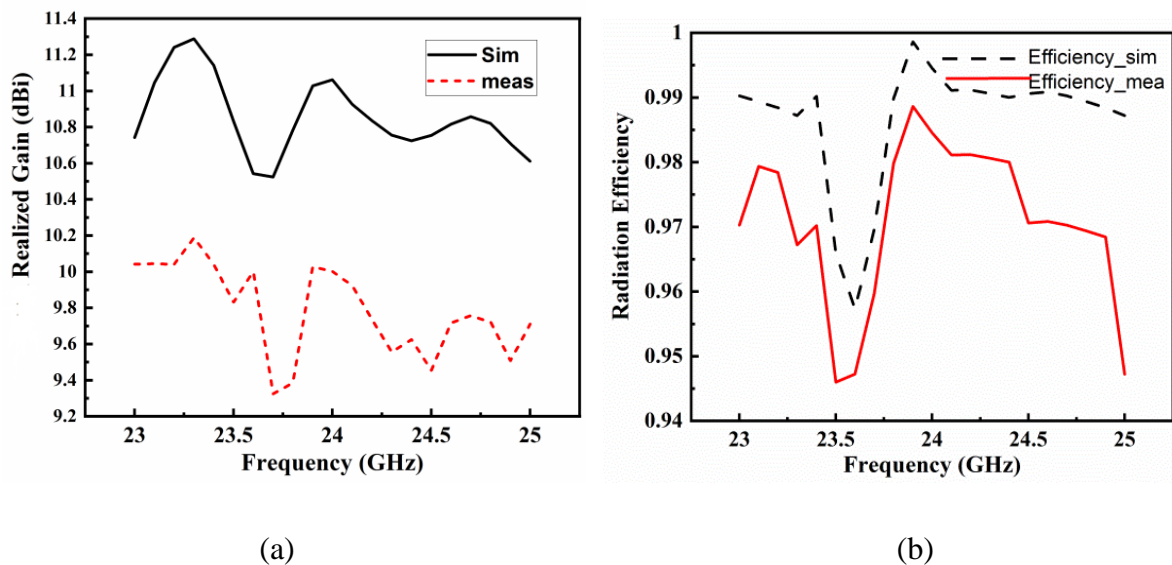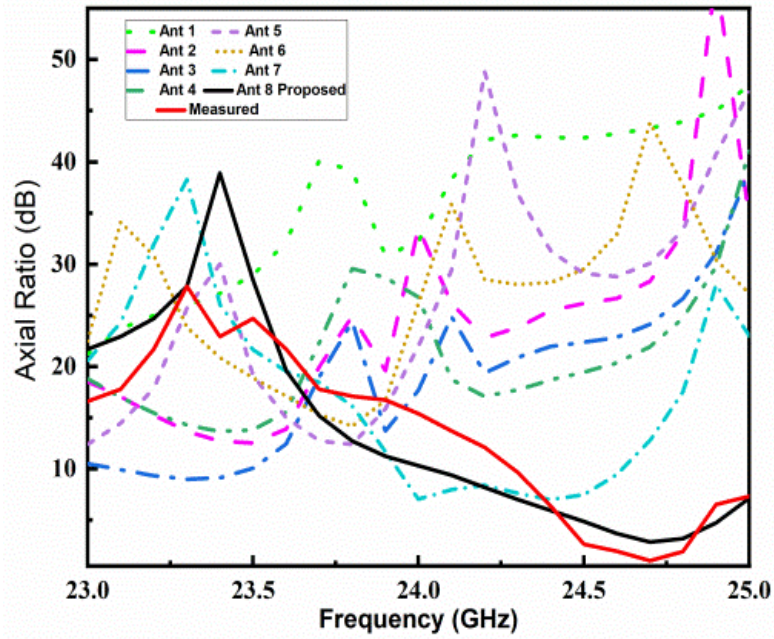
(c)

Figure 7.8: Simulated and measured (a) Realized gain, (b) Radiation efficiency, (c) Axial ratio of the proposed antenna.

Figure 7.9 depicts the proposed antenna's measured far-field radiation pattern. The proposed antenna's FTBR is expected to be 25.7 dB from both ports.
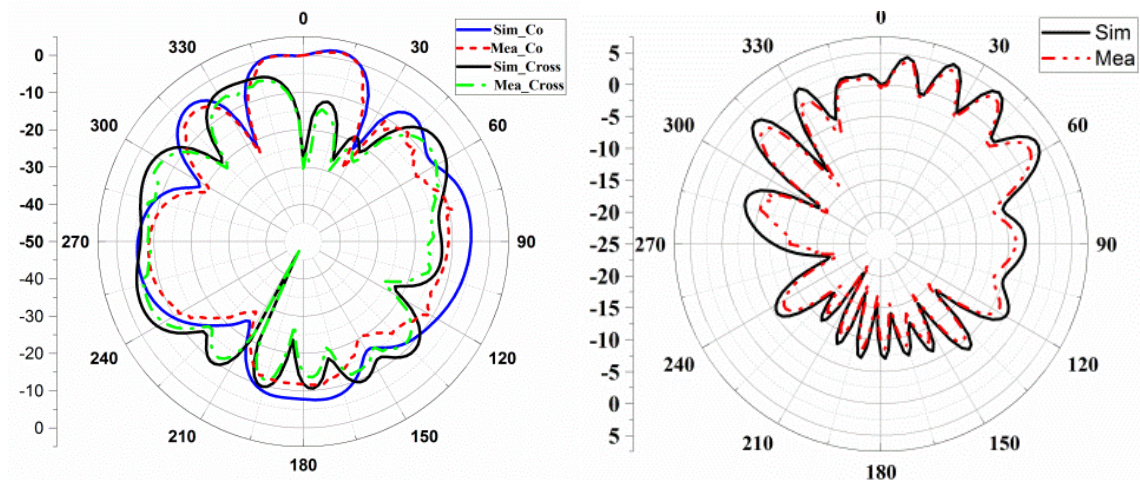
(a)   (b)

Figure 7.9: Far-field radiation pattern of the proposed antenna at 23.5 GHz, (a) E-plane co-cross polarization, (b) 2D radiation pattern at phi=90º.

For 5G communication, the diversity performance of the multiple-input and multiple-output antenna is essential.

Figure 7.10 shows the envelope correlation coefficient (ECC), diversity gain (DG), total active reflection coefficient (TARC), and channel capacity loss (CCL) of the proposed antenna diversity performance [144]-[145].

When the antenna efficiency is high, the envelope correlation coefficient can be estimated using the S-parameters approach instead of far-field radiation patterns [144]-[145]. The following equation can be used to determine the ECC:

$$ECC = \left| \frac{\left| S_{11}^* S_{12} + S_{12}^* S_{22} \right|}{\left\| (1-|S_{11}|^2 - |S_{21}|^2)(1-|S_{12}|^2 - |S_{22}|^2)(\eta_{rad,1}\eta_{rad,2}) \right|^{\frac{1}{2}}} \right|^2 \tag{7.6}$$

As shown in Figure 7.10 (a), the measured value of ECC within the band is 0.009. The value of ECC for the case of the MIMO antenna should be less than 0.5.

(a)

127
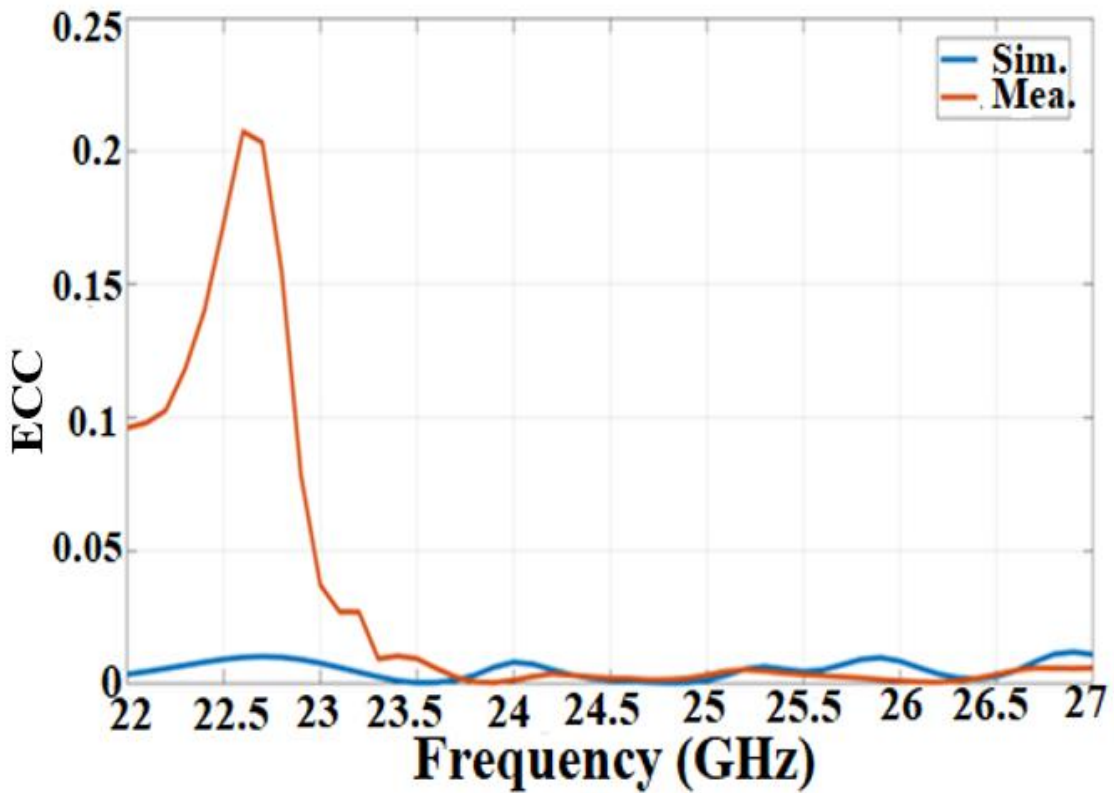
The proposed MIMO antenna's diversity gain (DG) can be determined using the equation:

$$DG = 10 \times \sqrt{(1 - ECC)^2} \tag{7.7}$$

The calculated diversity gain is 9.9 dB.

TARC is another parameter for the proposed antenna's diversity performance, and it is defined as follows:

$$TARC = \frac{Total\ reflected\ power}{Total\ incident\ power}$$

The return loss of the entire MIMO system is calculated using TARC.

TARC may be determined from S-parameters given the equation for a two-port MIMO system.

$$TARC = \sqrt{\frac{\left(S_{11} + S_{12}\right)^2 + \left(S_{22} + S_{21}\right)^2}{2}} \tag{7.8}$$

The measured and simulated values of TARC at $\theta = 0^o, 30^o, 60^o, 90^o, 180^o$ are shown in Figure 7.10 (b). Figure 7.10 (b) shows that the simulated and measured value of TARC is less than -6 dB within the band coverage of 23.5 GHz.

The channel capacity loss (CCL), commonly known as Shannon's channel capacity theorem, determines how much information may be transferred at a maximum rate without interference from the environment. The CCL may be calculated using the following equation:

$$\sigma_{ii}'|\&' = 1 - \left(|S_{ii}|^2 - |S_{ij}|^2\right) \tag{7.9}$$

$$\sigma_{ij}'|\&' = -\left(S_{ii}{}^* S_{ij} - S_{ji} S_{ji}{}^*\right)$$

Figure 7.10 (c) shows that both simulated and measured CCL values are less than 0.4 bits/seconds/Hz.
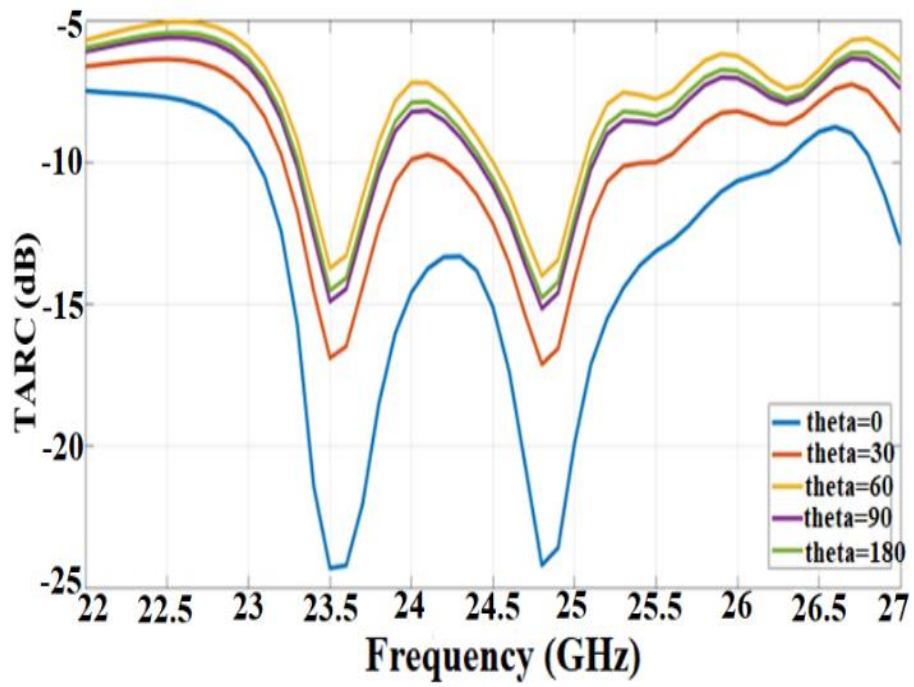
Simulated

Measured

(b)

129
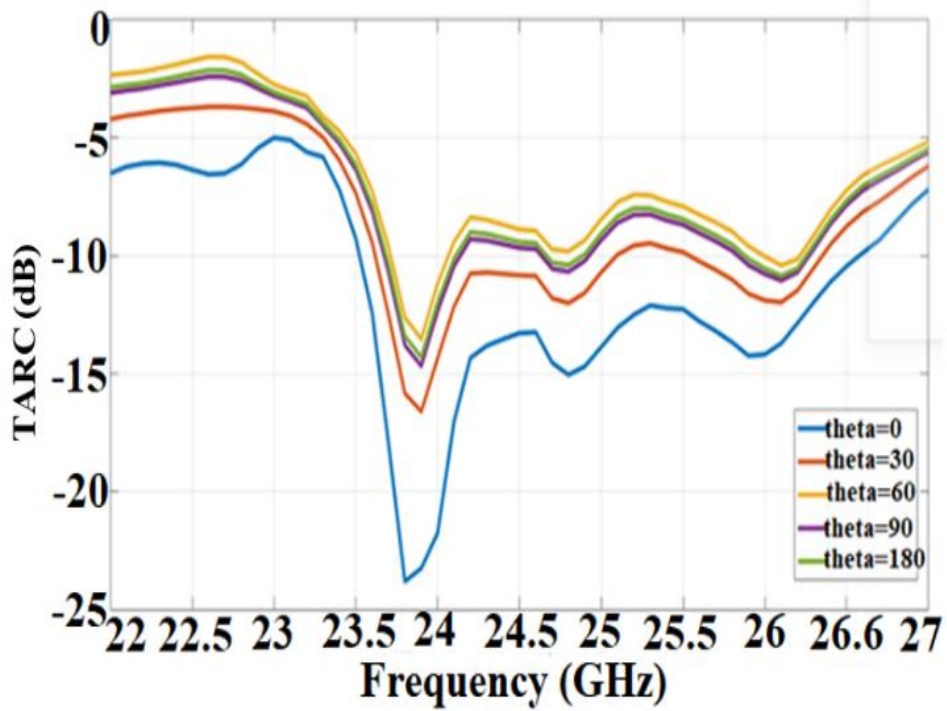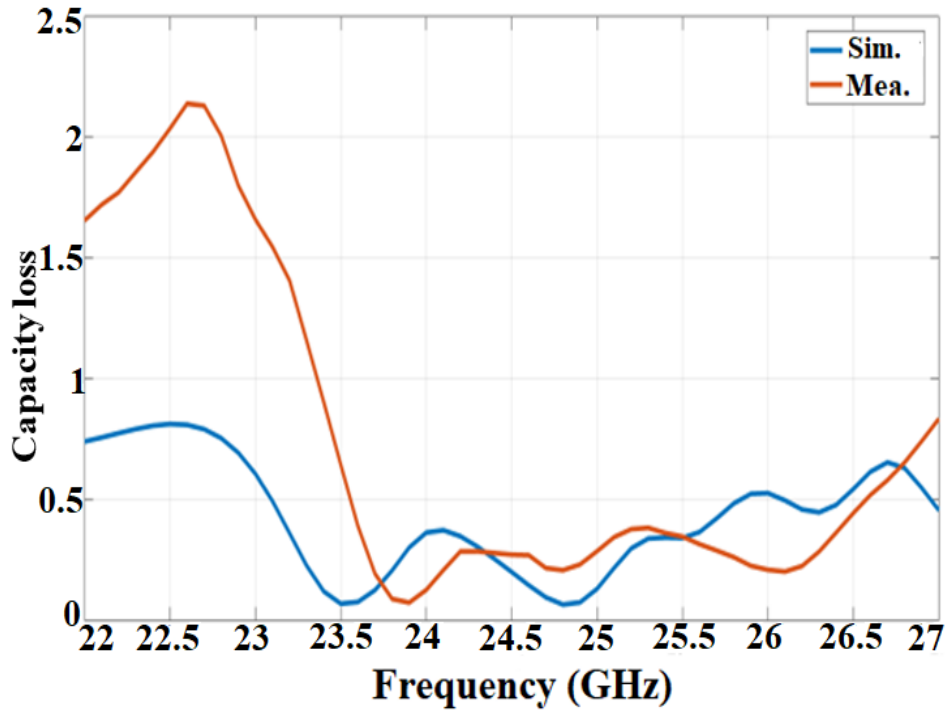
(c)

Figure 7.10: Diversity performance of the proposed antenna, (a) Envelope correlation coefficient. (b) Total active reflection coefficient. (c) Channel capacity loss.

7.4 Observations and Comparisons of Proposed Antenna with Existing Designs

In this section, the comparison between the presented antenna and its performances are compared with other published works, also compared based. Table 7.3 shows the comparative comparison among the related reference antennas, which have been published in the literature [117-120] and presented antenna performance. The presented antenna gives the -10 dB impedance bandwidth, beamforming, circular polarization with two-port MIMO SIW which are better compared to the published works. It offers a compact size with a wide scanning range compared with existing structures.

Table 7.3 Comparison of proposed work with different existing antennas

Ref	Antenna type	Size (λ^3)	Frequency band (GHz)	Realized gain (dBi)	Beamforming (Degree)
[117]	1×4 PFSA array	$1.98 \times .23 \times 0.11$	37-39	7.7	$\pm 50^o$
[118]	Slow wave SIW	$8.67 \times 0.91 \times 0.073$	13.5-13.9	9.2	35°
[119]	SIW antenna array	$0.48 \times 0.48 \times 0.09$	$24.25 - 29.5$	10.1 ± 0.7	$\pm 50^o$
[120]	4×6 Butler matrix (BM) based antenna array	$5.6 \times 4.6\lambda$	27.5, 28.5	11	$\pm 45^o$
Present Work	SIW MIMO antenna	$4.7 \times 2.97 \times 0.12$	23.5-25.5	9.8	$\pm 60^o$

7.5   Conclusion

This chapter discussed with the designed and analysis of the circularly polarized EBG based two-port MIMO. The antenna has been developed in this chapter by using the SIW, metasurface for obtaining beamforming and behaviour of circularly polarized radiations.

SIW generates multibeam using the proposed structure, which scans the first two quadrants with 120° coverage. Each quadrant generates four beams. MS is used to convert linear to circular polarisation using 72 periodic units. The proposed antenna operates in the frequency range of 23.5-25.5 GHz. It has a realized gain of 9.8 dBi and a 94.5 % radiation efficiency. The antenna's diversity performance, such as ECC, diversity gain, TARC, and CCL, meet the requirements of the 5G MIMO system.

CHAPTER 8

Conclusion and Future Scope

This chapter is mainly separated into two segments: (i) conclusions of the complete research work, which have been discussed in this given thesis, and (ii) the future scope of the given research work. The presented thesis is mainly focused on the high gain, beamforming, beam scanning and beam splitting.

8.1   Conclusion of the Presented Work

In the first chapter, a brief introduction of 5G technology and the expected spectrums were described. Next, the requirements of the antennas i.e., monopole, PIFA and microstrip patch antenna in future wireless technology were also discussed. In the end, for beam steering and gain enhancement, different types of periodic structures like AMC, uniform superstrate, non-uniform superstrate were explored. This introduction laid the foundation that is needed to appreciate the work performed in this thesis.

In the second chapter, we started with the design of a compact planar inverted-F antenna (PIFA). It is found that the gain and bandwidth of the antenna are low while the SAR value is high which may not be useful for 5G and other applications. To counter low gain, the gain enhancement of the PIFA antenna was explored by applying AMC. On the other hand, the SAR contribution leading to the undesired electromagnetic radiation towards the human body was analyzed using three- and four-layer of the human tissue model. Once the reason for high SAR was known, the SAR reduction technique with AMC was used, reducing SAR to a low value. The value of SAR of the proposed antenna was found to be lower than the IEEE standards which shows the effectiveness of the AMCs. When measured, the proposed antenna had an impedance bandwidth of 4.8–6.7 GHz (33 % with center frequency at 5.75 GHz) and a maximum gain of 7.6 dBi, making it appropriate for WLAN, satellite uplink C-band, and sub-6 5G applications.

In the third chapter, we designed a coplanar waveguide fed monopole antenna. Traditional planar monopole antennas have low gain and might not be usable for many applications due to it. While the use of AMC and superstrate is used for gain enhancements, it has never been employed for planar monopole antennas in a single design. So, we approached this low gain problem in a systematic manner. Hence, to achieve high gain, we used AMC as well as superstrate for enhancing the forward radiation from the antenna. However, superstrates demand for materials with high dielectric constants but these materials are either not available commercially off-the-shelf or are very expensive compared to traditional dielectrics. That motivated us to study three different superstrates and discussed how they can be used in place of each other without sacrificing antenna performance. Finally, one of these three superstrates was fabricated with the monopole and AMC combination. The fabricated coplanar waveguide fed monopole antenna with AMC and superstrate showed the measured impedance bandwidth of 15.7% (3.2-3.75 GHz) and has the maximum gain of 7 dBi which is well suited for 5G and WiMAX applications.

In the fourth chapter, we explored a beam-steering antenna based on a non-uniform metasurface superstrate and AMC as beam steering with low scan loss is going to be a necessity for 5G communications. The proposed antenna in this work can steer the beam along $\theta = -18°$ and $18°$ with the superstrate and along $\theta = 0°$ in the absence of the superstrate with almost zero scan loss. The antenna, working at 3.5 GHz, due to these qualities is an ideal candidate for 5G, WiMAX, and WLAN applications.

In the fifth chapter, we explored how an Eccosorb MCS absorber can be used to transform the radiation pattern of a slotted planar inverted-F antenna (PIFA). The structure of the PIFA antenna with and without absorber was analyzed to see whether the antenna performance might be improved. We showed that by using an absorber, the radiation pattern can be transformed, producing a radiation beam in the desired direction while also increasing the antenna's gain.

Extending the work performed in the fifth chapter, we designed a planar inverted-F multi-beam antenna using RF absorbers in the sixth chapter. The multi-beam antennas mostly require a complex system of multiple antennas such as a phased array or MIMO antennas and make the system bulky as well as power-hungry. The proposed antenna circumvented these

limitations and provided multiple beams from a single antenna with wide angular coverage. The designed antenna achieved a multi-beam behaviour by six slabs of absorbers placed periodically between the PIFA patch and substrate to split the beams into two directions at $\pm26^o$. This design fulfills the multibeam requirements not just for 5G but for other latest communication systems too.

In the seventh chapter, we designed a circularly polarized MIMO antenna for the 5G band at millimeter-wave frequencies (23.5-25.5 GHz). As microstrip or CPW type of transmission lines incur a high loss at millimeter frequencies, the antennas at these frequencies call for SIW based designs for low loss. As a result, in this chapter, a novel SIW structure was used to perform beamforming. This work comprised different types of vias and slots that achieve multibeam in the 1st and 2nd quadrant with 120° angular coverage. The introduction of slots also improves the axial ratio and antenna gain. The proposed antenna also benefited by using EBG and metasurfaces to produce right-handed circular polarized radiations within the desired band of 23.5-25.5 GHz with good return loss. Finally, the MIMO's diversity properties were investigated. In all aspects, the proposed antenna performs well for 5G applications.

8.2   Future Scope of the Presented Work

This thesis gives the concepts of various periodic structures for high gain, beamforming, beam scanning, and beam splitting in different antennas like monopole, PIFA, and microstrip patch antenna. Lastly, a EBG based SIW concept is also included in the thesis for achieving better antenna performance in terms of wide scanning range and high gain. This thesis mainly discussed the periodic structures such as AMC, uniform superstrate, non-uniform superstrate, RF absorber; one can also try to develop some other beamformers.

This thesis mostly concentrated on the basic design of the antennas, so it is also possible to used different designs to obtain wideband applications.

Multi-antenna systems are required for 5G and future wireless technology, such as 6G, which uses higher frequency ranges such as millimeter-wave and terahertz. The higher the frequency, the harsher the propagation conditions for electromagnetic waves will be. Multi-antenna setups and beamforming can help mitigate this to some extent.

There is more need to work on circular polarization which is useful for 5G and 6G. Therefore, FSS (frequency selective surface) which can be used to achieve circular polarization with high gain.

In beamforming antennas, generally, the gain becomes low during the scanning, so one can also try to develop and use the concepts of intelligent reflecting surface or some other different techniques to enhance the gain along with beamforming and beam scanning.

References

1. Su, W., Liu, Q., He, H. and Zhang, H., 2010. A new context awareness scheme for multi-mode mobile terminals in mobile Internet, IET 3rd International Conference on Wireless, Mobile and Multimedia Networks, pp. 95-98.

2. Huang, H.C., 2018, March. Overview of antenna designs and considerations in 5G cellular phones. In 2018 International Workshop on Antenna Technology (iWAT) (pp. 1-4). IEEE.

3. Calin, D., 2015, July. Technologies for future broadband wireless evolution. In 2015 IEEE 14th Canadian Workshop on Information Theory (CWIT) (pp. 58-61). IEEE.

4. 5G Vision, 5G PPP, 2015.

5. Ohishi, T., Oodachi, N., Sekine, S. and Shoki, H., 2005, July. A method to improve the correlation coefficient and the mutual coupling for diversity antenna. In 2005 IEEE Antennas and Propagation Society International Symposium (Vol. 1, pp. 507-510). IEEE.

6. Ban, Y.L., Li, C., Wu, G. and Wong, K.L., 2016. 4G/5G multiple antennas for future multi-mode smartphone applications. IEEE access, 4, pp.2981-2988.

7. Rawat, A., Yadav, R.N. and Shrivastava, S.C., 2012. Neural network applications in smart antenna arrays: A review. AEU-International Journal of Electronics and Communications, 66(11), pp.903-912.

8. Cisco. Visual Networking Index. White paper, 2015. [Online]. Available: www.Cisco.com.

9. Honcharenko, W., Kruys, J.P., Lee, D.Y. and Shah, N.J., 1997. Broadband wireless access. IEEE Communications Magazine, 35(1), pp.20-26.

10. Shafi, M., Hashimoto, A., Umehira, M., Ogose, S. and Murase, T., 1997. Wireless communications in the twenty-first century: A perspective. Proceedings of the IEEE, 85(10), pp.1622-1638.

11. Frattasi, S., Fathi, H., Fitzek, F.H., Prasad, R. and Katz, M.D., 2006. Defining 4G technology from the users perspective. IEEE network, 20(1), pp.35-41.

12. GSMA Intelligence, "Understanding 5G: Perspectives on future technological advancements in mobile," White paper.

13. Agiwal, M., Roy, A. and Saxena, N., 2016. Next generation 5G wireless networks: A comprehensive survey. IEEE Communications Surveys & Tutorials, 18(3), pp.1617-1655.

14. Rappaport, T.S., Roh, W. and Cheun, K., 2014. Wireless engineers long considered high frequencies worthless for cellular systems. they couldn't be more wrong. IEEE SPECTRUM, 51(9), pp.34-58.

15. Ghosh, A., Maeder, A., Baker, M. and Chandramouli, D., 2019. 5G evolution: A view on 5G cellular technology beyond 3GPP release 15. IEEE access, 7, pp.127639-127651.

16. https://www.gsma.com/spectrum/wp-content/uploads/2021/04/5G-Spectrum-Positions.pdf.

17. J. D. Kraus, "Antennas", McGraw-Hill, New York, 1988.

18. C. A Balanis, "Antenna Theory: analysis and Design", Hoboken, NJ: John Wiley & Sons, 2005.

19. https://www.allaboutcircuits.com/news/sub6g-and-mmwave-solutions-cut-through-haze-of-5g-antenna-design/.

20. M. N. Hamdy, "Beamformers Explained," COMMSCOPE,

21. Chang, D., 1968. On the electrically thick monopole: Part I--Theoretical solution. IEEE Transactions on Antennas and Propagation, 16(1), pp.58-64.

22. Chen, H., Yang, X., Yin, Y.Z., Fan, S.T. and Wu, J.J., 2013. Triband planar monopole antenna with compact radiator for WLAN/WiMAX applications. IEEE Antennas and Wireless Propagation Letters, 12, pp.1440-1443.

23. Boutayeb, H. and Denidni, T.A., 2007. Gain enhancement of a microstrip patch antenna using a cylindrical electromagnetic crystal substrate. IEEE transactions on antennas and propagation, 55(11), pp.3140-3145.

24. Hall, Peter S.; Lee, E.; Song, C. T. P., "Planar inverted-F antennas", pp. 197–227, in Waterhouse, Rod (ed), Printed Antennas for Wireless Communications, John Wiley & Sons, 2008.

25. Rowell, C.R. and Murch, R.D., 1997. A capacitively loaded PIFA for compact mobile telephone handsets. IEEE Transactions on antennas and Propagation, 45(5), pp.837-842.

26. Salonen, P., Sydanheimo, L., Keskilammi, M. and Kivikoski, M., 1999, October. A small planar inverted-F antenna for wearable applications. In Digest of papers. Third international symposium on wearable computers (pp. 95-100). IEEE.

27. E. 0. Hammerstad and F. Bekkadal, "Microstrip Handbook." ELAB Report STF44 A74169, The Norwegian lnstitute of Technology. Trondheim, Norway, 1975.

28. Jayasinghe, J.M. and Uduwawala, D., 2015. A novel multiband miniature planar inverted F antenna design for bluetooth and WLAN applications. International Journal of Antennas and Propagation, 2015.

29. K. L. Wong. "Compact and broadbandmicrostrip antennas". New York: JohnWiley & Sons Inc, 2003.

30. Gao, G.P., Yang, C., Hu, B., Zhang, R.F. and Wang, S.F., 2019. A wide-bandwidth wearable all-textile PIFA with dual resonance modes for 5 GHz WLAN applications. IEEE Transactions on Antennas and Propagation, 67(6), pp.4206-4211.

31. Firoozy, N. and Shirazi, M., 2011. "Planar Inverted-F Antenna (PIFA) design dissection for cellular communication application," J. Electromag. Anal. Appl., 3, pp. 406–411.

32. Van Trinh, T., Kim, G., Kim, J. and Jung, C.W., 2018. Wideband internal PIFA-loop antenna designed on the bezel of digital television applications for UHF band. Electronics Letters, 54(22), pp.1260-1262.

33. Chen, H.D. and Tsao, Y.H., 2010. Low-profile PIFA array antennas for UHF band RFID tags mountable on metallic objects. IEEE Transactions on Antennas and Propagation, 58(4), pp.1087-1092.

34. ievenpiper, D., Zhang, L., Broas, R.F., Alexopolous, N.G. and Yablonovitch, E., 1999. High-impedance electromagnetic surfaces with a forbidden frequency band. IEEE Transactions on Microwave Theory and techniques, 47(11), pp.2059-2074.

35. Yang, F. and Rahmat-Samii, Y., 2003. Reflection phase characterizations of the EBG ground plane for low profile wire antenna applications. IEEE Transactions on antennas and propagation, 51(10), pp.2691-2703.

36. Foroozesh, A. and Shafai, L., 2008. Application of combined electric-and magnetic-conductor ground planes for antenna performance enhancement. Canadian Journal of Electrical and computer engineering, 33(2), pp.87-98.

37. Gao, G.P., Yang, C., Hu, B., Zhang, R.F. and Wang, S.F., 2018. A wearable PIFA with an all-textile metasurface for 5 GHz WBAN applications. IEEE Antennas and Wireless Propagation Letters, 18(2), pp.288-292.

38. Yang, W., Wang, H., Che, W. and Wang, J., 2013. A wideband and high-gain edge-fed patch antenna and array using artificial magnetic conductor structures. IEEE Antennas and Wireless Propagation Letters, 12, pp.769-772.

39. Han, K., Swaminathan, M., Pulugurtha, R., Sharma, H., Tummala, R., Yang, S. and Nair, V., 2015. Magneto-dielectric nanocomposite for antenna miniaturization and SAR reduction. IEEE Antennas and Wireless Propagation Letters, 15, pp.72-75.

40. Lai, H.W., Mak, K.M. and Luk, K.M., 2015. Shorted bowtie patch antenna with less susceptibility to surface condition. IEEE Transactions on Antennas and Propagation, 64(1), pp.306-311.

41. Pan, Y.M., Hu, P.F., Zhang, X.Y. and Zheng, S.Y., 2016. A low-profile high-gain and wideband filtering antenna with metasurface. IEEE Transactions on Antennas and Propagation, 64(5), pp.2010-2016.

42. Joubert, J., Vardaxoglou, J.C., Whittow, W.G. and Odendaal, J.W., 2011. CPW-fed cavity-backed slot radiator loaded with an AMC reflector. IEEE Transactions on Antennas and Propagation, 60(2), pp.735-742.

43. Ta, S.X. and Park, I., 2014. Dual-band low-profile crossed asymmetric dipole antenna on dual-band AMC surface. IEEE Antennas and Wireless Propagation Letters, 13, pp.587-590.

44. Ta, S.X. and Park, I., 2013. Design of miniaturized dual-band artificial magnetic conductor with easy control of second/first resonant frequency ratio. Journal of electromagnetic engineering and science, 13(2), pp.104-112.

45. Hossain, M.I., Faruque, M.R.I. and Islam, M.T., 2016, November. Low SAR planar inverted-F antenna for mobile phone. In 2016 International Conference on Advances in Electrical, Electronic and Systems Engineering (ICAEES) (pp. 572-576). IEEE.

46. Vieira, V.F., Pessoa, L.M. and Carvalho, M.I., 2017. Evaluation of SAR induced by a Planar Inverted-F Antenna based on a Realistic Human Model. In EMBEC & NBC 2017 (pp. 599-602). Springer, Singapore.

47. Bang, J. and Choi, J., 2018. A SAR reduced mm-wave beam-steerable array antenna with dual-mode operation for fully metal-covered 5G cellular handsets. IEEE Antennas and Wireless Propagation Letters, 17(6), pp.1118-1122.

48. Hossain, M.I., Faruque, M.I. and Islam, M.T., 2015. Investigation of hand impact on PIFA performances and SAR in human head. Journal of applied research and technology, 13(4), pp.447-453.

49. Alemaryeen, A. and Noghanian, S., 2019. On-body low-profile textile antenna with artificial magnetic conductor. IEEE Transactions on Antennas and Propagation, 67(6), pp.3649-3656.

50. Raad, H.R., Abbosh, A.I., Al-Rizzo, H.M. and Rucker, D.G., 2012. Flexible and compact AMC based antenna for telemedicine applications. IEEE Transactions on antennas and propagation, 61(2), pp.524-531.

51. Choudhury, S., Mohan, A. and Guha, D., 2018. Wideband quasi-omnidirectional planar inverted F-Antenna for compact wireless systems. IEEE Antennas and Wireless Propagation Letters, 17(7), pp.1305-1308.

52. Ali, M, Arya, R. K, Yerrola, A. K, Murmu, L, and Kumar, A., 2021. Bandwidth and gain enhancement with cross polarization suppression in microstrip antenna. URSI GASS, Rome, Italy.

53. Can, S. and Yılmaz, A.E., 2016. Reduction of specific absorption rate with artificial magnetic conductors. International Journal of RF and Microwave Computer-Aided Engineering, 26(4), pp.349-354.

54. P. A. Hasgall, F. Di Gennaro, C. Baumgartner, E. Neufeld, B. Lloyd, M. C. Gosselin, D. Payne, A. Klingenböck, and N.Kuster. "IT'IS Database for thermal and electromagnetic parameters of biological tissues," Version 4.0, May 15, 2018.

55. Deng, C., Xie, Y.J. and Li, P., 2009. CPW-fed planar printed monopole antenna with impedance bandwidth enhanced. IEEE Antennas and Wireless Propagation Letters, 8, pp.1394-1397.

56. Mondal, S., Sinha, A. and Routh, J., 2015. A survey on evolution of wireless generations 0G to 7G. International Journal of Advance Research in Science and Engineering (IJARSE), 1(2), pp.5-10.

57. Bhalla, M.R. and Bhalla, A.V., 2010. Generations of mobile wireless technology: A survey. International Journal of Computer Applications, 5(4), pp.26-32.

58. Princess, J.P., Let, G.S., Rizopackiamary, P. and Keziah, J., 2019, March. Design of Dual-band Monopole Antenna for Mobile Communications. In 2019 2nd International Conference on Signal Processing and Communication (ICSPC) (pp. 70-73). IEEE.

59. Beigi, P. and Mohammadi, P., 2016. A novel small triple-band monopole antenna with crinkle fractal-structure. AEU-International Journal of Electronics and Communications, 70(10), pp.1382-1387.

60. Jafargholi, A., Kamyab, M. and Veysi, M., 2010. Artificial magnetic conductor loaded monopole antenna. IEEE Antennas and Wireless Propagation Letters, 9, pp.211-214.

61. Tan, W. and Shen, Z., 2017. A dual-band dual-sleeve monopole antenna. IEEE Antennas and Wireless Propagation Letters, 16, pp.2951-2954.

62. Beigi, P. and Mohammadi, P., 2016. A novel small triple-band monopole antenna with crinkle fractal-structure. AEU-International Journal of Electronics and Communications, 70(10), pp.1382-1387.

63. Deng, C., Lv, X. and Feng, Z., 2017. High gain monopole antenna with sleeve ground plane for WLAN applications. IEEE Antennas and Wireless Propagation Letters, 16, pp.2199-2202s.

64. Jiang, Z.H., Gregory, M.D. and Werner, D.H., 2011. A broadband monopole antenna enabled by an ultrathin anisotropic metamaterial coating. IEEE Antennas and Wireless Propagation Letters, 10, pp.1543-1546.

65. Panahi, A., Bao, X.L., Yang, K., O'Conchubhair, O. and Ammann, M.J., 2015. A simple polarization reconfigurable printed monopole antenna. IEEE Transactions on Antennas and Propagation, 63(11), pp.5129-5134.

66. Koohestani, M., Zürcher, J.F., Moreira, A.A. and Skrivervik, A.K., 2014. A novel, low-profile, vertically-polarized UWB antenna for WBAN. IEEE Transactions on Antennas and Propagation, 62(4), pp.1888-1894.

67. Abbasi, N.A. and Langley, R.J., 2011. Multiband-integrated antenna/artificial magnetic conductor. IET microwaves, antennas & propagation, 5(6), pp.711-717.

68. Yuan, T., Díaz-Rubio, A. and Ouslimani, H.H., 2016. New Subwavelength Profile Monopole-Type Antenna. IEEE Transactions on Antennas and Propagation, 64(8), pp.3347-3352.

69. Lin, J., Qian, Z., Cao, W., Shi, S., Wang, Q. and Zhong, W., 2017. A low-profile dual-band dual-mode and dual-polarized antenna based on AMC. IEEE Antennas and Wireless Propagation Letters, 16, pp.2473-2476.

70. Wu, J., Yang, S., Chen, Y., Qu, S. and Nie, Z., 2016. A low profile dual-polarized wideband omnidirectional antenna based on AMC reflector. IEEE Transactions on Antennas and Propagation, 65(1), pp.368-374.

71. Cao, Y.F., Zhang, X.Y. and Mo, T., 2018. Low-profile conical-pattern slot antenna with wideband performance using artificial magnetic conductors. IEEE Transactions on Antennas and Propagation, 66(5), pp.2210-2218.

72. Jackson, D. and Alexopoulos, N., 1985. Gain enhancement methods for printed circuit antennas. IEEE transactions on antennas and propagation, 33(9), pp.976-987.

73. Jackson, D.R., Burghignoli, P., Lovat, G., Capolino, F., Chen, J., Wilton, D.R. and Oliner, A.A., 2011. The fundamental physics of directive beaming at microwave and optical frequencies and the role of leaky waves. Proceedings of the IEEE, 99(10), pp.1780-1805.

74. Kim, J.H., Ahn, C.H. and Bang, J.K., 2016. Antenna gain enhancement using a holey superstrate. IEEE Transactions on Antennas and Propagation, 64(3), pp.1164-1167.

75. Mittra, R., Li, Y., & Yoo, K. (2010). A comparative study of directivity enhancement of microstrip patch antennas with using three different superstrates. Microwave and Optical technology letters, 52(2), 327-331.

76. Li, Y., Mittra, R., Zeng, B., Lu, G., Li, Z., Liu, J., ... & Chang, D. C. (2012). Directivity enhancement of fabry-perot antenna by using a stepped-dielectric slab superstrate. Microwave and Optical Technology Letters, 54(3), 711-715.

77. Zhang, S., Arya, R.K., Whittow, W.G., Cadman, D., Mittra, R. and Vardaxoglou, J.C., 2020. Ultra-wideband flat metamaterial GRIN lenses assisted with additive manufacturing technique. IEEE Transactions on Antennas and Propagation, 69(7), pp.3788-3799.

78. Arya, R.K., Zhang, S., Pandey, S., Kumar, A., Vardaxoglou, Y., Whittow, W., and Mittra, R., 2018. Meta-Atoms and Artificially Engineered Materials for Antenna Applications., Developments in Antenna Analysis and Design, 1, pp. 351-405.

79. Zhang, S., Arya, R.K., Pandey, S., Vardaxoglou, Y., Whittow, W. and Mittra, R., 2016. 3D-printed planar graded index lenses. IET Microwaves, Antennas & Propagation, 10(13), pp.1411-1419.

80. Yu, B., Yang, K. and Yang, G., 2017. A novel 28 GHz beam steering array for 5G mobile device with metallic casing application. IEEE Transactions on Antennas and Propagation, 66(1), pp.462-466.

81. Zhang, S., Syrytsin, I. and Pedersen, G.F., 2018. Compact beam-steerable antenna array with two passive parasitic elements for 5G mobile terminals at 28 GHz. IEEE Transactions on Antennas and Propagation, 66(10), pp.5193-5203.

82. Shah, A.S.A., Abd Rahman, N.H., Ali, M.T., Fauzi, N.F. and Ab Aziz, A.A., 2016, December. Beam scanning of phased array antenna using phase modification method for

satellite application. In 2016 IEEE Asia-Pacific Conference on Applied Electromagnetics (APACE) (pp. 291-295). IEEE.

83. Serhsouh, I., Himdi, M., Lebbar, H. and Vettikalladi, H., 2020. Reconfigurable SIW antenna for fixed frequency beam scanning and 5G applications. IEEE Access, 8, pp.60084-60089.

84. Wu, L., Farrall, A.J. and Young, P.R., 2015. Substrate integrated waveguide switched beam antenna. IEEE Transactions on Antennas and Propagation, 63(5), pp.2301-2305.

85. Arai, H., 2019, November. High gain optical beam scanning antenna and its measurement. In 2019 IEEE Asia-Pacific Conference on Applied Electromagnetics (APACE) (pp. 1-3).

86. McManamon, P.F., Bos, P.J., Escuti, M.J., Heikenfeld, J., Serati, S., Xie, H. and Watson, E.A., 2009. A review of phased array steering for narrow-band electrooptical systems. Proceedings of the IEEE, 97(6), pp.1078-1096.

87. Schmidt, U. and Thust, W., US Philips Corp, 1971. Optical deflection system including an alternating sequence of birefringent prisms and polarizers. U.S. Patent 3,572,895.

88. Karim, M.A., Cook, D. and McManamon, P.F., 1988, October. Digital beam steering system using modules of ferro electric liquid crystal and Wollaston prism. In Tech. Dig. 1988 Annu. Meeting Opt. Soc. Amer. (p. 118).

89. Van Acoleyen, K., Bogaerts, W., Jágerská, J., Le Thomas, N., Houdré, R. and Baets, R., 2009. Off-chip beam steering with a one-dimensional optical phased array on silicon-on-insulator. Optics letters, 34(9), pp.1477-1479.

90. Ji, L.Y., Guo, Y.J., Qin, P.Y., Gong, S.X. and Mittra, R., 2015. A reconfigurable partially reflective surface (PRS) antenna for beam steering. IEEE Transactions on Antennas and Propagation, 63(6), pp.2387-2395.

91. Tanoli, S.A.K., Khan, M.I., Fraz, Q., Yang, X. and Shah, S.A., 2018. A compact beam-scanning leaky-wave antenna with improved performance. IEEE Antennas and Wireless Propagation Letters, 17(5), pp.825-828.

92. Symeonidou, A. and Siakavara, K., 2013. A novel microstrip antenna array with metamaterial-based electronic beam steering at 2.4 GHz. Progress In Electromagnetics Research, 38, pp.27-42.

93. Dias, M.H.C., Freitas, V. and Vuong, T.P., 2015. Low cost electronic beam tilting of microstrip antennas by the use of tunable parasites. Microwave and Optical Technology Letters, 57(11), pp.2710-2713.

94. Luther, J.J., Ebadi, S. and Gong, X., 2012. A microstrip patch electronically steerable parasitic array radiator (ESPAR) antenna with reactance-tuned coupling and maintained resonance. IEEE Transactions on Antennas and Propagation, 60(4), pp.1803-1813.

95. Khairnar, V.V., Kadam, B.V., Ramesha, C.K. and Gudino, L.J., 2018. A reconfigurable parasitic antenna with continuous beam scanning capability in H-plane. AEU-International Journal of Electronics and Communications, 88, pp.78-86.

96. Li, Z., Mopidevi, H., Kaynar, O.Ğ.U.Z. and Cetiner, B.A., 2012. Beam-steering antenna based on parasitic layer. Electronics Letters, 48(2), pp.59-60.

97. Xing, L., Zhu, J., Xu, Q., Yan, D. and Zhao, Y., 2019. A circular beam-steering antenna with parasitic water reflectors. IEEE Antennas and Wireless Propagation Letters, 18(10), pp.2140-2144.

98. Ourir, A., Burokur, S.N. and De Lustrac, A., 2007. Phase-varying metamaterial for compact steerable directive antenna. Electronics letters, 43(9), pp.493-494.

99. Chu H., Guo Y X., 2017. A Filtering Dual-Polarized Antenna Subarray Targeting for Base Stations in Millimeter-Wave 5G Wireless Communications. IEEE Trans. Compon. Packaging Manuf. Technol., 2017, 7 (6), pp. 964-973.

100. Ojaroudiparchin, N., Shen, M., Zhang, S. and Pedersen, G.F., 2016. A switchable 3-D-coverage-phased array antenna package for 5G mobile terminals. IEEE Antennas and Wireless Propagation Letters, 15, pp.1747-1750.

101. Hong, K.D., Huang, G.L., Zhang, X. and Yuan, T., 2019, July. A High-Performance Radome for Millimeter Wave Antenna Applications. In 2019 Cross Strait Quad-Regional Radio Science and Wireless Technology Conference (CSQRWC) (pp. 1-3). IEEE.

102. Hashem, Y.A., Haraz, O.M. and El-Sayed, E.D.M., 2016, June. 6-Element 28/38 GHz dual-band MIMO PIFA for future 5G cellular systems. In 2016 IEEE International Symposium on Antennas and Propagation (APSURSI) (pp. 393-394). IEEE.

103. Morshed, K.M., Esselle, K.P., Heimlich, M., Habibi, D. and Ahmad, I., 2016, May. Wideband slotted planar inverted-F antenna for millimeter-wave 5G mobile devices. In 2016 IEEE Region 10 Symposium (TENSYMP) (pp. 194-197). IEEE.

104. Wang, L., Guo, Y.X. and Sheng, W., 2012, December. A 60-GHz wideband L-probe patch antenna array with gain enhanced structure based on LTCC technology. In 2012 Asia Pacific Microwave Conference Proceedings (pp. 151-153). IEEE.

105. Park, J.S., Ko, J.B., Kwon, H.K., Kang, B.S., Park, B. and Kim, D., 2016. A tilted combined beam antenna for 5G communications using a 28-GHz band. IEEE Antennas and Wireless Propagation Letters, 15, pp.1685-1688.

106. Aliakbari, H., Abdipour, A., Mirzavand, R., Costanzo, A. and Mousavi, P., 2016, April. A single feed dual-band circularly polarized millimeter-wave antenna for 5G communication. In 2016 10th European conference on antennas and propagation (EuCAP) (pp. 1-5). IEEE.

107. Kornprobst, J., Wang, K., Hamberger, G. and Eibert, T.F., 2017. A mm-wave patch antenna with broad bandwidth and a wide angular range. IEEE Transactions on Antennas and Propagation, 65(8), pp.4293-4298.

108. Agrawal, T. and Srivastava, S., 2018. Ku band pattern reconfigurable substrate integrated waveguide leaky wave horn antenna. AEU-International Journal of Electronics and Communications, 87, pp.70-75.

109. Faezi, H., Kashani, F.H. and Tayarani, M., 2018. Reduction of the effects of dielectric coating with the extended ground on a small slot leaky wave waveguide antenna. AEU-International Journal of Electronics and Communications, 94, pp.84-90.

110. Panda, P.K. and Ghosh, D., 2019. Wideband and high gain tuning fork shaped monopole antenna using high impedance surface. AEU-International Journal of Electronics and Communications, 111, p.152920.

111. Feng, G., Shi, X., Chen, L., Yue, H. and Yang, Y., 2017. A metasurfaced surface-wave antenna with performance enhancement. Journal of ElEctromagnEtic WavEs and applications, 31(11-12), pp.1167-1176.

112. Hasan, M.N., Bashir, S. and Chu, S., 2019. Dual band omnidirectional millimeter wave antenna for 5G communications. Journal of Electromagnetic Waves and Applications, 33(12), pp.1581-1590.

113. Katare, K.K., Chandravanshi, S., Biswas, A. and Akhtar, M.J., 2019. Realization of split beam antenna using transmission-type coding metasurface and planar lens. IEEE Transactions on Antennas and Propagation, 67(4), pp.2074-2084.

114. Cai, T., Wang, G.M., Zhang, X.F., Liang, J.G., Zhuang, Y.Q., Liu, D. and Xu, H.X., 2015. Ultra-thin polarization beam splitter using 2-D transmissive phase gradient metasurface. IEEE Transactions on Antennas and Propagation, 63(12), pp.5629-5636.

115. Jiang, H., Si, L.M., Hu, W. and Lv, X., 2019. A symmetrical dual-beam bowtie antenna with gain enhancement using metamaterial for 5G MIMO applications. IEEE Photonics Journal, 11(1), pp.1-9.

116. Khidre, A., Lee, K.F., Elsherbeni, A.Z. and Yang, F., 2013. Wide band dual-beam U-slot microstrip antenna. IEEE transactions on antennas and propagation, 61(3), pp.1415-1418.

117. Park, J., Seong, H., Whang, Y.N. and Hong, W., 2019. Energy-efficient 5G phased arrays incorporating vertically polarized endfire planar folded slot antenna for mmWave mobile terminals. IEEE Transactions on Antennas and Propagation, 68(1), pp.230-241.

118. Guan DF, Zhang Q, You P, Yang ZB, Zhou Y, Yong SW. Scanning rate enhancement of leaky wave antenna with slow-wave substrate integrated waveguide (SIW) structure. IEEE Trans Antennas Propag. Early Access.

119. De Paula, I.L., Lemey, S., Bosman, D., Van den Brande, Q., Caytan, O., Lambrecht, J., Cauwe, M., Torfs, G. and Rogier, H., 2020. Cost-Effective High-Performance Air-Filled SIW Antenna Array for the Global 5G 26 GHz and 28 GHz Bands. IEEE Antennas and Wireless Propagation Letters, 20(2), pp.194-198.

120. Ansari, M., Zhu, H., Shariati, N. and Guo, Y.J., 2019. Compact planar beamforming array with endfire radiating elements for 5G applications. IEEE Transactions on Antennas and Propagation, 67(11), pp.6859-6869.

121. Varum, T., Ramos, A. and Matos, J.N., 2018, August. Planar microstrip series-fed array for 5G applications with beamforming capabilities. In 2018 IEEE MTT-S International Microwave Workshop Series on 5G Hardware and System Technologies (IMWS-5G) (pp. 1-3). IEEE.

122. Wu, X., Eleftheriades, G.V. and van Deventer-Perkins, T.E., 2001. Design and characterization of single-and multiple-beam mm-wave circularly polarized substrate lens antennas for wireless communications. IEEE Transactions on Microwave Theory and Techniques, 49(3), pp.431-441.

123. Hall, P.S. and Vetterlein, S.J., 1990, October. Review of radio frequency beamforming techniques for scanned and multiple beam antennas. In IEE Proceedings H (Microwaves, Antennas and Propagation) (Vol. 137, No. 5, pp. 293-303). IET Digital Library.

124. Cheng, Y. M., Chen, P., Hong, W., Djerafi, T., Wu, K., 2011. Substrate-Integrated - Waveguide Beamforming Networks and Multi beam Antenna Arrays for Low-Cost Satellite and Mobile Systems. IEEE Antennas Propag., 53 (6), pp. 18-30.

125. Kumar, K., Dwari, S., 2017. Substrate Integrated Waveguide Cavity-Backed Self-Triplexing Slot Antenna. IEEE ANTENN WIREL PR., 16, pp. 3249 – 3252.

126. Peters, F.D., Tatu, S.O. and Denidni, T.A., 2012, July. Design of beamforming slot antenna arrays using substrate integrated waveguide. In Proceedings of the 2012 IEEE International Symposium on Antennas and Propagation (pp. 1-2). IEEE.

127. Alonso, L., Ver Hoeye, S., Fernández, M., Vázquez, C., Camblor, R., Hotopan, G., Hadarig, A. and Las-Heras, F., 2015, May. Millimetre wave textile integrated waveguide beamforming antenna for radar applications. In Global Symposium on Millimeter-Waves (GSMM) (pp. 1-3). IEEE.

128. Cheng, Y.J. and Xuan, Z.J., 2017, March. Two-dimensional beam scanning antenna array with 90-degree SIW twist. In 2017 International Workshop on Antenna Technology: Small Antennas, Innovative Structures, and Applications (iWAT) (pp. 264-266). IEEE.

129. Cheng, Y.J., 2012. Substrate integrated waveguide frequency-agile slot antenna and its multibeam application. Progress In Electromagnetics Research, 130, pp.153-168.

130. Cheng, Y.J., Hong, W. and Wu, K., 2009. Millimeter-wave multibeam antenna based on eight-port hybrid. IEEE Microwave and Wireless components letters, 19(4), pp.212-214.

131. Cheng, Y.J., Hong, W., Wu, K. and Fan, Y., 2010. Millimeter-wave substrate integrated waveguide long slot leaky-wave antennas and two-dimensional multibeam applications. IEEE Transactions on Antennas and Propagation, 59(1), pp.40-47.

132. Guntupalli, A.B., Djerafi, T. and Wu, K., 2013. Two-dimensional scanning antenna array driven by integrated waveguide phase shifter. IEEE Transactions on Antennas and Propagation, 62(3), pp.1117-1124.

133. Yang, W., Yang, Y., Che, W., Fan, C. and Xue, Q., 2017. 94-GHz compact 2-D multibeam LTCC antenna based on multifolded SIW beam-forming network. IEEE Transactions on Antennas and Propagation, 65(8), pp.4328-4333.

134. Ghanem, F., Delisle, G.Y., Denidni, T.A. and Ghanem, K., 2005, June. Directive frequency switched beam antenna based on EBG structures. In 11th International Symposium on Antenna Technology and Applied Electromagnetics [ANTEM 2005] (pp. 1-4). IEEE.

135. Ashraf, N., Haraz, O., Ashraf, M.A. and Alshebeili, S., 2015, May. 28/38-GHz dual-band millimeter wave SIW array antenna with EBG structures for 5G applications. In 2015 international conference on information and communication technology research (ICTRC) (pp. 5-8). IEEE.

136. Karthikeya, G.S., Abegaonkar, M.P. and Koul, S.K., 2017, November. Low cost high gain triple band mmWave Sierpinski antenna loaded with uniplanar EBG for 5G applications. In 2017 IEEE International Conference on Antenna Innovations & Modern Technologies for Ground, Aircraft and Satellite Applications (iAIM) (pp. 1-5). IEEE.

137. Yang, F. and Rahmat-Samii, Y., 2003. Reflection phase characterizations of the EBG ground plane for low profile wire antenna applications. IEEE Transactions on antennas and propagation, 51(10), pp.2691-2703.

138. Lu, C., Shen, J., Cao, W., Shao, W. and Meng, F., 2014, July. A broadband circularly polarized antenna array for beamforming applications in X-band. In 2014 IEEE Antennas and Propagation Society International Symposium (APSURSI) (pp. 1740-1741). IEEE.

139. Huang, K.C. and Wang, Z., 2006. Millimeter-wave circular polarized beam-steering antenna array for gigabit wireless communications. IEEE Transactions on Antennas and Propagation, 54(2), pp.743-746.

140. Chaimool, S., Rakluea, C. and Akkaraekthalin, P., 2011, December. Low-profile unidirectional microstrip-fed slot antenna using metasurface. In 2011 International Symposium on Intelligent Signal Processing and Communications Systems (ISPACS) (pp. 1-5). IEEE.

141. Zhu, H.L., Cheung, S.W., Chung, K.L. and Yuk, T.I., 2013. Linear-to-circular polarization conversion using metasurface. IEEE transactions on antennas and propagation, 61(9), pp.4615-4623.

142. Kordiboroujeni, Z. and Bornemann, J., 2013. Designing the width of substrate integrated waveguide structures. IEEE Microwave and wireless components letters, 23(10), pp.518-520.

143. Alphones, A., Mujumdar, M. and Jin, C., 2013, November. Substrate integrated waveguide and its applications to leaky wave antennas. In 2013 Asia-Pacific Microwave Conference Proceedings (APMC) (pp. 470-472). IEEE.

144. Kumar, N. and Khanna, R., 2020. A compact multi-band multi-input multi-output antenna for 4G/5G and IoT devices using theory of characteristic modes. International Journal of RF and Microwave Computer-Aided Engineering, 30(1), p.e22012.

145. Kim, S.H. and Chung, J.Y., 2020. Analysis of the envelope correlation coefficient of MIMO antennas connected with suspended lines. Journal of Electromagnetic Engineering and Science, 20(2), pp.83-90.